

Acoustical Modeling of the Transient Response of Rooms Using a Beam-Tracing Model

by

Behrooz Yousefzadeh

B.Sc., University of Tehran, Iran, 2008

A THESIS SUBMITTED IN THE PARTIAL FULFILMENT OF
THE REQUIREMENTS FOR THE DEGREE OF

MASTER OF APPLIED SCIENCE

in

The Faculty of Graduate Studies

(Mechanical Engineering)

THE UNIVERSITY OF BRITISH COLUMBIA

(Vancouver)

October 2010

© Behrooz Yousefzadeh, 2010

Abstract

Two room-acoustical prediction models were previously developed in the UBC Acoustics and Noise Research Group and used for studying the steady-state responses of various room configurations. The first is a wave-based beam-tracing model for empty rooms with specularly-reflecting, extended-reaction surfaces. Room surfaces were modeled as multiple layers of elastic solid, fluid and poroelastic materials, and their acoustical properties were calculated using a transfer-matrix approach. The second model, PRAY, is a wave-based ray-tracing model which can account for fittings, diffuse surface reflection and sound diffraction. This thesis presents further development of the existing beam-tracing model, incorporating features from PRAY such as diffuse reflection. The computational efficiency of the existing model has been improved and energy-based prediction has been implemented. Both wave- and energy-based modeling have been validated against theory for the case of sound propagation above a rigid plane. The new model can predict the pressure impulse response between the source and receiver, which is required for obtaining the temporal response of rooms to other sound sources, as well as for deriving room-acoustical parameters that correlate with subjective perception of sound. The new model is used to compare the effects of different surface-reaction models on the transient response and derived room-acoustical parameters. In addition to investigating the significance of modeling room surfaces as of extended or local reaction, effects of phase changes due to surface reflections have been studied by considering real and complex reflection coefficients. Moreover, wave-based energy impulse responses and room-acoustical parameters have been compared with those obtained from energy-based modeling. Modeling of diffuse surface reflections has been implemented in the model and validated against existing experimental results. The model has been further extended to include sound diffraction around wedges based on an exact formulation. This broadens the application of the model to situations with more realistic features, such as sound propagation in fitted rooms or in long enclosures with bends, and evaluation of screen barriers in open-plan offices. The implemented diffraction model has been validated through comparison with existing results in the literature, and by comparing prediction results with experiments on a finite-length barrier over a flat surface.

Table of Contents

Abstract	ii
Table of Contents	iii
List of Tables	vi
List of Figures	vii
Acknowledgements	x
Chapter 1	
Introduction.....	1
Chapter 2	
Background and Literature Review	6
2.1 Theoretical Background.....	6
2.2 Prediction Models in Room Acoustics	11
2.2.1 Modal Theory	12
2.2.2 Diffuse-Field Theory	13
2.2.3 Geometrical Room Acoustics	15
2.2.4 Diffusion Models	23
2.2.5 Numerical Analysis	24
2.3 Modeling of Surface Diffusion within Geometrical Models	25
2.4 Modeling of Sound Diffraction	27
2.5 Existing Ray- and Beam-Tracing Models	30
2.5.1 The Ray-Tracing Model	30
2.5.2 The Beam-Tracing Model.....	31
2.6 Summary.....	31
Chapter 3	
Development of the New Model.....	32
3.1 The Tracing Algorithm.....	33
3.2 The Steady-State Response: Energy and Phase Models.....	35
3.3 Attenuation of Sound by Air.....	36
3.4 Modeling Specular Reflections.....	37
3.4.1 Derivation of Basic Relations.....	38
3.4.2 Transfer-Matrix Modeling of Multilayer Walls	41

3.5 Modeling Diffuse Reflections.....	43
3.6 The Transient Response.....	44
3.6.1 Impulse Responses and Echograms.....	45
3.6.2 The relation between the pressure impulse response and the transfer function	47
3.6.3 Octave-Band Impulse Responses	49
3.7 Room-Acoustical Parameters	51
3.8 Edge Diffraction	57
3.8.1 Svensson’s Model.....	57
3.8.2 The Uniform Theory of Diffraction.....	62
3.9 Summary.....	64
Chapter 4	
Validation of the New Model	65
4.1 Computational Efficiency.....	66
4.1.1 Coding Improvements	66
4.1.2 Pre-Calculation of Source Beams.....	67
4.1.3 Pre-Calculation of the Acoustical Properties of Multilayer Surfaces.....	68
4.2 Sound Propagation over a Flat Surface	69
4.2.1 Specular Reflection.....	69
4.2.2 Diffuse Reflection.....	71
4.3 Comparison with Measurements in a Reverberant Room	71
4.3.1 Reverberation Time	72
4.3.2 Steady-State Sound-Pressure Level.....	74
4.5 Diffraction.....	77
4.5.1 Validation of the Code.....	77
4.5.2 Comparison with the Uniform Theory of Diffraction	78
4.5.3 Implementation in the Beam-Tracing Model	82
4.6 Summary.....	84
Chapter 5	
Application of the New Model	85
5.1 Test Configurations	87
5.2 Review of Previous Investigations	89
5.3 General Properties of the Boundary Conditions.....	91

5.4 Energy Impulse Responses and Decay Curves.....	97
5.5 Prediction Results	98
5.5.1 Sound Strength	104
5.5.2 Reverberation Time	112
5.5.3 Speech Intelligibility.....	116
5.6 Summary.....	118
Chapter 6	
Conclusions	121
6.1 Accomplishments	121
6.2 Summary of Results.....	123
6.3 Future Work and Improvements.....	124
References.....	126

List of Tables

Table 4.1. Summary of measurement and prediction results for the reverberant room.....	73
Table 5.1. Rooms, surface configurations and source and receiver positions involved in the prediction.	88
Table 5.2. Octave-band diffuse-field absorption coefficients of the test surfaces.	92
Table 5.3. Incident angles corresponding to first-order reflection paths for the three rooms....	109
Table 5.4. Relation between STI values and speech-intelligibility ratings.....	116

List of Figures

Figure 3.1. Reflection of plane waves from a uniform wall.	39
Figure 3.2. Profile view of a multilayer wall.	42
Figure 3.3. An echogram.	47
Figure 3.4. Relations between the time- and frequency-domain windows.	48
Figure 3.5. Octave-band Gabor and rectangular pulses at 250 Hz in: a) time domain, and b) frequency domain. Solid line: Gabor pulse; dashed line: rectangular pulse.	50
Figure 3.6. Wedge geometry and coordinate system. P_S and P_R are the planes containing the edge and the source and receiver, respectively.	58
Figure 3.7. The three zones formed around a diffracting edge when the diffracted sound is not present.	59
Figure 3.8. Unfolded, two-dimensional view of the wedge, along with the source, receiver and the apex point.	61
Figure 3.9. Side-view of the wedge with notations used in UTD.	62
Figure 4.1. Time require for calculating the source beams as a function of the icosahedron frequency. Solid line: the existing <i>icosa</i> function; dash-dot line: the modified function.	68
Figure 4.2. Sound pressure level over a flat, rigid surface at 1000 Hz. The beam-tracing model gave exactly the same results as the theory. Solid line: wave-based modeling; dash-dot line: energy-based modeling.	70
Figure 4.3. Comparison of pure-tone measured and predicted steady-state sound-pressure levels in a reverberant room at 86 Hz. Solid line: measurement; black dashed lines: wave-based prediction for R1; black dash-dot lines: energy-based prediction for R1; grey dashed lines: wave-based prediction for Z1; grey dash-dot lines: energy-based prediction for Z1.	75
Figure 4.4. Comparison of pure-tone measured and predicted steady-state sound-pressure levels in a reverberant room at 172 Hz. Solid line: measurement; black dashed lines: wave-based prediction for R1; black dash-dot lines: energy-based prediction for R1; grey dashed lines: wave-based prediction for Z1; grey dash-dot lines: energy-based prediction for Z1.	75
Figure 4.5. Comparison of pure-tone measured and predicted steady-state sound-pressure levels in a reverberant room at 258 Hz. Solid line: measurement; black dashed lines: wave-based prediction for R1; black dash-dot lines: energy-based prediction for R1; grey dashed lines: wave-based prediction for Z1; grey dash-dot lines: energy-based prediction for Z1.	76
Figure 4.6. Comparison of pure-tone measured and predicted steady-state sound-pressure levels in a reverberant room at 430 Hz. Solid line: measurement; black dashed lines: wave-based prediction for R1; black dash-dot lines: energy-based prediction for R1; grey dashed lines: wave-based prediction for Z1; grey dash-dot lines: energy-based prediction for Z1.	76
Figure 4.7. The configuration used for predicting the results in Figure 4.8.	78
Figure 4.8. Magnitude of the diffraction coefficient calculated using Svensson's model for the configuration in Figure 4.7. (a) Receiver R_1 . Solid line: edge length = 16 m; dotted line: edge length = 4 m; dash-dot line: edge length = 2 m; dashed line: edge length = 1m. (b)	

Receiver R_2 , edge length = 1 m. Note that the magnitude of diffraction coefficients is presented as $20\log(H_{diff}(\omega))$	79
Figure 4.9. Reference solution for the configuration corresponding to Receiver R1	79
Figure 4.10. Magnitude of the predicted diffraction coefficients at receiver R_1 in Figure 4.8. Grey line: UTD; black lines: Svensson's model with different wedge lengths (solid line: 16 m, dashed line: 2 m, dotted line: 1 m).	80
Figure 4.11. Source and receiver configuration for barrier insertion-loss measurements.	81
Figure 4.12. Third-octave-band measured and predicted sound-pressure levels and insertion losses of the barrier configuration at 1000 Hz. (a) Sound-pressure levels. Grey lines: without the barrier (solid line: measurement, dashed line: prediction); black lines: with the barrier (solid lines: measurement, dashed line: prediction using Svensson's model, dotted line: prediction using UTD. (b) Insertion loss. Circles: measurement; squares: Svensson's model; diamonds: UTD.	81
Figure 4.13. Layout of the configuration used by Lau and Tang [78] for insertion-loss measurements. Beam-tracing predictions were compared with the experimental results along the middle row of receivers.	83
Figure 4.14. Insertion loss of the barrier in the configuration shown in Figure 4.14 in the 1000-Hz octave band. Dashed line: measurement; solid lines: beam-tracing predictions (thick line: using UTD; thin line: using Svensson's model).....	84
Figure 5.1. Diffuse-field absorption coefficient of the double-drywall panel (black curves) and the double-steel panel (grey curves). Solid lines: assuming extended reaction; dotted lines: assuming local reaction.....	93
Figure 5.2. Diffuse-field absorption coefficient of the test surfaces with porous layers, assuming extended reaction (black curves) and local reaction (grey curves). Solid lines: FA; dashed lines: FR; dotted lines: CAF.....	93
Figure 5.3. Octave-band absorption coefficients of test surfaces at 125 Hz. Black curves: extended reaction; grey curves: local reaction. Solid lines: DGP; dotted line: DDW; dashed lines: SGP; dash-dot line: DSP.....	95
Figure 5.4. Octave-band absorption coefficients of test surfaces at 125 Hz. Black curves: extended reaction; grey curves: local reaction. Dotted line: FR; dashed lines: CAF; dash-dot line: FA.....	95
Figure 5.5. Octave-band predicted energy impulse response of the R1 configuration: a) wave-based, 500 Hz; b) wave-based 1000 Hz; c) wave-based, 2000 Hz; d) wave-based, 4000 Hz; e) energy-based.	99
Figure 5.6. Octave-band predicted energy impulse response of the R2 configuration: a) wave-based, 500 Hz; b) wave-based 1000 Hz; c) wave-based, 2000 Hz; d) wave-based, 4000 Hz; e) energy-based.	100
Figure 5.7. Octave-band predicted energy impulse response of the R3 configuration: a) wave-based, 500 Hz; b) wave-based 1000 Hz; c) wave-based, 2000 Hz; d) wave-based, 4000 Hz; e) energy-based.	101

Figure 5.8. Octave-band sound-decay curves for configuration R1: a) 500 Hz, b) 1000 Hz, c) 2000 Hz, d) 4000 Hz. Solid lines: wave-based; dashed lines: energy-based. Curves for (b), (c) and (d) were moved -7.5, -15 and -22.5 dB, respectively, so that details can be seen.....	102
Figure 5.9. Octave-band sound-decay curves for configuration R2: a) 500 Hz, b) 1000 Hz, c) 2000 Hz, d) 4000 Hz. Solid lines: wave-based; dashed lines: energy-based. Curves for (b), (c) and (d) were moved -7.5, -15 and -22.5 dB, respectively, so that details can be seen.....	102
Figure 5.10. Octave-band sound-decay curves for configuration R3: a) 500 Hz, b) 1000 Hz, c) 2000 Hz, d) 4000 Hz. Solid lines: wave-based; dashed lines: energy-based. Curves for (b), (c) and (d) were moved -7.5, -15 and -22.5 dB, respectively, so that details can be seen.....	103
Figure 5.11. Octave-band steady-state sound-pressure levels for configuration G1-ext, using 3920 beams and 50 reflections. Diamonds: Wareing's original results; dash-dot line: total levels, 10-Hz resolution; dotted line: total levels, 0.5-Hz resolution; dashed line: average levels, 10-Hz resolution, solid line: average levels, 0.5-Hz resolution.	105
Figure 5.12. Octave-band sound strength G for six configurations: G1, D1, G2, D2, G3 and SW3. Grey lines: energy-based predictions; solid line: EBR-ext, dashed line: EBR-loc. Black lines: wave-based predictions; solid line: WBC-ext, dashed line: WBC-loc, dash-dot line: WBR-ext, dotted line: WBR-loc.....	106
Figure 5.13. Octave-band sound strength G for six configurations: C1, SAC2, C2, SAC2, FG3 and SC3. Grey lines: energy-based predictions; solid line: EBR-ext, dashed line: EBR-loc. Black lines: wave-based predictions; solid line: WBC-ext, dashed line: WBC-loc, dash-dot line: WBR-ext, dotted line: WBR-loc.	107
Figure 5.14. Predicted reflection coefficient of the FR test surface, fibreglass on rigid backing, at the 76° angle of incidence. Black solid line: magnitude; black dashed line: phase (radians); grey solid line: real part; grey dashed line: imaginary part.....	110
Figure 5.15. Predicted real part and absolute value of the reflection coefficient of the FA test surface, as a function of incident angle at: a) 45 Hz, b) 90 Hz, c) 125 Hz and d) 180 Hz. Black curves: real parts; grey curves: absolute values. Solid lines: extended-reaction; dashed lines: local-reaction.	111
Figure 5.16. Predicted octave-band reverberation times T_{20} for six configurations: G1, D1, G2, D2, G3 and SW3. Grey lines: energy-based predictions; solid line: EBR-ext, dashed line: EBR-loc. Black lines: wave-based predictions; solid line: WBC-ext, dashed line: WBC-loc, dash-dot line: WBR-ext, dotted line: WBR-loc.....	113
Figure 5.17. Predicted octave-band reverberation times T_{20} for six configurations: C1, SAC2, C2, SAC2, FG3 and SC3. Grey lines: energy-based predictions; solid line: EBR-ext, dashed line: EBR-loc. Black lines: wave-based predictions; solid line: WBC-ext, dashed line: WBC-loc, dash-dot line: WBR-ext, dotted line: WBR-loc.....	114
Figure 5.18. Predicted RASTI values for all test configurations. Black bars: extended-reaction; Grey bars: local-reaction. WBC: wave-based prediction with complex reflection coefficients; WBR: wave-based prediction with real reflection coefficients; EBR: energy-based prediction with real reflection coefficients.....	117

Acknowledgements

First and foremost, I would like to express my gratitude to my supervisor, Professor Murray Hodgson, Director of the Acoustics and Noise Research Group at UBC. I am very grateful to him for the time and effort that he committed to my education, as well as for his continuous support and encouragement.

A toast to my colleagues at the Acoustics Lab, Gavin Steininger and Chris Bibby, who made the bridge for me between the real world and the window-less acoustical island of the Library Processing Center. Cheers!

Finally, I would like to thank my parents for their continuous support throughout my journey to the other side of the globe.

Chapter 1

Introduction

Most of us spend a significant portion of our lives in closed rooms. Although we may not be consciously aware of it, the acoustical conditions in rooms significantly influence our activities. In classrooms, for example, student learning efficiency is reduced as a result of inadequate speech intelligibility, in particular in the case of young children. In industrial workshops, workers are often exposed to excessive noise due to poor acoustical conditions in their work environments. As a consequence, they experience various health problems, such as hearing loss, stress and fatigue, as well as reduced productivity.

Being able to accurately predict the sound field in a room is invaluable to practicing acousticians, because it enables them to assess various acoustical-design strategies prior to construction, and evaluate the effectiveness and cost of noise-control strategies for optimal

acoustical conditions inside existing rooms. In other words, it enables the acoustician to “hear” how a room sounds, without having to build the actual space.

For such a design tool to make accurate, realistic predictions of the sound fields, it needs to effectively take into account various phenomena that influence the acoustical environment in a room. These features include the interference of sound waves with each other, the reaction of different types of surfaces to incident sound (either local or extended reaction), and the scattering of sound waves caused by diffuse reflection from surfaces and by diffraction around obstacles. Furthermore, it needs to be capable of predicting both the steady-state and transient responses of the room; while these are equivalent, they represent different aspects of the sound field. Impulse responses are specifically important for studying subjective aspects of the room sound field, since the room-acoustical parameters which are found to correlate with subjective perception of sound fields are defined based on the impulse responses of rooms.

Based on the way interference effects are treated, prediction models can be either energy-based or wave-based. In energy-based modeling, sound waves are assumed to be incoherent, so that they do not interfere with each other, and the energies of the waves add; wave-based models, on the other hand, take interference effects into account by adding the complex pressures of sound waves.

The interaction of sound waves with the boundaries of a room has a significant effect on the room sound field. When a sound wave hits a surface, only a portion of its energy is reflected back into the room; the rest is either absorbed by the surface or transmitted through it. The magnitude and phase of the reflected wave is determined from the acoustical characteristics of the surface, as well as the frequency of the incident wave and the angle between the wave direction and the surface (the angle of incidence). The acoustical properties of a wall surface can be completely described by its “surface impedance”, which is defined, in the frequency domain,

as the ratio between the sound pressure at the surface and the particle velocity normal to the surface.

In general, the impedance of a surface is a function of both frequency and the angle of incidence. In this case, the surface is said to be of extended reaction. Two commonly-used simplifying assumptions are to ignore the angular dependence of the surface impedance or reflection coefficient of the surface. When the impedance of the surface is independent of the direction of the incident sound, the surface is said to be of local reaction. This is equivalent to assuming that the particle velocity generated by the incident wave at any point on the surface is related to the local pressure only, and is therefore independent of the form of the incident sound field. From a rigorous point of view, all surfaces exhibit extended reaction to the incident sound; in some cases, however, they can be assumed to react locally. Local reaction is encountered whenever the wall itself or the space behind it is unable to propagate waves or vibrations in a direction parallel to its surface. This is generally a reasonable assumption for walls made of simple absorptive materials, because they dissipate the energy of acoustic waves effectively. On the other hand, local reaction is not a realistic assumption for walls having significant elastic properties.

Reflection of sound waves from surfaces is most often assumed to be specular; in other words, the angle of reflection is assumed to be equal to the incident angle (Snell's law). Real surfaces, however, often scatter sound energy in all directions. This redirection of all or a portion of sound energy from the specular direction into non-specular directions is called diffuse reflection. Diffuse reflections can be caused by surface irregularities or changes in wall impedance, and result in a more uniform distribution of sound energy throughout the room. The reflection at a surface is considered to be totally diffuse if the reflected sound intensity is equal

in all directions (Lambert's law). Diffuse reflection is an important property of room boundaries and should be taken into account for realistic prediction of the sound field.

In many rooms, the direct path between a sound source and a receiver can be obstructed. An important mode of sound propagation, in this case, is through diffraction around the free boundary or boundaries of the occluding surface; this surface can belong to an obstacle or be a part of the room boundaries (a column, for example). Diffraction not only significantly changes the sound field in shadow zones behind the obstacle, but also makes audible changes to the sound field in non-shadow zones. It is therefore important for an acoustical model to be capable of accounting for sound diffraction.

Two room-acoustical prediction models have previously been developed by the UBC Acoustics and Noise Research Group. The first was a wave-based beam-tracing model for empty rooms with specularly-reflecting, extended-reaction surfaces. The second was a wave-based ray-tracing model which could account for partial diffuse reflection and first-order diffraction around free edges. Both models predicted steady-state sound-pressure fields in rooms, but not their transient responses (*i.e.* the impulse response of the rooms). Moreover, the diffraction algorithm that was used in the ray-tracing model was based on a high-frequency, approximate formulation of sound diffraction over wedges of infinite length. It was therefore of interest to replace it by an exact formulation.

The general objective of the research reported here was to develop a new beam-tracing model which included as many desirable features of the two existing models as possible. Specifically, the new model was required to predict the transient response of rooms, so that derived room-acoustical parameters could be calculated. One main objective of the current work was to study the effects of different surface-reaction models on the steady-state characteristics and temporal variations of sound-pressure fields in various room configurations. This had

already been done in part using the existing beam-tracing model: the effects of modeling surfaces as of local or of extended reaction on steady-state sound-pressure levels were investigated in twelve room configurations. The aim here was to extend this study from steady-state pressure levels to transient conditions and other room-acoustical parameters. Moreover, the significance of modeling interference effects on the sound fields were to be investigated. This involved two stages: in the first stage, all phase effects were to be ignored (energy-based modeling); in the second stage, only phase changes on surface reflection were to be ignored. Consequently, energy-based modeling of both the steady-state and transient responses of rooms was implemented in the new beam-tracing model.

Modeling of diffuse reflection and edge diffraction within the new beam-tracing was another objective of the current research. The corresponding algorithms were to be imported from the existing ray-tracing model. The diffraction modeling, however, was to be improved and based on a more reliable theory.

In summary, the objective of this thesis is the development of this new beam-tracing model. The theoretical background on acoustics, and a review of the literature on prediction models in room acoustics, are presented in Chapter 2, along with an overview of the two existing models. In Chapter 3, the structure and theory of the new beam-tracing model is discussed in detail. Modifications made to the existing model, and its new features, are then validated in Chapter 4. Results obtained from application of the model are presented and discussed in Chapter 5. Finally, a summary of the results is presented in Chapter 6, along with conclusions and suggestions for future work.

Chapter 2

Background and Literature Review

We begin this chapter by discussing the fundamental characteristics of sound waves, their propagation in air and their interaction with the boundaries. We then provide an overview of prediction models in room acoustics, describing the fundamental concepts in each modeling technique and the differences between them. Next is presented the two existing models based on which the new model is to be developed.

2.1 Theoretical Background

The relation between spatial and temporal variations of acoustic-pressure fluctuations in a fluid is described by the wave equation:

$$\nabla^2 p - \frac{1}{c^2} \frac{\partial^2 p}{\partial t^2} = 0 \quad (2.1)$$

Here c is the speed of propagation and p is the acoustic or sound pressure, which is the difference between the instantaneous and static pressures in the fluid. In room acoustics, the medium of propagation is air, treated as an ideal gas. It is implicitly assumed in Eq. (2.1) that the medium is homogeneous, at rest and unbounded.

Propagation of acoustic-pressure fluctuations is most often assumed to be adiabatic [108, p.28]. As shown by Morris [98], the propagation speed of acoustic pressure waves as infinitesimal pressure steps can be obtained as a compatibility condition on the system of equations derived from the thermal equation of state and the balances of mass, momentum and total energy. Using Gibbs relation and linearized equations, it then follows that this propagation is isentropic.

In the particular case that all field variables oscillate at a constant angular frequency, ω , the wave equation is reduced to the Helmholtz equation:

$$\nabla^2 p + k^2 p = 0 \quad (2.2)$$

Here k is the wave number, defined as follows:

$$k = \frac{\omega}{c} \quad (2.3)$$

These types of waves are called single-frequency or time-harmonic waves. For other types of time dependence, one can still reduce the wave equation to the Helmholtz equation by means of a Fourier transformation in time. The Helmholtz equation is sometimes called the time-independent or frequency-domain form of the wave equation, on the basis that solutions of the wave and Helmholtz equations can be regarded as Fourier-transform pairs. In room acoustics, analyses are frequently performed in the frequency domain (corresponding to the Helmholtz equation) because boundary conditions are more frequently defined in the frequency domain.

There are various forms of solutions to the wave (or Helmholtz) equation, depending on the physical nature of the sound sources and acoustic environments [31]. Two forms of solutions, however, are of particular interest in room acoustics: plane waves and spherical waves. Plane waves are the simplest types of sound waves in which the acoustical variables depend on one (independent) spatial coordinate only and each acoustical quantity is uniform over plane surfaces normal to this coordinate. In spherical waves, on the other hand, surfaces of constant sound pressure are concentric spheres. In addition, sound intensity decays inversely with the square of the radial distance from the source – this is known as the spherical spreading law [108, p. 42].

For plane waves, the general solution to the wave equation can be written in terms of a Cartesian coordinate, s , along the direction of sound propagation, as follows [108]:

$$p(s, t) = f(t - s/c) + g(t + s/c) \quad (2.4)$$

This is the well-known D’Alembert solution of the wave equation, where f and g are arbitrary functions representing, respectively, plane waves traveling in the positive and negative s -directions with a velocity c . We will return to this solution in the next chapter when studying the reflection of plane waves.

For spherically-symmetric waves, the solution of the wave equation can be written as follows [108]:

$$p(r, t) = \frac{1}{r} f(t - r/c) + \frac{1}{r} g(t + r/c) \quad (2.5)$$

Here f and g are two arbitrary functions representing waves traveling outward from the coordinate origin and converging to the origin, respectively. r denotes the radial distance from the origin, where the source of sound is located – a hypothetical “point” at the center of the spherical wave fronts. Mathematically, point sources are described by Dirac delta functions and represent a discontinuity in the solution at the source position. In practice, however, sources that are small compared to the measurement distance are called point sources, not because they are

physically small but because, at the measurement distance, their size does not influence the behaviour of the radiated sound [85, p.65]. For further details on plane and spherical waves see, for example, [108, Ch. 1] or [74, Ch. 1].

In addition to the free propagation of sound waves as described by the wave or Helmholtz equation, the interaction of sound waves with the boundaries of the medium should be taken into account. Boundaries are interfaces where one medium encounters another one, resulting in the generation of reflected and transmitted waves. There are two boundary conditions that must be satisfied for all times at all points on the boundary [67, p. 125]: continuity of pressure and continuity of normal particle velocity. The first condition ensures that there is no net force on the plane separating the media, and the second condition ensures that the media remain in contact. Acoustic pressure and particle velocity are related through Euler's equation of motion,

$$\rho \frac{\partial \vec{u}(\vec{r}, t)}{\partial t} + \vec{\nabla} p(\vec{r}, t) = 0 \quad (2.6)$$

Here \vec{r} is a position vector and $\vec{u}(\vec{r}, t)$ denotes the acoustic particle velocity, which is a vector field and a function of space and time. Denoting the outward direction normal to a wall by the normal vector, \hat{n} , and projecting Eq. (2.6) in this direction,

$$\rho \frac{\partial(\hat{n} \cdot \vec{u})}{\partial t} + \hat{n} \cdot \vec{\nabla} p = 0 \quad (2.7)$$

In the context of room acoustics, the boundaries are often the walls of a room (six flat surfaces in the simplest case). A very common boundary condition is the surface impedance of the wall, which is defined, in the frequency domain, as follows:

$$Z = \left(\frac{p}{\hat{n} \cdot \vec{u}} \right)_{surface} \quad (2.8)$$

Acoustical impedance is regarded as one of the most important acoustical properties of materials and surfaces, and is a measure of the “resistance” to motion at a given point; in other words, the acoustical impedance of a wall describes how much a wall impedes sound propagation through it, in amplitude and phase. Impedance is usually normalized to the characteristic impedance of the medium of propagation, ρc , where ρ is the density of the fluid. The resulting specific impedance is denoted by ζ :

$$\zeta = \frac{Z}{\rho c} \quad (2.9)$$

Impedance is generally complex, meaning that the normal velocity is not necessarily in phase with the incident pressure wave. The real and imaginary parts of the impedance are called resistance and reactance, respectively. Admittance, Y , is the reciprocal of impedance and carries the same information about the surface as impedance. Admittance is used when equations are more conveniently formulated in terms of Y than Z .

Using the two boundary conditions described above, Euler’s equation and the definition of impedance, a generic impedance boundary condition can be written as follows, in the frequency domain:

$$\hat{n} \cdot \bar{\nabla} p + i \frac{\rho \omega}{Z} p = 0 \quad (2.10)$$

Subject to this impedance boundary condition, solution of the Helmholtz equation gives the steady-state pressure field inside the room. We will discuss this further in the next section.

The steady-state sound field is usually characterized, specifically in engineering applications, on a logarithmic scale. The reason is that, in the frequency range that human hearing is most sensitive, the intensities of the sound that can just be heard and that is painful to hear differ by about 13 orders of magnitude [74, p. 22]; as a result, it would be impractical to use a linear scale. A second reason for using a logarithmic scale is that we judge the relative

loudness of different sounds by the ratio of their intensities [67, p.115]. Logarithmic scales are used for this purpose to define quantities known as sound levels.

There are different levels used in acoustics [6]. In this research we only use sound pressure level, *SPL*, which is defined as follows:

$$SPL=10\log\left(\frac{p_{rms}}{p_0}\right)^2 \quad (2.11)$$

Here p_{rms} denotes the root-mean-square value of the sound pressure and p_0 denotes the reference pressure, which corresponds roughly to the average hearing threshold of airborne sound at 1 kHz. *SPL* is expressed in decibels, and it is often adequate in most noise-control applications to quote it to the nearest decibel value [6].

2.2 Prediction Models in Room Acoustics

Prediction models in room acoustics attempt to find the temporal and spatial distributions of sound pressure or energy (pressure squared) inside an enclosed space according to the source and boundary conditions of the room. Predictions are either energy-based or wave-based. Energy-based models assume sound waves to be incoherent, meaning that they do not interfere with each other; in wave-based modeling, on the other hand, interference effects are taken into account.

Room-acoustical prediction models can be placed in the following categories: modal theory, diffuse-field theory, geometrical room acoustics, and diffusion models. The modal theory is wave-based, while diffuse-field theory and diffusion models are inherently energy-based. Geometrical models were traditionally defined as energy-based models, but can be modified to make wave-based predictions as well. In this section, we will introduce each of these categories, explaining their underlying assumptions and range of applicability. This is followed by a brief introduction to numerical methods in acoustics. These are general approaches for solving

differential and integral equations, and are addressed here due to their wide application to room acoustics.

The models mentioned above are all theoretical. It should be mentioned that empirical models also exist in room acoustics. Empirical models are developed from experimental data and usually focus on a particular category of rooms – e.g. industrial workrooms and classrooms. See [49] for further information on empirical models in room acoustics.

2.2.1 Modal Theory

The modal theory, also known as the wave-theoretical approach, tackles the Helmholtz equation directly in order to solve it for the pressure field. The Helmholtz equation gives non-zero solutions satisfying the impedance boundary conditions only for discrete values of the wave number, called wave-number eigenvalues, or eigenvalues in general. Corresponding to each wave-number eigenvalue is a frequency eigenvalue or eigenfrequency, as calculated by Eq. (2.3). Each eigenvalue is associated with a solution of the Helmholtz equation, known as an eigenfunction or a natural mode. These represent three-dimensional standing waves known as the normal modes of the room. The general solution of the equation is the superposition (summation) of all these modes. This is why this approach is called the modal theory of room acoustics.

In mathematical terms, the Helmholtz equation in Eq. (2.2), subject to impedance boundary conditions as in Eq. (2.10), forms a non-self-adjoint Sturm-Liouville boundary-value problem, which gives rise to an eigenvalue problem. A mathematically-rigorous discussion of this can be found in [88].

The modal theory of room acoustics is most easily explained for a rectangular room with rigid walls, as elaborated by Kuttruff [74, Ch. 3.2]. When the walls of the room are not rigid or soft, but nearly rigid or soft, approximations can be made to form an analytical solution; for

example, see [100, Ch. 10.3] for an analytical derivation of the sound field in a lightly-damped enclosure, or [27] for a first-order perturbation analysis applying to rooms with nearly-rigid or nearly-soft walls.

For rectangular rooms with arbitrary wall impedances, eigenfrequencies can be obtained only by means of numerical approximations. The first solution set forth was probably that of Morse who, in 1939, assumed the same impedance on each pair of parallel walls [94]. Morse also used his results in studying the transmission of sound inside rectangular pipes lined with absorptive materials [95]. Later, Mechel revisited Morse's approach and improved it [93]. Recently, numerical methods have been proposed [9,99], which can be reliably used for any choice of uniform impedance on each wall.

Apart from calculating the eigenfrequencies, it is ideally desired to solve the governing equations analytically. This would be the most reliable and appropriate theory for room acoustics from a physical point of view [74, p.68]. Nevertheless, the complexities associated with analytical (exact and approximate) methods increase very rapidly as the boundary conditions become more realistic, and it becomes necessary to seek other forms of solutions by means of employing numerical approximations or developing alternative approaches such as the diffuse-field theory or geometrical room acoustics.

2.2.2 Diffuse-Field Theory

The diffuse-field theory is the best known theoretical model for predicting room sound fields and is widely used by practitioners due to its simplicity [49]. It can be used to predict the sound decay (and therefore the reverberation time) of a room with a diffuse sound field, as well as the room's steady-state sound-pressure level. To be considered diffuse, the sound field in a room should satisfy the following two conditions [48]:

- 1) The sound field should be the same at every position in the room;

- 2) At any point in the room, sound waves should arrive from all directions with equal intensity and random phase relations.

This idealization of a room's sound field was first proposed by Sabine about a century ago. In its classical forms, Sabine and Eyring formulations, the diffuse-field theory can be derived using conservation of the acoustic energy in a room, as described by Pierce [108, Ch. 6.1]. The governing integral equations of a diffuse sound field have been derived by Kuttruff as the radiosity integral; see [74, Ch. 4.5]. It assumes the walls of the enclosure to reflect the incident sound waves in a totally diffuse manner, in which the directional distribution of the reflected sound energy does not depend on the direction of the incident wave. The radiosity integral equation can be solved numerically for arbitrary polyhedral rooms using an algorithm which is called acoustical radiosity [101]. Because acoustical radiosity is usually categorized as a geometrical-acoustics model, we will discuss it in section 2.2.3.1.

The validity of the second assumption of a diffuse field has been put into question for both diffuse fields [87] and non-diffuse reverberant fields [58], mostly in order to improve theoretical predictions to match results from measurements. Most recently, Jeong [58] investigated energy-density distributions incident on an absorber sample for various room shapes and source positions. He then used this information to make more realistic predictions of the absorption coefficients of samples when measured in reverberation chambers [59].

The assumption of a diffuse sound field is generally very restrictive in practice, and the theory has limited applicability to real rooms. For instance, the sound field is not diffuse in a space where one dimension is much bigger than the other two; as a matter of fact, diffuse-field formulae are even more inaccurate when the boundaries of a long enclosure are assumed to be diffusely-reflecting [65]. In its classical forms – the Sabine and Eyring formulations – diffuse-field theory can only accurately predict both sound decay and steady-state pressure level in the

case of an empty room with quasi-cubic dimensions, specularly-reflecting walls and uniform surface absorption [48]. The theory accounts for only some of the relevant features of a room [49]: room geometry and source directivity are modeled only approximately, while the distribution of surface absorption and the presence of furnishings or barriers are not modeled.

2.2.3 Geometrical Room Acoustics

Geometrical acoustics is a branch of acoustical theory in which the concept of a sound wave is replaced by the concept of a sound ray. The name comes from “geometrical optics”, where the techniques in geometrical acoustics were initially taken from [109]. By a sound ray we mean “a small portion of a spherical wave with vanishingly small aperture which originates from a certain [source] point” and differs from light rays only in the propagation speed [74]. Sometimes the term “sound particle” is used in the same context, as small energy packets or carriers traveling along sound rays with a constant speed. These particles are purely hypothetical and have no physical instance in the real world. They represent the analogy between the movement of a wavefront along a ray with that of a point mass in the absence of gravity. This analogy can be rationalized from the fact that in a homogeneous, isotropic medium at rest, which is normally the case in room acoustics, wavefronts are normal to rays and travel at constant speed along them [109]. A more tangible description of sound particles is made by Kuttruff [74, p.128] as short sound pulses propagating along sound ray paths, all having the same broadband power spectrum. Detailed descriptions of sound rays and ray acoustics can be found in [108, Ch. 8].

Methods of geometrical acoustics are traditionally energy-based models, neglecting the wave properties of sound. Geometrical acoustics has been developed as a high-frequency, broadband approximation of the wave-theoretical approach, in which a very large number of modes need to be calculated in order to cover a wide frequency range. At lower frequencies, where the

wavelength of sound waves is comparable with the characteristic dimensions of the room, only a few standing waves are excited and the modal series expansion of the pressure field converges fairly rapidly. At higher frequencies, however, the modal theory of room acoustics “no longer has either conceptual simplicity or provides ease of computation” [97, p.576], the resonances merge and knowledge of individual normal modes becomes “pointless” [74].

Classically, there are two geometrical models in room acoustics: the method of image sources and ray tracing. A third category of geometrical models consists of beam-tracing models, which are more recent and can be regarded as alternative forms of the ray-tracing algorithm. Acoustical radiosity is also considered a geometrical-acoustics model and is the fourth category of geometrical models considered here. In this section, each of these four categories is introduced in some detail. There also exist hybrid models which take advantage of features from more than one category of these models. These will be discussed within the four main categories. After this introduction, two important issues associated with the geometrical models will be discussed: introduction of phase changes and surface-reaction modeling.

2.2.3.1 Four Categories of Geometrical Models

The method of image sources, or the image method in short, is based on the assumption that reflections from surfaces of the room are purely specular and that they can be replaced by the direct sound from a virtual source of the same power output (assuming omni-directionality), and still satisfy the surface boundary conditions. This virtual source is located in place of the mirror image of the real source with respect to the plane of reflection. The use of an image source is equivalent to the assumption of a rigid-wall (zero normal velocity) boundary condition [1], and does not strictly apply to finite-impedance boundaries. However, this approximation is almost always tolerated in geometrical acoustics. For non-rigid surfaces, the amplitude of the output of the virtual source is multiplied by the relevant reflection coefficient of the surface at

that point. This implies a plane-wave assumption, which is valid if the plane of reflection is infinite in extent and its reflection coefficient does not vary over the surface [77]. Although these assumptions do not generally apply to real surfaces, we will see in section 2.2.3.3 that they are not too restrictive and have generally been tolerated.

The image method of Allen and Berkeley [1] is one of the best known of its kind in room acoustics. The model takes phase changes due to distance traveled into account, but assumes real-valued, frequency- and angle-independent pressure-reflection coefficients to avoid additional computational cost. A significance of the model of Allen and Berkeley is that it is considered [74] to be the first model to be used for purely computer-based auralization. This model was extended to arbitrary polyhedrons by Borish [11] and later improved computationally by Lee and Lee [79]. The image method is conceptually simple and mathematically easy to program. It is a deterministic model and gives the correct impulse response of the room within the assumptions of geometrical acoustics, because it can find all the transmission paths between a source and a receiver. However, as the order of the images increases, most of the image sources become invalid and it takes an enormous computational effort to identify and eliminate them [91]. Alternative algorithms have been proposed to overcome this problem, such as [130] and [81]. For a detailed description of the image-source model see [132].

According to Kuttruff [74], the first acoustical simulation of concert halls by a computer model was carried out by Krokstad *et al.* [70] using a stochastic ray-tracing technique. It has since been improved and used by numerous authors and in different contexts. Ray-tracing techniques can now be used to make wave-based prediction of sound fields in rooms of arbitrary shape with arbitrary surface-property distributions and source directivity, variable fitting density and diffracting edges [49].

In ray-tracing, numerous sound rays or particles are emitted from a source in straight lines and traced as they propagate to a receiver, taking into account their interactions with different surfaces in the room. For an omni-directional sound source, the rays should be emitted randomly around the source with a uniform angular distribution. This random distribution of source rays is what makes ray-tracing a stochastic process. Ray-tracing can also be implemented in a deterministic manner; however, this would increase the chances of spatial aliasing [38].

According to Lehnert [80], there are two types of errors inherent in the ray-tracing algorithm. The first error is due to the limited number of traceable rays. The problem in this case is not using enough rays, which results in insufficient coverage of the sound field and detected reflections. The second error is due to detection problems: because rays are dimensionless, a point receiver will not be able to detect them; a receiver with finite volume is needed instead. However, this could result in receiver directionality, as well as multiple and invalid detections. The probability of a sound particle being detected is a function of the area of the cross-section of the detector facing the direction of incidence; as a result, the shape of the detector volume determines the directionality of the receiver. For example, a planar disc shows a figure-of-eight receiving characteristic; only a sphere has omni-directional reception. In order to optimize this type of error, various receiver-radius sizes have been proposed by different researchers; e.g. Jiang and Qiu [62] and Xiangyang [138].

Randomly-distributed scattering obstacles in a room can be modeled using an algorithm proposed by Ondet and Barbry for “fitted” workshops [103]. In this model, the fitted region is divided into a number of zones, each having a fitting density and reflection coefficient. Fittings are omni-directionally scattering points with the free paths between them distributed according to a Poisson distribution with some average value. The “fitting density” is the inverse of this value. Upon arrival, each ray is reflected according to this coefficient and scattered into a

random direction. The model assumes cubic receivers. It has been shown by Hodgson [46] that the model proposed by Ondet and Barbry can make accurate predictions of the sound field in rooms with non-uniform fittings.

Beam-tracing is an alternative method to ray-tracing, in which dimensionless rays are replaced by rays having some volume, the beams. Beam-tracing was first introduced in computer graphics [2, 44] in order to overcome the inherent uncertainties in ray-tracing due to the statistical nature of the rays. In its original form, beams had conical shapes. The problem with conical beams is that they cannot model a source without overlapping; this is overcome by using pyramid-shaped beams [37].

In acoustics, conical [86], pyramidal [33] and triangular [82] beam-tracing techniques have been used. Beam-tracing models are deterministic and allow for a point receiver. Beam-tracing produces the same results as the image method for specular reflections, but optimizes the visibility calculations so that only valid image sources are considered [75]. However, the beam-front becomes larger as beams propagate in the room and eventually intersects more than one surface or becomes larger than a surface. This results in overlaps and missing reflections and can be overcome by an adaptive tracing algorithm [28], in which the shape of the reflected beams is redefined by the shape of the reflecting surface, in order to prevent overlaps and holes in the sound field. The problem with the adaptive tracing algorithm is that it is difficult to implement, because it relies on “sophisticated techniques to map out sections of illumination” [28]. According to Laine *et al.* [75], beam-tracing is the fastest geometrical model in acoustics.

The acoustical radiosity method is an inherently energy-based geometrical model in room acoustics, which can be regarded as a numerical implementation of the integral equation of the diffuse sound in an enclosure [101]; it therefore assumes diffuse reflection. One of the earliest realizations of the acoustical radiosity is by Lewers [82], where it was combined with a beam-

tracing model. By 2003, algorithms for acoustical radiosity were developed for arbitrary polyhedral enclosures by Nosal *et al.* [101]. Experimental evaluation of acoustical radiosity [51] suggests that it is most accurate in rooms with surfaces that reflect sound somewhat diffusely.

2.2.3.2 Introduction of Phase Changes

Traditional energy-based geometrical models work well with relatively proportionate geometry, large room volumes, and medium to high frequency, in which the distribution of the reflection directions is well mixed [77]. Nevertheless, when the wavelength of sound becomes comparable to the dimensions of the room, the wave behaviour of sound, such as interference, becomes too important to be neglected. Models that can account for wave effects of the sound field are called wave-based models or phase models.

Interference effects can be modeled effectively if sound energy is replaced by complex pressure amplitudes, which include phase information from the propagation path [77, 119]. Phase information can more readily be applied to an image method than to ray- or beam-tracing methods [137]; one of the earliest models to include phase information was the image method of Allen and Berkeley [1]. Wave-based image methods have since been used by other authors – for example, by Guo and Hodgson [39] to study the active control of noise from a point source and by Xiangyang *et al.* [137] to model the behaviour of multiple sources, both in an empty, rectangular room. The first implementation of phase into ray-tracing and beam-tracing models is often [61, 119, 134] attributed to De Geest and Patzold [26] and De Geest and Garcea [25], respectively. In both cases, the transfer function of the room was calculated using both a boundary-element method and the proposed wave-based model, showing good agreement between the results.

Using a wave-based beam-tracing model, Jeong *et al.* [60, 61] have compared energy impulse responses obtained using both energy- and wave-based approaches with results from

measurements. It was observed that the results obtained from the phase model were notably closer to measurements than results from the energy model, specifically in the early part of the impulse response and at lower frequencies.

Phase information is crucial for construction of pressure impulse responses [77]. As will be discussed in detail in chapter 3.6, pressure impulse responses can be calculated from the transfer function of a room, provided that phase information is included in the transfer function. This is a common method for calculating the pressure impulse response using geometrical models [1, 61, 77, 119]. It should also be mentioned that it has been proposed by Kuttruff [72, 73] that the phase spectrum of a room transfer function is “non-critical” and that it is sufficient to choose any phase function which is convenient for the processing. He gives the example of assuming the transfer function to be minimum-phase, for which the phase information can be obtained using a Hilbert transform [90]. On the other hand, it can be seen in the work by Jeong and Ih [60] that the transfer function of a room is not minimum-phase.

Another significance of modeling phase is that phase shifts due to surface reflections can be modeled. This is done by replacing the real-valued reflection coefficients of surfaces with complex reflection coefficients. The effects of modeling phase changes upon reflection will be discussed in the next section.

2.2.3.3 Surface-Reaction Modeling

The traditional boundary condition used in (energy-based) geometrical models is a frequency- and angularly-invariant absorption coefficient for room surfaces. An improvement to this boundary condition is to use absorption coefficients for different octave bands. This information is traditionally obtained from measurements in a reverberation chamber, as explained in [22, Ch. 3.4]. Real-valued reflection coefficients are often obtained from the absorption coefficient, neglecting sound transmission through the boundaries.

One important characteristic of the reflection coefficients of real surfaces is its dependence on the angle of incidence. An empirical model for modeling the reflection coefficient of square surfaces is proposed by Rindel [110] based on the impedance and absorption coefficient of the samples measured in a diffuse-field condition, and as a function of frequency, angle of incidence and the surface area of the samples. The model assumes locally-reacting surfaces and neglects the imaginary part of the reflection coefficient. This model was used by Jeong *et al.* [61] in a wave-based beam-tracing model. Results of predictions using both energy-based and wave-based modeling suggest that the best match with measurements is obtained using the angle-dependent reflection coefficient; however, a reasonably good accuracy could still be obtained using an angle-independent reflection coefficient based on a measured absorption coefficient. The authors suggest that use of a complex reflection coefficient will improve the precision of the results.

Suh and Nelson [119] investigated the effect of phase changes on reflection by replacing the measured surface impedance by a real-valued impedance which has the same absorption coefficient. By comparing the transfer function of the room for both cases, they conclude that accounting for reflection phase changes has a significant effect on the accuracy of the model, “at least for fairly absorptive surfaces”.

The validity of the plane-wave reflection coefficient has been called into question by several authors. The study by Suh and Nelson [119] concludes that the accuracy of approximating spherical-wave reflection coefficients with the plane-wave reflection coefficient decreases when the absorption coefficient of the surface or the angle of incidence increases, as well as when the distance between the source and receiver decreases. Moreover, the study by Lam [77] has shown through various examples that using a spherical-wave reflection coefficient gives results which are very close to those obtained by a boundary-element analysis. The results

further suggest that the plane-wave reflection model was found to give noticeable errors for highly absorptive surfaces (absorption coefficient greater than 0.5) and for higher orders of reflection.

In order to study the effect of modeling the surfaces of a room as of extended- or local-reaction, Wareing and Hodgson [134] used a beam-tracing model. Implemented in their beam-tracing model is a transfer-matrix algorithm for calculating the acoustical properties of room surfaces, which are modeled as multiple layers of elastic solid, fluid and poroelastic materials. Several multilayer surfaces in three room configurations were studied and predicted steady-state levels were compared. It was concluded that the difference between modeling a room surface as of extended- or local-reaction is significant when the surface consists of multilayers of solid or porous material and includes a layer of fluid with a large thickness relative to other layers. A plane-wave reflection coefficient was used in this study.

2.2.4 Diffusion Models

An alternative approach to describing the sound field in enclosures is by modeling sound propagation as a diffusion process. This is based on the analogy of sound energy density with a density of particles traveling (diffusing) at a constant speed along straight lines [127]: the sound particles in an enclosure represent its acoustical energy content and can be imagined as the molecules of a gas [74, Ch. 5.7]. The motion of this sound gas is then modeled as a diffusion process.

This diffusion approach to sound propagation was originally developed as a generalization of the Sabine diffuse-field theory in 1969 [102]. It was improved in 1997 by Picaut *et al.* [105] and then applied to various problems in room acoustics, such as long rooms [106], fitted rooms (*i.e.* rooms containing obstacles that scatter sound) [128], coupled rooms [8],

and rooms with mixed diffuse and specular reflections [34]. Since 2007, the diffusion model has also been studied by Jing and Xiang [63], and applied to coupled [136] and long [64] enclosures.

Diffusion models are intrinsically energy approaches, and they are more general than diffuse-field theory due to the fact that they allow for internal energy flows and, therefore, local variations of the energy density. According to Kuttruff [74], the complete solution of the diffusion equations is not easier than that of the wave equation because in both cases a set of eigenvalues and eigenfunctions needs to be calculated. Nevertheless, the required number of eigenfunctions is often much fewer in diffusion equations, because they neglect phase relations and only deal with sound energy.

2.2.5 Numerical Analysis

In a very general sense [32], in numerical analysis we assume various forms of distributions for the field quantities that are present in the governing equations, together with sets of unknown coefficients that specify the contribution of these distributions to the total field. By entering the expressions for these contributions into the governing equation, various computational techniques are used to produce estimates of the unknown coefficients. There are three main categories of numerical analyses used in acoustics: Finite Difference, Finite Element and Boundary Element Analysis.

Finite-Difference Analysis (FDA) is the most intuitive and most straightforward way to approach differential equations numerically. In FDA [32], the fluid region is divided by a line grid, and field values are assigned to the grid intersection points. Partial derivatives are then represented by finite-difference approximations, relating the parameters at any given grid point to its surrounding grid points. An initial set of field values is assumed and then iterated systematically to a stable solution. The main practical problem with FDA in application to sound fields in volumes of arbitrary geometry is that it does not readily accommodate boundaries that

do not conform to the grid-line pattern. In room acoustics, FDA is often used for time-domain analyses; for example, see [12].

Finite-Element Analysis (FEA) and Boundary-Element Analysis (BEA) are the two most widely used numerical methods in acoustics. FEA and BEA [104] were originally developed, respectively, for analyzing the dynamics of complex structures and for predicting noise radiation from vibrating structures in an infinite acoustic medium. They are both applied to integral forms of the wave equation and represent a continuous system (infinite degrees of freedom) by a discrete system (finite degrees of freedom). The accuracy of the solution, therefore, depends on the number of degrees of freedom used. The higher the frequency of interest, the more degrees of freedom are required. Consequently, these methods become inefficient at higher frequencies. High-frequency problems in acoustics are dealt with using other methods, such as geometrical techniques in room acoustics and statistical energy analysis in vibroacoustics.

For interior problems, finite-element methods (FEM) are more economical than boundary-element methods (BEM) in most practical configurations [42]. One can therefore argue that FEM is used more often than BEM in room acoustics. Nevertheless, both methods are commonly used in room-acoustical analyses – see [29] and [123] as cases in point. References [32] and [104] provide very useful introductions to FEA and BEA of interior and exterior problems in acoustics, including examples from room acoustics.

2.3 Modeling of Surface Diffusion within Geometrical Models

Diffuse reflection is recognized as an extremely important phenomenon in room acoustics, having a strong impact on the perceived quality of the room sound field [23]. Torres *et al.* [124] performed listening tests to investigate the audibility of frequency-dependent changes in diffuse-reflection modeling, using computed auralizations of a concert hall. They found that not only is the inclusion of diffuse reflections in the model audible, but also that diffuse

reflections should be modeled in a frequency-dependent manner. We will return to the discussion of diffuse-reflection modeling in section 3.5.

It is generally believed that partial diffusion occurs inevitably when sound is reflected from a real wall, and that including (preferably frequency-dependent) diffuse reflection is one of the necessary conditions for good prediction accuracy in geometrical room models [129, 47, 21, 76]. The most obvious deficiency resulting from calculations based only on specular reflection is an overestimation of reverberation time [30, 22]. This is especially true for enclosures where absorption is concentrated on one surface or when the shape is highly disproportionate [76, 47].

While there are various methods for incorporating diffuse surface reflections in a geometrical room model (see [23] and [22, Ch. 12.3]), it is not known which modeling technique, if any, is intrinsically more accurate [22, p. 408]. The scattered energy in geometrical models is most commonly assumed [21] to be distributed according to Lambert's cosine law, which assumes [74, Ch. 4.5] that the diffused sound intensity is equal in all directions. Such a distribution is achieved if the diffused energy is proportional to the cosine of the angle of reflection. While Lambert's law applies to totally-diffuse reflection, reflections are often only partially diffuse in room acoustics. Nevertheless, it has been pointed out by Kuttruff [74, p.122] that, in reverberant enclosures, "the assumption of totally diffuse reflections comes often closer to the properties of real walls than that of specular reflection, particularly if we are concerned not only with one but instead with many successive reflections of a ray from different walls or portions of walls". This rationalizes, to some extent, the use of Lambert's law in geometrical models; in addition, Lambert's law can be used as a "point reflectivity function", a very appealing property for computer models [23].

2.4 Modeling of Sound Diffraction

Diffraction is a mode of sound propagation, particularly important in situations where the direct path between a sound source and a receiver is occluded. In rooms, this can happen due to presence of obstacles (equipment in an industrial building, for example) or geometrical features of the room such as columns and corners. While obstructing the direct source-receiver path very significantly changes the sound field in the shadow zone, it makes audible changes to the sound field in non-shadow zones as well [125]. As a result, it is important for an acoustical model to correctly model sound diffraction.

The first mathematical formulation of wave diffraction is attributed [83, 10] to Sommerfeld in 1896, who considered the two-dimensional problem of a plane wave incident on an infinite half-plane with hard surfaces. A generalization of this formulation to diffraction of time-harmonic spherical waves is, among others, due to McDonald in 1915 [89]; this is often referred to as a reference solution [83, 108]. Pierce [107] extended this approach to sound diffraction around wedges; in addition, he formulated an approximate second-order solution for diffraction over a truncated wedge, taking into account first-order diffraction from the two edges, as well as second-order diffraction over the top of the truncated wedge. The equivalent formulation in the time domain is due to Biot and Tolstoy in 1957 [10], who provided an exact, closed-form solution for the impulse response of a spherical sound wave diffracted by an infinitely-long, straight wedge with hard surfaces. This is often referred to as the Biot-Tolstoy model. Medwin [92] modified the source term in the Biot-Tolstoy model, and extended it to model first-order diffraction from wedges of finite length; the Biot-Tolstoy-Medwin (BTM) model.

Both time- and frequency-domain approaches provide the exact solution for diffraction from an infinite rigid wedge; these are presented as a counter integral in the complex plane,

“with an integrand of moderate complexity involving elementary transcendental functions” [40], which cannot be evaluated simply. Svensson *et al.* [122] reformulated the BTM model as a line integral along the diffracting edge, which has the benefit of allowing for simulations of finite and infinite edges with the appropriate choice of integral limits. In the new formulation, the edge of the wedge is interpreted as a collection of infinitesimal secondary sound sources; the diffracted sound is therefore calculated by dividing the edge into infinitesimal parts and integrating the radiation of all these parts over the edge. This formulation was later transformed to the frequency domain by Svensson *et al.* [121], and was shown to be equivalent to Pierce’s formulation in the case of an infinite wedge. Furthermore, careful measurements of the diffraction of sound from an edge of a thin chipboard panel were performed in both time and frequency domains by Lokki *et al.* [84]. They compared measurement results with theoretical simulations based on the model developed by Svensson *et al.* [122], showing that the theoretical model can make accurate predictions of the diffracted sound field.

In the case of frequency-domain formulations, if both the source and receiver are located at distances from the edge that are large compared to the sound wavelength, the solutions can be expressed using an asymptotic approximation by Fresnel integrals [40]. An example of such an approximate model is the Geometrical Theory of Diffraction (GTD), which was introduced by Keller in 1962 [66]. GTD extended the ray theory of light (geometrical optics) to account for diffracted rays, and is therefore limited to high frequencies. The Uniform Theory of Diffraction (UTD) was developed by Kouyoumjian and Pathak in 1974 [69] as an improvement of GTD, by overcoming the problem with singularities of GTD at shadow and reflection boundaries. Both GTD and UTD are restricted to infinite wedges. For a given source and receiver position, a complex-valued diffraction coefficient is calculated, which can be multiplied by the pressure-amplitude of the incident sound ray to obtain the pressure-amplitude of the diffracted sound ray.

In geometrical room acoustics, modeling sound diffraction is traditionally ignored, partly because accounting for diffraction is very time consuming [131, 116]. This, however, is a very serious shortcoming; diffraction is a very common phenomenon in real rooms since the wavelengths of sound waves in the audible spectrum are of the same order of magnitude as the characteristic lengths of many objects in rooms [74].

A number of attempts have been made to make diffraction modeling possible in room-acoustical models. UTD provides a straightforward algorithm for implementing diffraction into geometrical-acoustics models based on the fact that it is a geometrical model itself; moreover, it accounts for both the magnitude and phase change of sound rays on diffraction. In room-acoustical applications, UTD has been used, as a case in point, by Funkhouser *et al.* [35], who developed a beam-tracing model to compute early propagation paths from a static source to a moving receiver for real-time auralization in large architectural environments. Chan [19] implemented UTD in a wave-based ray-tracing model in order to investigate sound-pressure fields in rooms containing parallelepiped obstacles at low frequencies, for which the wavelength is comparable to the obstacle dimensions. Only first-order diffraction was considered by Chan. He compared ray-tracing predictions with experimental results, and with predictions by a finite-element method. Although his predictions were performed at low frequencies, first-order modeling of diffraction using UTD was successful in predicting shadow zones. The accuracy of predictions could be further improved by using a diffraction model which is valid for the low frequencies considered, such as the model by Svensson *et al.* [122].

An energetic approach to sound diffraction was proposed by Stephenson and Svensson [117], based on an analogy to Heisenberg's uncertainty relation. This model has recently been used by Stephenson [116] in a two-dimensional, energy-based ray-tracing model, and very good

agreement has been obtained with results obtained from the model by Svensson *et al.* [122] in the case of an infinite half-plane.

2.5 Existing Ray- and Beam-Tracing Models

The present work is an integration of two existing geometrical room-acoustical models: a ray-tracing model consolidated by Hodgson *et al.* [50] and a beam-tracing model developed by Wareing and Hodgson [134]. In this section, each of these models will be explained.

2.5.1 The Ray-Tracing Model

The ray-tracing model developed by Hodgson *et al.* [50] – hereafter called PRAY – is based on the ray-tracing algorithm of Ondet and Barbry [103]. This model predicts sound-pressure level (based on sound energy) at any number of cubic receiver cells in a horizontal plane in a room. The source is omnidirectional and air absorption can be taken into account. The room can be almost any polyhedron with walls of constant energy reflection coefficients. Moreover, scattering obstacles can be modeled by user-defined fitting densities and reflection coefficients. Fittings can be divided into a number of zones and are assumed to scatter sound omnidirectionally.

This model was improved by Hodgson [47] to include diffuse surface reflections according to Lambert's law. The new model was called DRAY. It was further improved [45] to calculate the energy echogram and room-acoustical parameters at a single receiver cell, while still accounting for diffuse surface reflection. This model is called ERAY; it has recently been used to investigate optimal reverberation times in classrooms for speech intelligibility, based on the assumption of a diffuse sound field [53]. In another line of research, Chan [19] and Cousins [20] developed PRAY from DRAY: they translated the program from FORTRAN to MATLAB, implemented phase changes due to distance traveled and surface reflections, made predictions

based on complex sound pressure instead of sound energy, and included the prediction of sound intensity. Moreover, Chan implemented the prediction of sound diffraction from wedges into PRAY, based on the uniform theory of diffraction [69]. This wave-based model was later used in a rectangular-duct configuration, and shown to be capable of predicting the modal characteristics of the duct's sound field [139].

2.5.2 The Beam-Tracing Model

The beam-tracing model developed by Wareing [133] is based on the triangular beam-tracing model of Lewers [82], but extended to include phase. It can be used to predict steady-state sound fields in empty rooms with walls that reflect sound specularly. Most importantly, the model involved a transfer-matrix algorithm integrated into the beam-tracing algorithm. The transfer-matrix algorithm is used to calculate the frequency- and angularly-varying acoustical properties of room surfaces. Room surfaces are modeled as multilayer surfaces of fluid, solid or poro-elastic materials, and Biot theory is used in the transfer-matrix formulation of the poro-elastic layers as described in [17]. The model was subsequently used to compare the effects of extended- and local-reaction modeling of room surfaces on steady-state pressure levels in three different room configurations [52]. The results of this research will be reviewed in section 5.2 of this thesis.

2.6 Summary

With the review of the theoretical background and the literature related to this research presented in this chapter, we are now ready to discuss features of the new model in detail. Development of the new beam-tracing model is presented in the following chapter.

Chapter 3

Development of the New Model

As was discussed in the previous chapter, it was decided that the new model would be a beam-tracing model. It was therefore developed based on the existing beam-tracing model by Wareing [133]. The general structure of the new model is the same as the existing one, but modifications have been made to accommodate new algorithms inside the code and improve the existing ones. Features (diffuse reflections and edge diffraction) from the existing ray-tracing model have been included in the new beam-tracing model, and features (calculation of the transient response of the room and the room-acoustical parameters) new to both the existing beam- and ray-tracing models have been added. Modifications have also been made to the existing model to improve its computational efficiency; these will be addressed in section 4.1. This chapter lays out the structure and theory of the new beam-tracing model. Presentation and

discussion of the results obtained from the implementation of the new model will be postponed until Chapters 4 and 5.

This chapter begins with a brief description of the sound source modeling and the tracing algorithm – complete details are available in Wareing’s thesis [133]. Calculation of the steady-state response of the room is then described, and the differences between the energy and phase models are explained. Modeling of specular and diffuse reflections are described next, followed by the method of calculating the transient response of the room, explaining the relationship between the transient and steady-state responses of the room. The room-acoustical parameters considered in this research are then defined and their relevance to the subjective perception of the sound field is addressed briefly. Finally, the two formulations of sound diffraction used in this research are briefly explained.

3.1 The Tracing Algorithm

The beam-tracing algorithm models a spherical wave that is generated by a single-frequency point source and propagates inside an enclosure. The source is omnidirectional and has a constant power at all frequencies. A spherical wave was approximated by a point source surrounded by a modified icosahedron with subdivided triangular faces. The modified icosahedron is made by dividing each edge of the 20 faces of an icosahedron into f_i equal lengths. This results in a polygon with $20 f_i^2$ faces or beam fronts. Each beam initially consists of three bounding rays (the vertices of the sub-icosahedron face) and a center ray originating at the source and normal to the beam front. Associated with each beam are also three bounding planes. Beams are propagated through the room by tracing their center ray for a number of reflection equal to a predefined reflection order. A beam’s vertex is the real source in the room if it contains the direct source-receiver path; otherwise, for beams containing a source-receiver path involving reflections, the vertices are the image sources that were last calculated.

In a free field, a single-frequency spherical wave is expressed as follows:

$$p(r, t) = \frac{P_0}{r} e^{i(\omega t - kr)} \quad (3.1)$$

Here p_0 is the amplitude of the acoustic pressure wave. It can be expressed [74] either in terms of the source sound power, W :

$$p_0 = \sqrt{\frac{\rho c W}{4\pi}} \quad (3.2)$$

or in terms of the source volume velocity, Q :

$$p_0 = \frac{\rho \omega^2 Q^2}{8\pi c} \quad (3.3)$$

Pressure amplitude decays with distance from the source. The initial phase angle of the beams is set to zero and changes linearly with the distance L from the source as $-kL$, where k is the wave number. As a beam arrives at the walls, its amplitude and phase change according to the reflection characteristics of the wall: the associated complex pressure-reflection coefficient is multiplied by the incident beam's complex pressure to find the pressure of the reflected beam front. When a beam reflects from a surface, the incident trajectory is replaced by one originating from an image source, and the image source becomes the new start point for the reflected beam. Modifications made to this algorithm to account for diffuse reflections and edge diffraction will be discussed in sections 3.5 and 4.5.3, respectively.

Whenever a beam reaches a receiver, its contribution to the acoustic pressure at that receiver point is calculated as follows:

$$p_{beam} = \frac{P_0}{L} R_{eff} e^{-ikL} ; \quad R_{eff} = \prod_{i=1}^{r_0} R_i \quad (3.4)$$

Here, R_{eff} is the effective reflection coefficient for that specific beam, which accounts for the reflection coefficient of all reflecting surfaces, R_i , encountered by the beam up to the reflection

order, r_o , during its path from the source to the receiver. Also note that, in comparison with Eq. (3.1), the pressure amplitude in Eq. (3.4) does not have the time-dependent factor, $\exp(i\omega t)$. The reason is that, in the analysis of time-harmonic waves, the time dependence is the same for all parameters and is usually dropped.

3.2 The Steady-State Response: Energy and Phase Models

Both the existing ray-tracing and beam-tracing models make steady-state predictions only; the ray-tracing model makes predictions of both sound pressure and energy (*i.e.* pressure squared), while the beam-tracing model makes predictions of sound pressure only. In this section, we discuss calculations of both sound pressure and energy within the new beam-tracing algorithm.

For each beam traveling in the room, Eq. (3.4) expresses the complex pressure at a receiver point between reflections r_o and $r_o + 1$. Using these values, the total steady-state acoustic pressure at a receiver point is calculated by summing the pressures of all beams detected at that receiver point. The corresponding sound-pressure level at each frequency is obtained by taking the absolute value of this complex pressure, squaring it and converting it to decibels as in Eq. (2.11). Moreover, the total pressure at each frequency can be used to create the transfer function of the room. The transfer function is defined in the frequency domain, and its value at each frequency is equal to the total (complex) pressure at that frequency, calculated as described above. The transfer function of a room is also called its frequency response.

In energy models, sound energy is traced instead of sound pressure. At large distances from the source (compared to the acoustic wavelength), the energy density of a spherical source is proportional to the square of its pressure amplitude – see Eq. (1.28) in [74]. Whenever a beam is detected at a receiver point, its sound energy is calculated by taking the absolute value of its complex pressure amplitude and squaring it. The total energy-based sound-pressure level at the

receiver is then calculated by summing the energies of all beams detected at the receiver point and converting the sum to decibels. Interestingly, if the absolute values of the complex pressures are not squared, their sum diverges; *i.e.* increases monotonically. This is, quite probably, analogous to the fact that the series, $\sum_{n=1}^{\infty} 1/n^p$ converges for $p > 1$ and diverges for $p \leq 1$; see [118, p.716], for example.

If the transfer function of the room is built using the total energy at each frequency (instead of the total complex pressure amplitude), the resulting function is called the “energy transfer function” instead, to distinguish it from the transfer function. Note that it would be more correct to rename the transfer function to “pressure transfer function”; this, however, has not been done, because it is not found in the literature. It is also important to remember that, as explained in the previous paragraph, the energy transfer function is not equal to the squared absolute value of the transfer function. We will return to transfer functions in section 3.6.

When, in an energy model, we take the absolute value of the complex pressure amplitude, phase information is lost. As a consequence, interference effects are ignored: when different sound waves are superimposed at a receiver point, their mutual phase relations are not taken into account. As sound waves travel in a medium, their phase angles change linearly with the distance traveled. Moreover, sound waves that have been reflected or diffracted are not generally in phase with the incident waves. These phase changes can be modeled in the frequency domain using complex-valued reflection and diffraction coefficients.

3.3 Attenuation of Sound by Air

Apart from energy losses taking place at the walls, there are various mechanisms that attenuate sound waves propagating in air (or any other fluid). In room acoustics, these effects are negligible in many situations and become significant only in large rooms and at relatively high

frequencies [74, p. 160]. An introductory description of the physics of these loss mechanisms can be found in [31, Ch. 7.2] and will not be discussed here. In the context of the current work, it is sufficient to know that air propagation loss attenuates the pressure amplitude according to an exponential law, as follows [74, p.12]:

$$p(r,t) = \frac{P_0}{r} \exp(i(\omega t - kr)) \exp(-mr/2) \quad (3.6)$$

m is called the air attenuation exponent and is a function of temperature, relative humidity and frequency. It is often integrated, mathematically, into the wave number to form an imaginary wave number:

$$k = \frac{\omega}{c} - i \frac{m}{2} \quad (3.7)$$

The new beam-tracing model accounts for air attenuation in octave bands.

3.4 Modeling Specular Reflections

At each point on a wall-air interface, the component of velocity in the direction normal to the boundary should be equal for both the wall and air. This ensures that the two media remain in contact along their interface. Another interface boundary condition is obtained by applying Newton's second law of motion. This condition usually reduces to continuity of pressure (or stress in the case of an elastic solid), because the interface is assumed to be massless. As a result of these boundary conditions, an accurate model of the interaction needs to account for the entire wave field both inside and outside the wall.

In this section, we consider the reflection of a planar sound wave from the surface of a wall with infinite lateral extent and uniform properties. The assumption of uniform properties means that the wall impedance is not a function of position, ensuring that plane waves are only reflected specularly [43]. Moreover, a wall with finite lateral extent would necessarily have

edges that scatter sound in all directions. The assumptions of infinite lateral extent and uniform properties therefore ensure that incident waves are reflected wholly specularly from the surfaces of the wall. Non-specular reflections are discussed in the next section.

In the first part of this section, descriptors of the acoustical properties of surfaces are defined and basic relations among them are derived. This part concerns the study of the sound field inside the room (outside the wall). Subsequently, a general method for modeling sound propagation in multilayer walls – the transfer-matrix algorithm – is introduced, which concerns the study of the sound field inside the wall.

3.4.1 Derivation of Basic Relations

Because plane waves are functions of one independent spatial coordinate only, it can be assumed, without loss of generality, that the wall normal and the normal of the incident wave lie in the x-y plane of a rectangular coordinate system, as shown in Figure 3.1. For this configuration, the classical solution of the wave equation can be written as follows:

$$p(x, y, t) = f(t - x \cos \theta / c - y \sin \theta / c) + g(t + x \cos \theta / c - y \sin \theta / c) \quad (3.8)$$

$$u_x(x, y, t) = \frac{\cos \theta}{\rho c} (f(t - x \cos \theta / c - y \sin \theta / c) - g(t + x \cos \theta / c - y \sin \theta / c)) \quad (3.9)$$

Since impedance is defined as the ratio between pressure and particle velocity in the frequency domain, we need to transform Eqs. (3.8) and (3.9) to the frequency domain. The following Fourier-transform convention will be used throughout this thesis:

$$F(f(t)) = \hat{f}(\omega) = \int_{-\infty}^{+\infty} f(t) e^{-i\omega t} dt \quad (3.10a)$$

$$F^{-1}(\hat{f}(\omega)) = f(t) = \frac{1}{2\pi} \int_{-\infty}^{+\infty} \hat{f}(\omega) e^{i\omega t} d\omega \quad (3.10b)$$

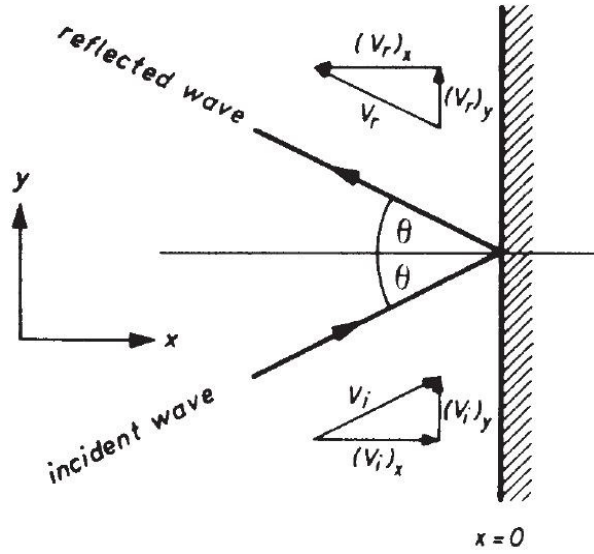


Figure 3.1. Reflection of plane waves from a uniform wall [74].

Because the exponential term in the integrand of the inverse Fourier transform, Eq. (3.10b), has a negative sign, this convention is equivalent to positive time dependence in complex notations, as in Eq. (3.1). Using Eq. (3.10a), one can easily show that, for a constant τ ,

$$F(f(t - \tau)) = \hat{f}(\omega)e^{i\omega\tau} \quad (3.11)$$

Taking the Fourier transform of Eqs. (3.8) and (3.9), and using Eq. (3.11), gives:

$$\hat{p}(x, y, \omega) = \hat{f}(\omega)\exp(x\cos\theta/c + y\sin\theta/c) + \hat{g}(\omega)\exp(-x\cos\theta/c + y\sin\theta/c) \quad (3.12)$$

and,

$$\hat{V}_x(x, y, \omega) = \left(\begin{array}{l} \hat{f}(\omega)\exp(x\cos\theta/c + y\sin\theta/c) \\ -\hat{g}(\omega)\exp(-x\cos\theta/c + y\sin\theta/c) \end{array} \right) \frac{\cos\theta}{\rho c} \quad (3.13)$$

The impedance boundary condition is defined as:

$$Z = \left(\frac{\hat{p}}{\hat{V}_x} \right)_{\text{surface}} = \frac{\hat{p}(0, y, \omega)}{\hat{V}_x(0, y, \omega)} \quad (3.14)$$

Substituting Eqs. (3.12) and (3.13) into Eq. (3.14),

$$Z = \frac{\rho c}{\cos \theta} \frac{\hat{f}(\omega) + \hat{g}(\omega)}{\hat{f}(\omega) - \hat{g}(\omega)} = Z(\omega, \theta) \quad (3.15)$$

As expected, the value of impedance does not depend on y .

The reflection coefficient is defined as the ratio of the amplitudes of the reflected wave and the incident wave:

$$R = \frac{\hat{g}(\omega)}{\hat{f}(\omega)} \quad (3.16)$$

Dividing both the numerator and denominator of Eq. (3.15) by $\hat{f}(\omega)$ and rearranging the terms, the relations between the impedance and reflection coefficient can be found as:

$$Z = \frac{\rho c}{\cos \theta} \frac{1+R}{1-R} \Leftrightarrow R = \frac{Z \cos \theta - \rho c}{Z \cos \theta + \rho c} \quad (3.17)$$

or in terms of specific impedance, ζ ,

$$\zeta = \frac{1}{\cos \theta} \frac{1+R}{1-R} \Leftrightarrow R = \frac{\zeta \cos \theta - 1}{\zeta \cos \theta + 1} \quad (3.18)$$

Both impedance and reflection coefficient are generally functions of frequency and the angle of incidence, and have complex values. Consequently, to characterize a wall with uniform properties, one needs to know the (complex) value of either the impedance or the reflection coefficient for every angle of incidence, and every frequency, of interest. When applicable, simplifying assumptions are made in order to reduce the amount of data required for the analysis of the problem. Regarding the angular dependence, one can assume that either the reflection coefficient or the impedance do not vary with the angle of incidence¹. Regarding frequency dependence, however, such assumptions are not common. Rigid and soft walls are very special

¹ Note that because of the $\cos(\theta)$ term in Eq. (3.17), at least one of the impedance and reflection coefficient has to vary with the angle of incidence.

cases for which the impedance depends neither on the frequency nor the direction of the incident sound.

Absorption coefficient, α , is defined as the ratio of the absorbed and incident sound energies. If we do not differentiate between the amount of energy that is transmitted through the wall and the amount of energy that is lost inside it, the absorption and pressure-reflection coefficients can be related to each other as follows:

$$\alpha = 1 - |R|^2 \quad (3.19)$$

This definition represents the portion of the incident energy that is not reflected back from the wall into the room. The absorption coefficient does not include any phase information regarding the process of reflection. It is a real number and, generally, a function of frequency and the angle of the incident sound. Using Eqs. (3.19) and (3.18), the absorption coefficient can be expressed in terms of the specific impedance as follows:

$$\alpha = \frac{4 \operatorname{Re}(\zeta) \cos \theta}{|\zeta|^2 \cos^2 \theta + 2 \operatorname{Re}(\zeta) \cos \theta + 1} \quad (3.20)$$

3.4.2 Transfer-Matrix Modeling of Multilayer Walls

When an acoustic wave acts on the surface of an interface, it tends to force some air through it. This brings about wave motion in the material forming the surface, provided that it is possible for the fluid to move normal to the surface [97]. Consequently, the motions of the points on the surface are related to each other, as imposed both by the wave motion inside the material and by the incident and reflected waves. The influence of the incident and reflected waves was studied in section 3.4.1. Here, the focus is on the wave motion inside the material: a simple method of modeling sound propagation in multilayer walls is presented.

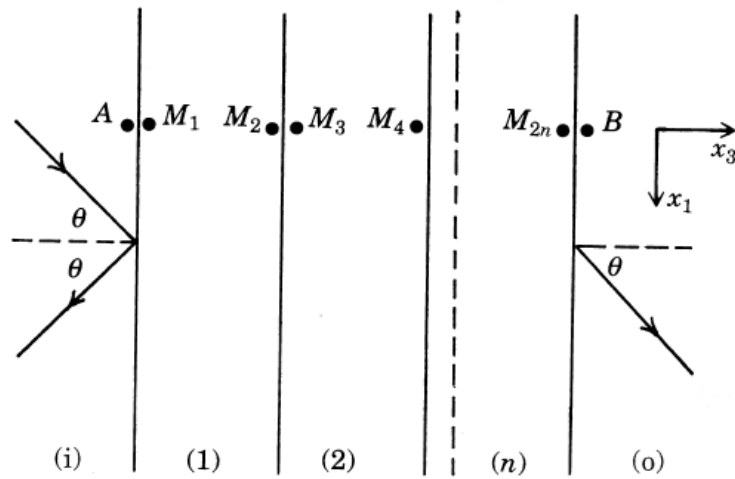


Figure 3.2. Profile view of a multilayer wall [17].

Consider a layered wall of finite thickness and infinite lateral extent, as shown in Figure 3.2. Each layer can be either a fluid, an elastic solid, or a poroelastic material (a porous material with an elastic frame). Propagation of plane sound waves in such a layered medium can be described using a transfer-matrix model, as proposed by Brouard *et al.* [17].

The model relates the properties at the two sides of the layered wall, points A and B in Figure 3.2, through a matrix equation, as follows:

$$V(A) = T \cdot V(B) \quad (3.21)$$

Vectors $V(A)$ and $V(B)$ contain the properties at points A and B, respectively, and T is the transfer matrix of the wall. Properties needed for each material are the normal component of velocity (along x_3) and the stress components. Sound propagation within each layer is written in a matrix format which relates the properties at the two ends of the layer - points M_1 and M_2 , for example. At the boundary of two adjacent layers - points M_2 and M_3 - the properties are related such that the displacement field remains continuous and no net force exists. Proper assembly of these matrices results in T , which “transfers” the properties at one end of the layer to the other end. Knowing the properties at the end of the layers - point B - the impedance at point A can easily be calculated using the transfer matrix, T . Point B is usually considered to be a semi-infinite layer of

air, or a rigid surface. The transfer-matrix approach is very general and can be used as long as the propagation of sound within each layer and through the boundaries between the layers is linear.

The transfer-matrix approach has been implemented in MATLAB by Wareing [133]. For validation, he compared the transfer-matrix prediction of surface impedances and reflection coefficients either to predictions by other known theories or with experimental results in the literature, with very good agreement. He then incorporated the transfer-matrix in his beam-tracing model in order to investigate the significance of modeling the surfaces of a room as of local- and extended-reaction on the steady-state response of the room; the results of this research can be found in [52].

3.5 Modeling Diffuse Reflections

In the previous section, we considered specular reflection of sound waves from surfaces. Real surfaces, however, very often scatter sound energy in all directions. This redirection of (a portion of) the sound energy from the specular direction into non-specular directions is called diffuse reflection. In the new beam-tracing model, diffuse surface reflections are accounted for according to Lambert's law in the same way as in the existing ray-tracing model.

According to this approach [45], surfaces are considered to diffuse the incident sound partially, as quantified by the diffuse reflection coefficient, d , taking values between 0 and 1. A surface reflects a portion d of the incident sound such that equal sound intensities are reflected in all directions (Lambert's law), and the remaining $1-d$ portion is reflected specularly. Ideally, this concept would be implemented in the (ray- or) beam-tracing model such that when a beam hits a surface, multiple beams are reflected from it in one specular direction and multiple non-specular directions. This, unfortunately, is very inefficient computationally. Instead, a random number is generated upon each reflection (Monte Carlo approach), to determine whether the reflection is

specular or diffuse. If the random number is bigger than the corresponding diffuse-reflection coefficient, then the reflection is considered specular; otherwise, the incident beam is reflected diffusely. As a result, a wall reflects all incident beams diffusely if $d = 1$; likewise, wholly-specular reflection is characterized by $d = 0$.

In the case of diffuse reflections, the direction of reflection is determined by two random numbers which are used to determine the inclination and azimuthal angles of the reflected direction with respect to a local spherical coordinate system located at the point of reflection (center ray of the beams). In order to ensure Lambert's law is respected, the inclination angle is chosen as the inverse cosine of the square root of a random number generated uniformly in the interval $(0, 1)$. The azimuthal angle, on the other hand, is chosen randomly from the interval $(-\pi, \pi)$.

This realization of Lambert's law was first proposed by Kuttruff in 1971 [71]. It should also be noted that the use of Lambert's law has the potential to cause prediction errors "particularly acute for the early sound field" [22, p. 413].

3.6 The Transient Response

Under the assumption of source and receiver immobility, the acoustical space in which they are placed can be considered a linear, time-invariant system [114]. Such a system can be uniquely represented either in the frequency domain (by its transfer function) or in the time domain (by its impulse response) – see, for example, [131, p.107]. The impulse response represents the transient response of a room, and the transfer function represents its steady-state response. In this section, we first discuss different ways of expressing the temporal response of a room. We then continue with the relation between the transfer function and the impulse response of a room, and explain the way impulse responses are calculated in the new beam-tracing model.

It should be noted that the measurement of impulse responses is not addressed in this thesis; see [114] for a discussion of different impulse-response measurement techniques.

3.6.1 Impulse Responses and Echograms

The acoustical impulse response of a room is often considered one of its most important characteristics, because it contains all information about the acoustics of that room between the corresponding source and receiver positions. Various room-acoustical parameters that correlate with subjective perception of sound can also be derived directly from the impulse response, as will be described in section 3.7. Furthermore, impulse responses are often used in auralization in order to recreate the aural impression of the acoustic characteristics of a space [68]. This is done by convolving the impulse response of the space with a sound signal recorded in an anechoic environment – for further details about auralization refer to [68] and [131].

What is usually meant by the impulse response of a room is the temporal variation of the acoustic pressure at a stationary receiver point after the source emits a vanishingly short impulse with non-vanishing energy; in other words, the signal obtained at the receiver position after the source is excited by a Dirac delta function [74, p.255]. We hereafter use the term “pressure impulse response” for the quantity defined in this way. The word pressure has been added to distinguish it from another form of impulse response, the “energy impulse response”. The energy impulse response is simply the square of the pressure impulse response. The rationale for such a naming is that pressure squared is proportional to sound energy. An energy impulse response contains less information about the signal than a pressure impulse response, because the signs of pressure values cannot be retrieved once they have been squared. Since they express a physical parameter (pressure), the pressure and energy impulse responses of a room have real values.

Another way of describing the temporal response of rooms is by an echogram, which is an approximation to the energy impulse response [73]. For each beam detected by a tracing

algorithm, the beam's path length from the source to the receiver is stored. Divided by the speed of sound, a beam's path length represents the beam's time of arrival at the receiver point. Using this information, an echogram is obtained at a receiver point by plotting the energy of the received beams versus their arrival times. An echogram is plotted in Figure 3.3.

For a concise, mathematical presentation of an echogram, one can consider the energy of each arriving beam represented by a Dirac delta function at the time of arrival. The echogram, $e(t)$, can then be written as a sum over all detected beams at the receiver point, according to Eq. (3.4), as follows:

$$e(t) = p_0^2 \sum_b \frac{|R_{eff,b}|^2}{L_b^2} \delta(t - L_b / c) \quad (3.22)$$

Here the index b represents the beams detected at the receiver point.

If the direct path between the source and the receiver is not blocked, the first component of an echogram represents the direct sound which arrives at the receiver without having been affected by the room. This is usually the strongest component of the echogram and arrives after a time delay called the initial gap. The direct sound is followed by components that have been reflected by room boundaries, with their temporal densities increasing rapidly. Reflected waves carry less energy as time progresses because a fraction of their energies are absorbed every time they hit a surface, and due to spherical spreading and air absorption.

Regarding the subjective hearing impression of the sound field, the first reflections have different effects than the numerous weak reflections arriving at later times [73]. The early portion is of crucial importance for the sensations of loudness, clarity and spaciousness of the sound field, as well as its directional structure. The late portion, on the other hand, is more important for the gross temporal and spectral characteristics, rather than the fine structure of the sound field. It consists of many overlapping reflections and is known as reverberation.

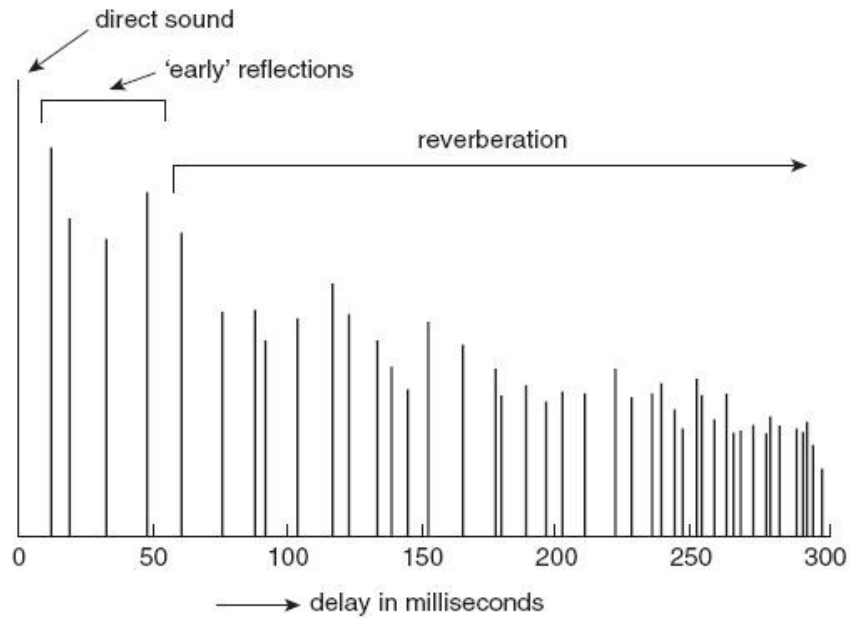


Figure 3.3. An echogram [74].

3.6.2 The relation between the pressure impulse response and the transfer function

The Fourier transform of the pressure impulse response is the transfer function (of the room) between the source and the receiver. For discrete signals, certain relations hold between a signal in the time domain and its (discrete) Fourier transform in the frequency domain – see Figure 3.4. These rules are summarized below [113]:

$$\begin{aligned}
 \omega_c &= 2\pi f_c = K\Delta\omega = K(2\pi \Delta f) \\
 \Delta t &= \frac{2\pi}{\omega_c} = \frac{1}{f_c}, \quad T_c = \frac{2\pi}{\Delta\omega} = \frac{1}{\Delta f} \\
 f_N &= \frac{1}{2\Delta t}
 \end{aligned}
 \tag{3.23}$$

When going from the frequency to the time domain, the size of the time window, T_c , determines the lowest frequency that can be represented in the frequency domain and, therefore, the frequency resolution, Δf . The sampling rate, Δt , determines the highest frequency that can be represented in the frequency domain, f_c . The first frequency-domain component corresponds to

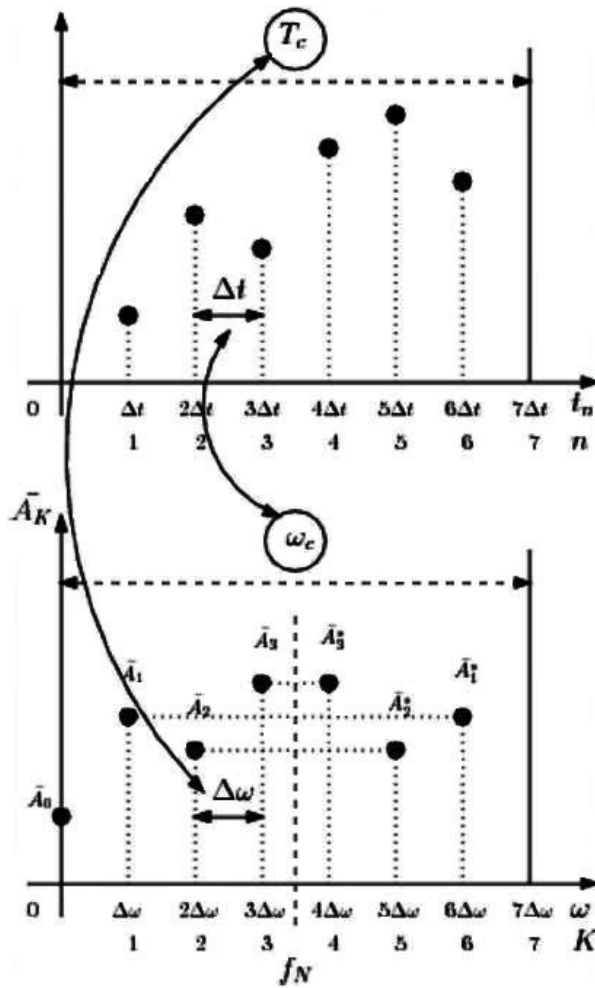


Figure 3.4. Relations between the time- and frequency-domain windows [113].

the DC component of the time-domain signal. This is followed by complex components, up to the Nyquist frequency, f_N , and then by the complex conjugates of these numbers in the reverse order. Therefore, the discrete Fourier transform of the pressure impulse response has an odd length.

Using the beam-tracing model, the transfer function is calculated with a frequency resolution Δf , and to an upper frequency f_c . The transfer function is then inverted to the time domain using the inverse-Fourier-transform function in MATLAB, *ifft*. While preparing the data for the inverse transformation, it should be noted that the result of the transformation must be real-valued. In order to ensure this, the transfer function must be preceded by a zero and

followed by its complex conjugate in the reverse order, before being transformed into the time domain.

3.6.3 Octave-Band Impulse Responses

In order to calculate octave-band pressure impulse responses, the pressure impulse response of the room (the inverse Fourier transform of the transfer function) must be properly filtered for that frequency bandwidth. This can be done by either convolving the pressure impulse response with the time-domain signal of the filter or, alternatively, by taking the inverse Fourier transform of the product of the transfer function of the room and the filter in the frequency domain. In this research, we will perform the filtering in the frequency domain; i.e. the transfer function is multiplied by an octave-band filter in the frequency domain and the product is then transformed to the time domain.

Perhaps the simplest band-pass filter to use in the frequency domain is a rectangular filter. An octave-band rectangular filter has the value zero everywhere except at frequencies within the corresponding bandwidth. For example, for calculating the 250-Hz octave-band pressure impulse response, the value of the transfer function outside the frequency range of 177 to 355 Hz is set to zero before transforming it to the time domain.

A property of the Fourier transform of a function is that the narrower is the function in one domain, the wider it is in the other domain [41]. The extreme case is a Dirac delta function, which has a constant (infinitely-wide) Fourier transform. This is a mathematical phenomenon associated with the interdependence of time- and frequency-domain representations of a function, allowing it to be an arbitrary function of time or frequency, but not both together [13]. This property is known as the uncertainty principle or relation, and dictates the following restriction on the time width, Δt , and the frequency bandwidth, Δf , of a signal:

$$\Delta t \cdot \Delta f \geq 0.5 \tag{3.24}$$

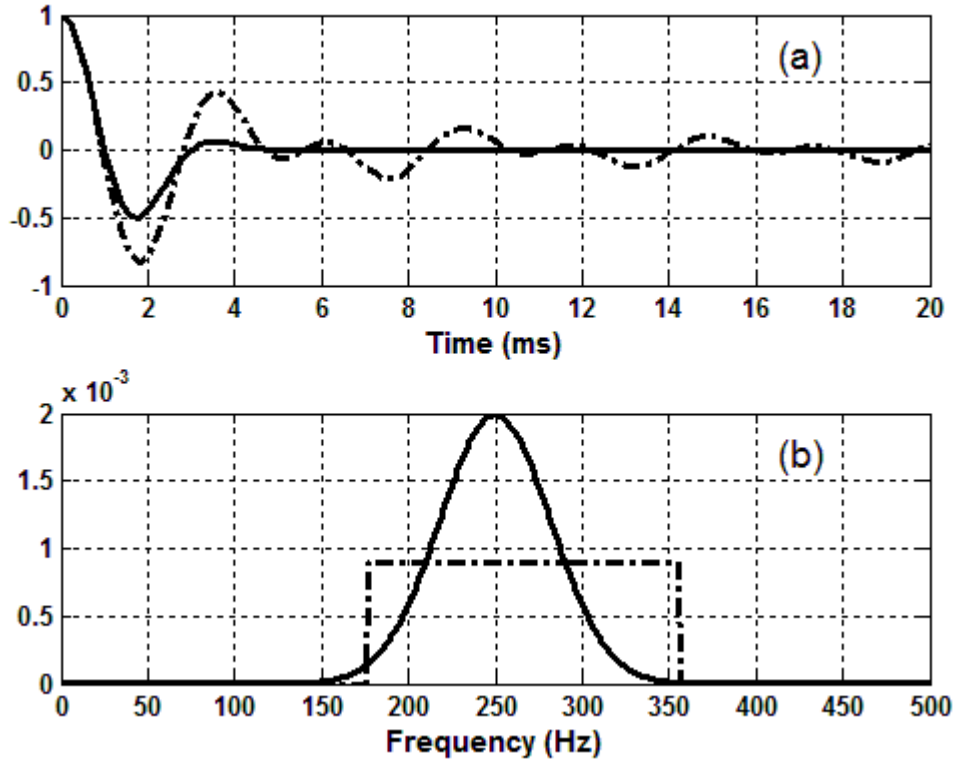


Figure 3.5. Octave-band Gabor and rectangular pulses at 250 Hz in: a) time domain, and b) frequency domain. Solid line: Gabor pulse; dashed line: rectangular pulse.

For further details, and a proof, of the uncertainty principle, see [13, pp.160-163].

When the time-domain characteristics of a function are of interest, as is the case here with pressure impulse responses, one would ideally desire a signal with the shortest time-width possible for a given frequency bandwidth, so that a better time resolution is achieved. Given a frequency bandwidth, the time-width is twice the minimum value possible when using a filter with rectangular spectrum in the frequency domain [119]. The shortest possible time duration can be obtained using a Gaussian signal (which has a Gaussian spectrum as well) [119, 41]. Following Suh and Nelson [119] we call this signal a Gabor pulse. Its Fourier transform, which we accordingly call a Gabor filter, is given by:

$$G(f) = \frac{\sqrt{2}}{4} \frac{1}{\Delta f} \left(\exp\left(-\frac{\pi^3}{2} \left(\frac{f + f_0}{\Delta f}\right)^2\right) + \exp\left(-\frac{\pi^3}{2} \left(\frac{f - f_0}{\Delta f}\right)^2\right) \right) \quad (3.25)$$

Here f_0 is the center frequency of the octave band and Δf is its bandwidth. Figure 3.5 shows octave-band Gabor and rectangular pulses at 250 Hz in the time and frequency domains.

Suh and Nelson [119] argue that, since real sound sources become directional as the frequency increases, Gabor pulses are the optimal source signals for comparison of measurements with prediction results, because they have the shortest time resolution for the frequency bandwidth in which the source is omnidirectional. Unless otherwise stated, a Gabor filter is used in this research for calculation of octave-band parameters.

3.7 Room-Acoustical Parameters

Apart from respecting certain laws of physics, the sound field in a room should satisfy its occupants. In order to quantify a listener's subjective impression of a room's sound field, several quantities have been defined which correlate with particular subjective aspects of the acoustical characteristics of the sound field. Some of these parameters, hereafter referred to as room-acoustical parameters, will be very briefly introduced in this section; for more details, see [36, Ch. 9.3]. What the room-acoustical parameters have in common is that they are all derived by post-processing of the pressure impulse response of the room. Unless otherwise cited, the material presented here is taken from [140] and [74, Ch. 7]. The new beam-tracing algorithm is capable of calculating all of the parameters introduced in this section.

Reverberation, regarded as the most characteristic acoustical phenomenon in a closed room by Kuttruff, refers to the fact that sound generated in a room will not disappear immediately after the sound source is shut off, but remains audible for a certain period of time afterwards, although with steadily decreasing loudness. The descriptor of the rate of this decay is the reverberation time, which is the time required for the sound energy to decrease by a factor of 10^6 , equivalent to 60 dB. This time is usually denoted by T_{60} , the number 60 emphasizing the 60-dB drop. Reverberation time, however, can be evaluated based on a smaller range than 60 dB,

but is always extrapolated to a decay time of 60 dB. If reverberation time is derived between the times at which the sound level decreases 5 and 25 dB below the initial level, it is labelled T_{20} . If decay values of 5 to 35 dB below the initial level are used, it is labelled T_{30} . If the initial 10 dB of the decay is used, it is labelled EDT, for early decay time. EDT is most relevant subjectively and is related to the perceived reverberance. The other reverberation times are more related to the physical properties of the room.

All reverberation times are determined from the slope of the decay curve, which is obtained by plotting the sound level in the room versus time after the sound source is turned off. The slope is that of the best-fit linear-regression line between the levels corresponding to each parameter; for example, between 0 and -10 dB for EDT. The decay times should then be calculated as the time required for a 60-dB decay, using this slope.

Reverberation curves or sound-decay curves were traditionally obtained using electromechanical level recorders. Fortunately, however, Schroeder [111] has shown that the sound-decay curve, $SD(t)$, can be calculated with increased statistical accuracy by backward integration of the pressure impulse response as follows:

$$SD(t) = 10 \log \frac{\int_0^{\infty} p^2(t) dt}{\int_t^{\infty} p^2(t) dt} \quad (3.26)$$

This method is called backward integration because the upper integration limit is not known; originally proposed in the days of magnetic tape recorders, the integration was done by playing the tape backwards [36].

Definition, D_{50} , is a descriptor of the distinctive of sound and is defined as follows:

$$D_{50} = \frac{\int_0^{50ms} p^2(t) dt}{\int_0^{\infty} p^2(t) dt} \cdot 100\% \quad (3.27)$$

Definition will be 100% if the impulse response does not contain any components with delays more than 50 ms. It was the earliest parameter introduced to define an objective criterion of the distinctness of sound. The just-noticeable difference in D_{50} is 5% and its typical range is from 5 to 35%².

A parameter which correlates with the perceived clarity of sound is the early-to-late energy fraction C , defined as follows:

$$C_T = 10 \log_{10} \frac{\int_0^T p^2(t) dt}{\int_T^{\infty} p^2(t) dt} \quad (3.28)$$

This is usually calculated for T values of either 50 or 80 ms, depending on whether the results are intended to relate to conditions for speech or music, respectively. C_{80} is called clarity index and is widely accepted as a useful criterion for the clarity and transparency of musical sounds in concert halls. The just-noticeable difference in C_{80} is 1 dB and its typical values range from -5 to 5 dB.

Center time, T_s , is defined as the first moment of the squared impulse response:

$$T_s = \frac{\int_0^{\infty} t p^2(t) dt}{\int_0^{\infty} p^2(t) dt} \quad (3.29)$$

A reflection with given strength contributes more to T_s , the longer it is delayed with respect to the direct sound, because it would be farther from the “center of gravity” of the squared impulse

² All typical ranges reported in this section correspond to frequency-averaged values at single positions in unoccupied concert and multi-purpose halls up to 25,000 m³.

response. High transparency or speech intelligibility corresponds to low values of the center time. The just-noticeable difference in center time is 10 ms and it typically ranges from 60 to 260 ms.

The modulation transfer function, MTF, has been shown by Houtgast and Steeneken to be a good predictor of speech intelligibility in rooms [54, 57]. It has been shown by Schroeder [112] that the MTF, $m(F)$, and a room's pressure impulse response, $p(t)$, are related via the Fourier transform as follows:

$$m(F) = \frac{\int_0^{\infty} p^2(t) \exp(-2i\pi Ft) dt}{\int_0^{\infty} p^2(t) dt} \quad (3.30)$$

Furthermore, the MTF can be converted into a single index, Speech Transmission Index (STI), which is found to correlate well with intelligibility scores for a wide variety of speech signals. Conversion of the MTF into STI involves calculation of $m(F)$ in seven octave bands from 125 Hz to 8kHz, each involving averaging 14 values for modulation frequencies of 0.63 to 12.5 Hz in third-octave intervals. Details of this conversion can be found in [56]. In this research, we use an approximation to the full STI which is called RASTI, for RAPid Speech Transmission Index.

First introduced in 1984 [55], RASTI was originally developed for the purpose of the fast evaluation of speech transmission in auditoria and for estimating the effectiveness of a public-addressing system [56]. Only the two octave bands 500 Hz and 2 kHz are used in calculation of RASTI. At 500 Hz, values of the modulation index, m , are calculated for four modulation frequencies: 1, 2, 4 and 8 Hz. At 2000 Hz, five modulation frequencies are used: 0.7, 1.4, 2.8, 5.6 and 11.2 Hz. Each of these nine values is then converted into an apparent signal-to-noise ratio level as follows:

$$(S/N)_{app} = 10 \log \frac{m}{1-m} \quad (3.31)$$

These levels are then limited to a 30-dB range by truncating the values exceeding the range of ± 15 dB. The resulting signal-to-noise ratios are averaged and the result, $\overline{(S/N)_{app}}$, is converted into a RASTI value, as follows:

$$RASTI = \frac{1}{30} \left(\overline{(S/N)_{app}} + 15 \right) \quad (3.32)$$

Sound strength, G , is a steady-state measure that corresponds the total energy in the impulse response relative to that in a free field at a distance of 10 m from the sound source. G can be expressed as follows:

$$G = \frac{\int_0^{\infty} p^2(t) dt}{\int_0^{\infty} p_{10}^2(t) dt} \quad (3.33)$$

Here, $p_{10}(t)$ is the pressure impulse response of the source measured in a free field at a distance of 10 m. The sound strength correlates with the perceived loudness of the sound, which is important since high clarity or definition are not achievable if the sound is too weak to be heard at a comfortable loudness. The just-noticeable difference in G is 1 dB and it typically ranges from -2 to +10 dB.

Bass ratio, BR, is defined as a measure of the bass reverberation of the room, which is perceived as warmth [85]. Originally introduced by Beranek in 1962 [3, p.435], BR expresses the ratio between the average low- and mid-frequency reverberation times, and is defined as follows:

$$BR = \frac{T_{60}(125) + T_{60}(250)}{T_{60}(500) + T_{60}(1000)} \quad (3.34)$$

Recommended values for BR are 1.1 to 1.25 for music halls with reverberation times of around 2.2 s, and 1.1 to 1.45 for reverberation times of 1.8 s or less [4, p.430]. BR, however, was later found to be unrelated to the subjective acoustical quality of the sound field [5]: experiments

using simulated sound fields carried out by Bradley *et al.* [16] indicated that the perceived strength of bass sound is related to the level of both the early- and late-arriving sound levels, but not to low-frequency reverberation times. For this reason, study of BR values has been omitted from this report.

There are two parameters used as measures of the acoustical conditions on performance stages from the musicians' points of view. The first parameter, early support, is defined as the decibel ratio of the reflected energy within the first 0.1 s relative to the direct and floor-reflected energies, measured at a distance of 1 m from an omnidirectional sound source:

$$ST_{Early} = 10 \log \frac{\int_{0.010}^{0.100} p_{1m}^2(t) dt}{\int_0^{0.020} p_{1m}^2(t) dt} \quad (3.35)$$

Here $p_{1m}(t)$ is the pressure impulse response at a distance of 1 m from the source. The second parameter, late support, is defined as the decibel ratio of the reflected energy within the first 0.1 s relative to the direct and floor-reflected sound, measured at a distance of 1 m from an omnidirectional source:

$$ST_{Late} = 10 \log \frac{\int_{0.100}^{1.000} p_{1m}^2(t) dt}{\int_0^{0.100} p_{1m}^2(t) dt} \quad (3.36)$$

Both support parameters relate to the extent to which the room supports the musician's efforts to create music on their own instruments: whether they find it easy to play together (early support), or whether they have to force their instruments to fill the room (late support). While early support relates to the musicians' ease of hearing other members of the orchestra, late support relates to the perceived reverberance of the hall as heard by the musicians. Both support parameters are typically measured the octave bands 250, 500, 1000 and 2000 Hz. Their typical

values range from -24 to -8 dB for early support and -24 to -10 dB for late support. For classical music, values of -14 to -10 dB are suggested for early support [36].

3.8 Edge Diffraction

Diffraction of sound around wedges has been modeled using two formulations: the uniform theory of diffraction (UTD) [69] and the model developed by Svensson *et al.* [122] (Svensson's model). The former is the model used in the existing ray-tracing model, and the latter is the model which is proposed to be used in the new beam-tracing model. In this section, the two models are introduced briefly.

3.8.1 Svensson's Model

Svensson's model gives the solution for the first-order diffraction from a finite wedge as a line integral along its edge, which has the benefit of allowing for simulations of finite and infinite wedges with the appropriate choice of integration limits. A wedge formed at the intersection of two rigid surfaces acts as a secondary source when hit by a sound wave. The edge therefore acts as a collection of infinitesimal secondary sources of sound and radiates in every direction. The wave front that radiates from the edge is modeled in the time domain with an impulse response, which is a function of the geometry of the edge and the positioning of the source and receiver.

The continuous-time formulation of the diffraction impulse response, $h_{diff}(t)$, for the configuration in Figure 3.6, is given as follows [120]:

$$h_{diff}(t) = -\frac{\nu}{4\pi} \sum_{i=1}^4 \int_{z_1}^{z_2} \delta\left(t - \frac{m+l}{c}\right) \frac{\beta_i}{ml} dz \quad (3.37)$$

Here, $\nu = \pi/\theta_W$ is the wedge index, with θ_W being the exterior wedge angle. A local cylindrical coordinate system (r, θ, z) is used, where r is the radial distance from the edge, θ is

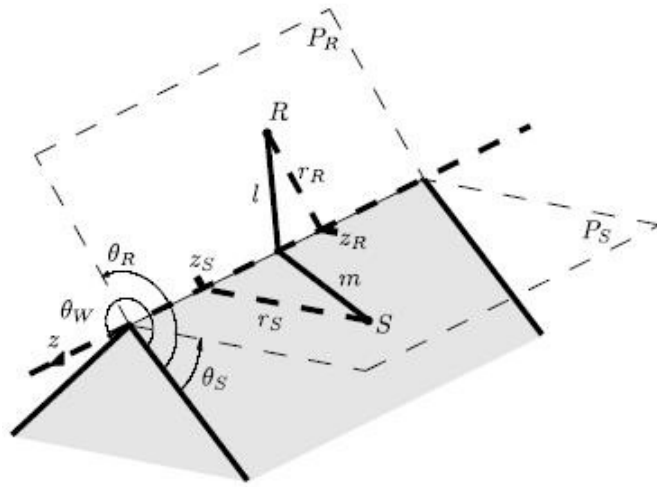


Figure 3.6. Wedge geometry and coordinate system. P_S and P_R are the planes containing the edge and the source and receiver, respectively [120].

measured from one of the faces of the wedge and the z -axis is aligned with the edge of the wedge. The integration limits z_1 and z_2 are the z -coordinate values of the two ends of the edge. For an infinite wedge, the integration is carried out with both limits at infinity. m and l are the distances, respectively, from the source, S , and receiver, R , to a point on the edge:

$$m = \sqrt{r_S^2 + (z - z_S)^2}, \quad l = \sqrt{r_R^2 + (z - z_R)^2} \quad (3.38)$$

β_i are the secondary-source directivity functions defined as below:

$$\beta_i = \frac{\sin(v\varphi_i)}{\cosh(v\eta) - \cos(v\varphi_i)} \quad (3.39)$$

The angles φ_i are:

$$\begin{aligned} \varphi_1 &= \pi + \theta_S + \theta_R, & \varphi_2 &= \pi + \theta_S - \theta_R, \\ \varphi_3 &= \pi - \theta_S + \theta_R, & \varphi_4 &= \pi - \theta_S - \theta_R \end{aligned} \quad (3.40)$$

and the auxiliary function η is:

$$\eta = \cosh^{-1} \frac{(z - z_S)(z - z_R) - ml}{r_S r_S} \quad (3.41)$$

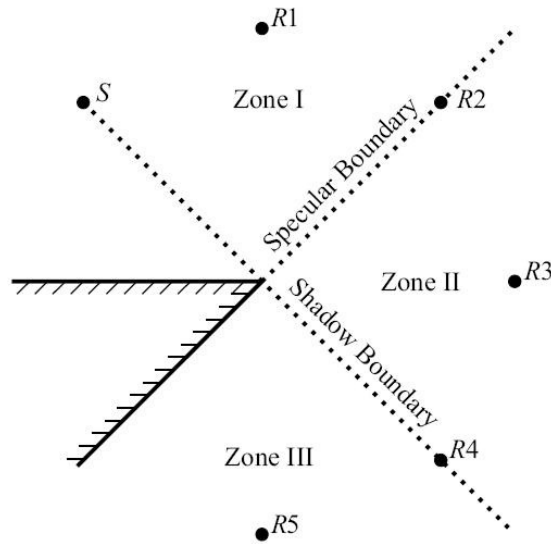


Figure 3.7. The three zones formed around a diffracting edge when the diffracted sound is not present [120].

β_i are called directivity functions because η , and therefore β_i , can be written as a function of the entrance and exit angles towards and from the edge point [121]. For compactness, the dependences of β_i , m and l on the integration variable z are not written out explicitly.

The frequency-domain formulation of Svensson's diffraction model can be obtained by taking the Fourier transform of the time-domain expression in Eq. (3.37). The result is the edge-diffraction transfer function [121], $H_{diff}(\omega)$:

$$H_{diff}(\omega) = -\frac{v}{4\pi} \sum_{i=1}^4 \int_{z_1}^{z_2} \exp(-jk(m+l)) \frac{\beta_i}{ml} dz \quad (3.42)$$

Note that a time function $\exp(i\omega t)$ is assumed here, but omitted.

When diffraction of sound is not taken into account, the sound-pressure field becomes discontinuous due to reflection and obstruction of the incident sound wave. This is depicted in Figure 3.7. A receiver in Zone I, $R1$, receives one direct and one specularly-reflected sound wave. A receiver in Zone II, $R3$, will only receive the direct sound wave, and a receiver in Zone III, $R5$, will receive neither a direct nor a reflected wave. Zone III is therefore called the shadow region. Receivers on the zone boundaries, $R2$ and $R4$, experience discontinuity in their sound pressures. The boundary beyond which the specularly-reflected wave does not exist

(corresponding to $R2$) is called the specular boundary and is located at $\theta = \pi - \theta_S$. The boundary beyond which no sound wave reaches (corresponding to $R4$) is called the shadow boundary and is located at $\theta = \pi + \theta_S$.

These discontinuities in the pressure field are compensated for by the sound field caused by edge diffraction. As a consequence, the diffracted sound field is discontinuous too, although in such a way that the overall sound field becomes continuous. The zone-boundary singularities in the diffracted sound field are due to the secondary-source directivity functions, β_i , as the denominator of one or two of these terms takes the value zero, making the integrand in Eq. (3.42) singular [120]. This singularity occurs when the terms $\cosh(v\eta)$ and $\cos(v\varphi_i)$ in Eq. (3.39) both take the value 1; note that this is the only possible singularity because $\cosh(v\eta) \geq 1$ and $\cos(v\varphi_i) \leq 1$. Furthermore, the integrand is singular at zone boundaries for only one specific value of z – the point corresponding to the shortest path from the source to the receiver via the line containing the edge. This point is called the apex point and is denoted here by z_a . A two-dimensional view of the wedge configuration is given in Figure 3.8.

The z -coordinate of the apex point can be calculated from the radial and axial source and receiver coordinates as follows:

$$z_a = \frac{z_R r_S + z_S r_R}{r_S + r_R} \quad (3.43)$$

If z_a is not included within the limits of integration, the singularity does not affect the integral, and ordinary numerical techniques can be used to compute $H_{diff}(\omega)$. In order to isolate the apex point, the integration range is split into three sub-regions: one covering a small region around the apex point up to a point denoted by z_{split} , and two extending from z_{split} to each of z_1 and z_2 . The diffraction transfer function can then be written as follows [121]:

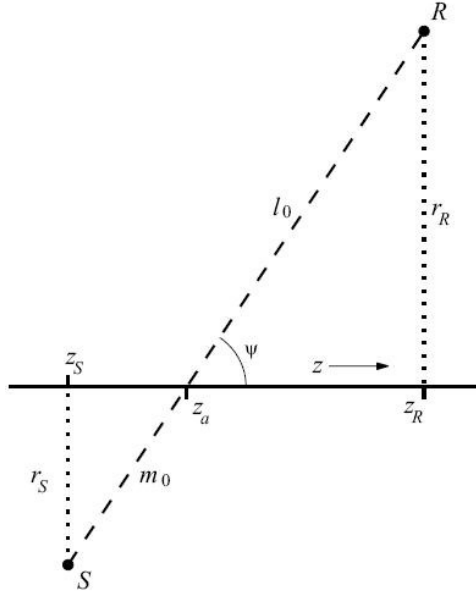


Figure 3.8. Unfolded, two-dimensional view of the wedge, along with the source, receiver and the apex point [120].

$$\begin{aligned}
 H_{diffr}(\omega) &= I_1 + I_2 + I_3 = \\
 &- 2 \times \frac{\nu}{4\pi} \sum_{i=1}^4 \int_{z_a}^{z_{split}} \exp(-jk(m+l)) \frac{\beta_i}{ml} dz \\
 &- \frac{\nu}{4\pi} \sum_{i=1}^4 \int_{z_{split}}^{z_1} \exp(-jk(m+l)) \frac{\beta_i}{ml} dz \\
 &- \frac{\nu}{4\pi} \sum_{i=1}^4 \int_{z_{split}}^{z_2} \exp(-jk(m+l)) \frac{\beta_i}{ml} dz
 \end{aligned} \tag{3.44}$$

The second and third integrals, I_2 and I_3 , have no singularities and can be handled with ordinary numerical methods. However, the first integral, I_1 , is singular, and analytical approximations of the integrand around the apex point should be used to avoid its singularity. Such approximations have been derived by Svensson and Calamia [120] and are used here. I_1 can be approximated near the apex point as follows:

$$I_1 \approx - 2 \times \frac{\nu}{4\pi} e^{-jk(m_0+l_0)} \sum_{i=1}^4 \int_{z_a}^{z_{split}} \frac{\beta_i}{ml} dz \tag{3.45}$$

As shown in Figure 3.8, m_0 and l_0 are distances from the apex point to the source and receiver, respectively. It is also required for z_{split} to satisfy the following conditions:

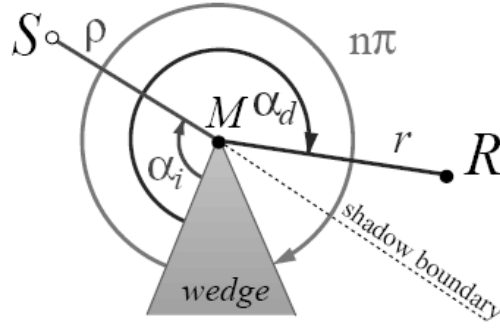


Figure 3.9. Side-view of the wedge with notations used in UTD [126].

$$z_{split} \ll \sqrt{\frac{2m_0 l_0 (m_0 + l_0)}{k(r_S + r_R)^2}}, \quad (3.46)$$

$$z_{split} \ll m_0, \quad z_{split} \ll l_0$$

Following Svensson *et al.* [121], all numerical integrations were carried out using the *quadgk* function in MATLAB using a relative tolerance of 10^{-6} . This function implements the adaptive Gauss-Kronrod quadrature and supports infinite intervals with moderate singularities at the endpoints [141].

3.8.2 The Uniform Theory of Diffraction

According to UTD³, the sound wave diffracted by a wedge, p_{diff} , can be expressed, in the frequency domain, in terms of the incident wave on its edge, $p_{incident}$, as follows:

$$p_{diff} = p_{incident} \exp(-ikr)A(r, \rho)D \quad (3.47)$$

Here, the exponential term represents phase change due to propagation from the edge to the receiver. As shown in Figure 3.9, r and ρ are, respectively, the distances from the receiver and the source to the edge. A is a scalar distance-attenuation term along the propagation path:

$$A(r, \rho) = \sqrt{\frac{r\rho}{r + \rho}} \quad (3.48)$$

D is a complex-valued diffraction coefficient accounting for amplitude and phase changes due to diffraction. It is defined as follows:

³ The material presented in this section is taken from [126].

$$\begin{aligned}
D(n, k, \rho, r, \theta_i, \alpha_i, \alpha_d) = & -\frac{\exp(-i\pi/4)}{2n\sqrt{2k\pi} \sin \theta_i} \\
& \left[\tan^{-1}\left(\frac{\pi + (\alpha_d - \alpha_i)}{2n}\right) F(kLa^+(\alpha_d - \alpha_i)) \right. \\
& + \tan^{-1}\left(\frac{\pi - (\alpha_d - \alpha_i)}{2n}\right) F(kLa^-(\alpha_d - \alpha_i)) \\
& + \tan^{-1}\left(\frac{\pi + (\alpha_d + \alpha_i)}{2n}\right) F(kLa^+(\alpha_d + \alpha_i)) \\
& \left. + \tan^{-1}\left(\frac{\pi - (\alpha_d + \alpha_i)}{2n}\right) F(kLa^-(\alpha_d + \alpha_i)) \right]
\end{aligned} \tag{3.49}$$

n , α_i and α_d are defined in Figure 3.9. θ_i is the angle between the incident direction and the edge.

The function $F(X)$ is the Fresnel integral, defined as follows:

$$F(X) = 2i\sqrt{X} e^{iX} \int_{\sqrt{X}}^{+\infty} \exp(-i\tau^2) d\tau \tag{3.50}$$

L is given by:

$$L = \frac{r\rho}{r + \rho} \sin^2 \theta_i \tag{3.51}$$

Functions $\alpha(\beta)$ are defined as follows:

$$\alpha^\pm(\beta) = 2 \cos^2 \left(\frac{2\pi N^\pm n - \beta}{2} \right) \tag{3.52}$$

where N is defined as the integer that satisfies more closely the following relations:

$$2\pi N^+ n - \beta = \pi \tag{3.53a}$$

$$2\pi N^- n - \beta = -\pi \tag{3.53b}$$

Overall, using Eq. (3.47), the diffraction coefficient predicted by UTD can be expressed as follows:

$$H_{UTD}(\omega) = \exp(-ikr) A(r, \rho) D \tag{3.54}$$

Compared to Eq. (3.44), the formulation in Eq. (3.54) does not take the length of the wedge into account.

3.9 Summary

In this chapter, the theory and structure of the new beam-tracing model were explained in some detail. Modifications have been made to the existing model in order to accommodate new algorithms inside the code and improve the existing ones. These modifications are validated in following chapter.

Chapter 4

Validation of the New Model

The new beam-tracing model is a modified and improved version of the existing beam-tracing model. The accuracy of the predicted transfer function was validated by Wareing [133] through comparison with a wave-based, method-of-images model (the image-phase model) developed by Guo and Hodgson [39]. This remains valid for steady-state predictions in rooms with specularly-reflecting walls by the new model, since the algorithm is the same. However, since wave-based and energy-based predictions of the transient responses of rooms have been implemented in the new model, the transfer function needs to be calculated over a wider frequency range, and beams need to be traced for a longer time (higher reflection order). This increases the runtimes of the predictions. More importantly, the transfer-matrix algorithm which is used for calculating the acoustical properties of the multilayer surfaces was not implemented in the Wareing model in the most computationally-efficient way, resulting in very long runtimes.

Given that one of the objectives of the current research was to study the transient responses of rooms with multilayer surfaces, an immediate priority objective was to improve the computational efficiency of the model – specifically in relation to the implementation of the transfer-matrix algorithm. Apart from computational efficiency, there are other aspects of the new model which need validation. These are the features that have been added to the existing model.

This chapter begins with the discussion of the computational efficiency of the new model. Energy- and wave-based predictions are then validated against theory for the simple case of sound propagation over a flat surface, for both specular and diffuse reflection. Next, predictions of reverberation times and steady-state sound-pressure levels are compared with measurements in a reverberant room. To ensure correct programming, the diffraction module is validated through comparison with results in the literature. The two sound-diffraction formulations considered in this work are then compared in the case of a finite-length wedge. Comparison is also made of theoretical predictions with experiments on a finite-length barrier over a flat surface in an anechoic chamber.

4.1 Computational Efficiency

The computational efficiency of the beam-tracing model was improved in three stages: coding improvements, pre-calculation of the source beams, and pre-calculation of the acoustical properties of multilayer surfaces. Of course, implementing edge diffraction into the beam-tracing model increased the runtime of the model; this will be addressed in section 4.5.

4.1.1 Coding Improvements

Minor details of the code structure were changed in order to improve its computational efficiency. In order to investigate the effects of these changes, predictions were made for a test

configuration involving the frequency range of 500 to 4000 Hz with 10-Hz increments in a room with dimensions of $3 \times 3 \times 3 \text{ m}^3$ having an average diffuse-field absorption coefficient of 0.1 for all surfaces. Using the original code of the existing beam-tracing model, this test configuration took 3 min and 47 s for 2880 beams traced for 30 reflections.

In the original model, the dot (inner) product of two vectors was calculated using MATLAB's *dot* function. This, however, is not an efficient way of calculating the dot product of two real-valued vectors. It is more efficient to use the array multiplication operator (*.**) instead. The dot-product of two arbitrary real-valued vectors was calculated 2,080,293 times using each method – this is the number of times a dot-product needs to be calculated in the test configuration. While this process took 43.2 s using the *dot* function, it took only 0.5 s using the array multiplication. Overall, the modifications made to the code decreased the runtime for the test configuration to 2 min and 35 s, a 30% improvement.

4.1.2 Pre-Calculation of Source Beams

As mentioned in section 3.1, in the beam-tracing model a spherical wave is approximated by a point source surrounded by a modified icosahedron with $20 \times f_i^2$ subdivided triangular faces. We call f_i the icosahedron frequency. At the beginning of the beam-tracing algorithm, before tracing the beams, the source beams are created according to the defined icosahedron frequency, inside the *icosa* function. The time needed for creating the source beams increases with the fourth power of the icosahedron frequency.

Minor modifications were made to the *icosa* function, which decreased its runtime, as shown in Figure 4.1. For the icosahedron frequencies used in this research, the runtimes do not impose computational restrictions. Nevertheless, the source beams were pre-calculated for different icosahedron frequencies and stored in a folder. Instead of calculating the source beams

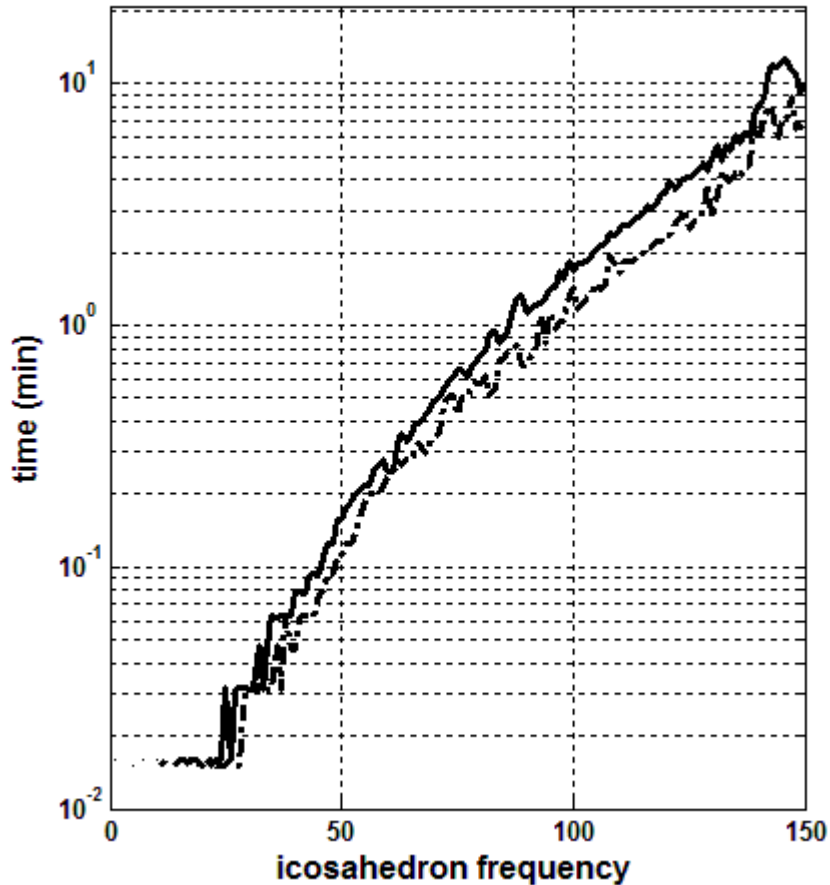


Figure 4.1. Time require for calculating the source beams as a function of the icosahedron frequency. Solid line: the existing *icosa* function; dash-dot line: the modified function.

each time the program runs, the corresponding file is called from this folder, which takes less than 0.2 s.

4.1.3 Pre-Calculation of the Acoustical Properties of Multilayer Surfaces

The most significant computational inefficiency of the existing beam-tracing model occurs in the case of rooms with multilayer surfaces. The time required for prediction of the sound field in a room with walls that are locally-reacting or have constant reflection coefficient is less than half an hour. If only one of the walls is modeled as of extended-reaction, however, the required time becomes greater than a day. The reason for this is that the acoustical properties of multilayer surfaces are calculated using the transfer-matrix algorithm, and in an inefficient

way. On each reflection, the surface impedance is calculated for every frequency and for the applicable angle of incidence. This limits the use of the model for further investigations in rooms with surfaces of extended- and local reaction.

One way of circumventing this runtime problem is to pre-calculate the acoustical properties of the surfaces which are used in a configuration, separate from the room prediction process. Before running the program, the reflection coefficient of each multilayer surface is calculated for a wide frequency range and for different angles of incidence. These data are then stored in an Excel file, and saved for use in the current prediction process, and for future use. Each Excel file contains the reflection coefficient of a multilayer configuration in 1-degree steps of angle of incidence and 0.5-Hz steps of frequency, from 0.5 to 10,000 Hz. Different files are needed for surfaces modeled as of extended- and local-reaction, each taking about half an hour to create on average, depending on the number of layers. With the acoustical properties of surfaces pre-calculated, 30 s are added to runtimes of predictions when one wall of the room is a multilayer surface.

4.2 Sound Propagation over a Flat Surface

In this section, we study the sound field of a point source over an infinitely-long, rigid, flat surface for both specular and diffuse reflection.

4.2.1 Specular Reflection

When considering specular reflections, the sound field at the receiver point comprises two components: the direct and reflected sound waves, p_d and p_r , respectively. Since the surface is assumed to be rigid, the reflected wave can be replaced by the direct wave from a mirror-image source with the same amplitude and phase. Using Eq. (3.1), the sound field is therefore described as follows:

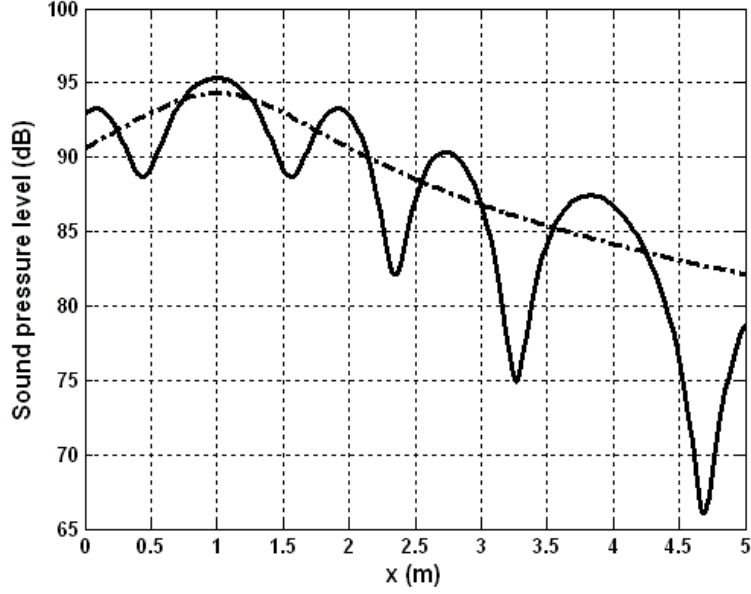


Figure 4.2. Sound pressure level over a flat, rigid surface at 1000 Hz. The beam-tracing model gave exactly the same results as the theory. Solid line: wave-based modeling; dash-dot line: energy-based modeling.

$$p = p_d + p_r = p_0 \left(\frac{\exp(ikr_d)}{r_d} + \frac{\exp(ikr_r)}{r_r} \right) \quad (4.1)$$

where r_d and r_r are the distances from the real and image source to the receiver. In energy-based models, on the other hand, squared amplitudes of the direct and reflected waves are added:

$$p^2 = p_d^2 + p_r^2 = p_0^2 \left(\frac{1}{r_d^2} + \frac{1}{r_r^2} \right) \quad (4.2)$$

Assuming unit pressure amplitude, the pressure field is calculated using Eqs. (4.1) and (4.2) for both the energy- and wave-based models in a two-dimensional configuration at 1000 Hz. The results are shown in Figure 4.2. The source is located 1 m above the ground at $x = 1$ m. The receiver is located 1.8 m above the ground and its position varies between $x = 0$ and 5 m. Note that the difference between the energy- and wave-based pressure levels at $x = 1$ m is due to the height difference of the sound and receiver.

The beam-tracing model gave exactly the same results as theory in both cases.

4.2.2 Diffuse Reflection

In the case of specular reflection beam-tracing predictions had very good agreement with theory using as few as 320 beams. For diffuse reflections, on the other hand, predictions did not converge, even with 128,000 beams, and different results were obtained each time the program was run. The reason lies in the statistical nature of the diffuse-reflection algorithm used in the model. Because the directions are chosen using random numbers, a very large number of beam trajectories would be required for the sound field to converge. In ray-tracing models (e.g. PRAY) where this type of diffusion modeling works, a much greater (up to even two orders of magnitude) number of rays is usually used. Since the ray-tracing algorithm is itself statistical, inclusion of diffuse reflections does not impose additional restrictions. Beam-tracing models, however, are deterministic, and inclusion of a statistical module restricts their applicability. A more valid way of modeling diffuse reflections within the beam-tracing model would be to incorporate acoustical radiosity and use a hybrid model, as proposed by Lewers [82].

4.3 Comparison with Measurements in a Reverberant Room

The sound field calculated using the beam-tracing model has been compared with the results obtained from pure-tone measurements in a reverberant room (an empty office). The measurements were carried out by Bibby [7] in order to examine the scattering performance of a corrugated-plywood product on the standing waves in a small room. This is a $5.35 \times 4.00 \times 2.70 \text{ m}^3$ rectangular room, which has a floor of vinyl tile on concrete, four walls of drywall on 100-mm studs and a suspended acoustical ceiling. The source was an omnidirectional dodecahedron speaker, located in one corner of the room (approximately 35 cm away from the two walls). Steady-state sound-pressure levels were measured at 22 locations along the 4-m length, 1.5 m from one wall and 1.35 m above the ground. Reverberation times T_{20} were measured in octave bands at five receiver positions in the room, and averaged.

To validate the model, beam-tracing predictions using the same room geometry were compared with measured results, in two stages. In the first stage, the reverberation time of the room was studied. Measured octave-band reverberation times were used to calculate average diffuse-field absorption coefficients for the room surfaces, and then employed in the beam-tracing model in four configurations. In configuration Z1, the locally-reacting impedance, Z , that corresponded to the diffuse-field absorption coefficients were calculated and used as the boundary condition for all room surfaces – see Table 4.1. In configuration R1, the octave-band diffuse-field absorption coefficients were applied to all room surfaces. To investigate the effects of frequency dependence, the boundary conditions in configuration Z1 and R1 were averaged over frequency and used as frequency-independent boundary conditions in configurations Z2 and R2, respectively. The configurations were chosen such that they would give the same reverberation times in a diffuse-field condition, equal to the measured values. For each configuration, wave- and energy-based beam-tracing predictions were made at five receiver positions, and averaged.

In the second stage of validation, the measured steady-state response of the room was compared with predictions made by the beam-tracing model using the same boundary conditions, and the results are discussed. All beam-tracing predictions in this section were made using 4500 beams and 50 reflections.

4.3.1 Reverberation Time

Under the assumption of a diffuse sound field (described in section 2.2.2), the reverberation time, T , of a room can be expressed as follows [74, Eq. (5.24)]:

$$T = \frac{24 \ln 10}{c} \frac{V}{-S \ln(1 - \bar{\alpha})} \quad (4.3)$$

where V is the volume of the room, m is the air-absorption exponent (introduced in section 3.3), S is the total surface area of the room, and $\bar{\alpha}$ is the average absorption coefficient of the room surfaces. If the sound field in the room is diffuse, the average absorption coefficient of the room surfaces can be calculated using this equation.

The reverberation times of the room, T_{20} , in octave bands from 63 to 4000 Hz were measured at five receiver positions and averaged. The corresponding average diffuse-field absorption coefficients of the room were then calculated and used as the boundary conditions of the room for beam-tracing predictions in four configurations.

Table 4.1 shows the measured and predicted results at octave-band frequencies from 63 to 4000 Hz. For reverberation times, their standard deviations from the measured values are presented in the last column. In the case of wave-based predictions, it can be seen that when frequency-dependent boundary conditions are used, the results have good agreement with

Table 4.1. Summary of measurement and prediction results for the reverberant room.

		63 Hz	125 Hz	250 Hz	500 Hz	1 kHz	2 kHz	4 kHz	Avg.	Dev.
Measurements	T20 (s)	0.56	0.58	0.45	0.66	0.74	0.52	0.90	0.63	0
	$\bar{\alpha}$	0.16	0.16	0.20	0.14	0.13	0.17	0.11	0.15	-
Z (Nsm⁻³)		17529	17529	13512	20411	22188	16345	26725	19452	-
Wave-based T20 (s)	R1	0.57	0.64	0.50	0.63	0.66	0.50	0.71	0.60	0.09
	R2	0.58	0.65	0.72	0.62	0.59	0.54	0.57	0.61	0.19
	Z1	0.48	0.62	0.50	0.63	0.64	0.47	0.68	0.57	0.11
	Z2	0.51	0.65	0.71	0.61	0.58	0.53	0.55	0.59	0.19
Energy-based T20 (s)	R1	0.56	0.58	0.48	0.63	0.67	0.52	0.69	0.59	0.09
	R2	0.59	0.59	0.59	0.59	0.58	0.57	0.55	0.58	0.17
	Z1	0.89	0.54	0.44	0.58	0.63	0.48	0.65	0.60	0.18
	Z2	0.57	0.57	0.57	0.57	0.56	0.55	0.53	0.56	0.18

measurements. The configuration with constant-reflection surfaces (R1) gave results slightly closer to the measurements than the configuration with locally-reacting surfaces (Z1). The two configurations have similar results to each other, except at 63 Hz and, in both cases, using an average frequency-independent absorption coefficient resulted in poorer agreement with measurement, most significantly at 250 and 4000 Hz. In the case of energy-based predictions, the two configurations with frequency-dependent boundary conditions gave reverberation times that agreed well with measurement, except at 4000 Hz. When locally-reacting boundaries were used (Z1), the predicted reverberation time at 63 Hz had the biggest deviation from the measured value. For configurations with frequency-independent boundary conditions, as expected, reverberation times did not change with frequency, except very slightly due to air absorption.

In general, energy-based reverberation times were predicted to be lower than wave-based ones. Among all configurations, R1 gave the best match with measurements in both energy- and wave-based predictions, followed by wave-based predictions in Z1. All configurations predicted unexpectedly lower reverberation times than measurements at 4000 Hz, which could not be explained.

4.3.2 Steady-State Sound-Pressure Level

Energy- and wave-based predictions of the steady-state sound-pressure levels were compared with measurements at four frequencies: 86, 172, 258 and 430 Hz. The results are shown in Figures 4.3 to 4.6. Frequency-invariant and frequency-varying boundary conditions gave very similar results and have not been presented here.

In general, it can be seen that some aspects of the modal behaviour of the sound field can be predicted using wave-based beam-tracing; predictions, however, do not agree well with measurements. Constant-reflection boundary conditions gave results closer to experiments than

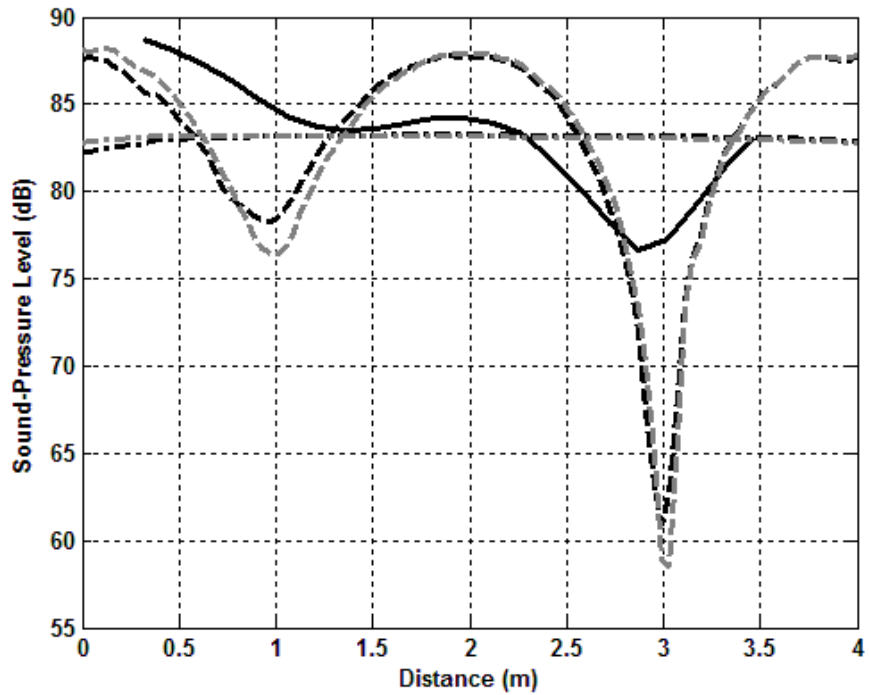


Figure 4.3. Comparison of pure-tone measured and predicted steady-state sound-pressure levels in a reverberant room at 86 Hz. Solid line: measurement; black dashed lines: wave-based prediction for R1; black dash-dot lines: energy-based prediction for R1; grey dashed lines: wave-based prediction for Z1; grey dash-dot lines: energy-based prediction for Z1.

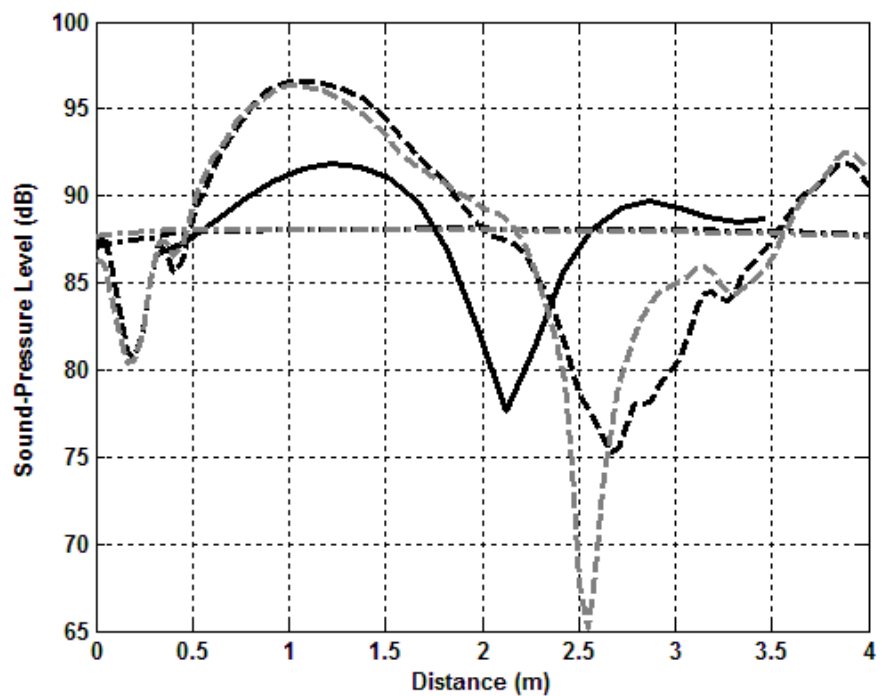


Figure 4.4. Comparison of pure-tone measured and predicted steady-state sound-pressure levels in a reverberant room at 172 Hz. Solid line: measurement; black dashed lines: wave-based prediction for R1; black dash-dot lines: energy-based prediction for R1; grey dashed lines: wave-based prediction for Z1; grey dash-dot lines: energy-based prediction for Z1.

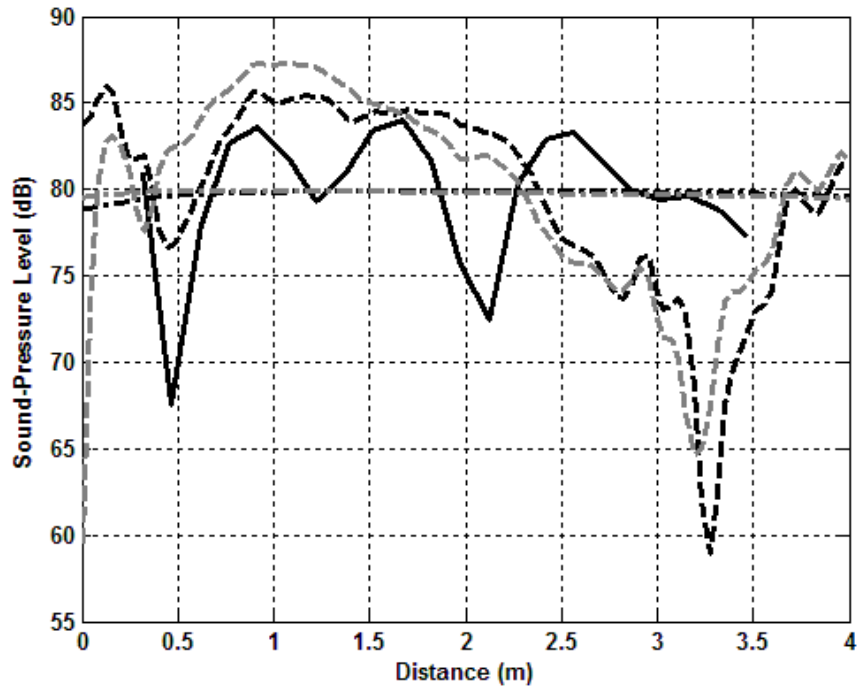


Figure 4.5. Comparison of pure-tone measured and predicted steady-state sound-pressure levels in a reverberant room at 258 Hz. Solid line: measurement; black dashed lines: wave-based prediction for R1; black dash-dot lines: energy-based prediction for R1; grey dashed lines: wave-based prediction for Z1; grey dash-dot lines: energy-based prediction for Z1.

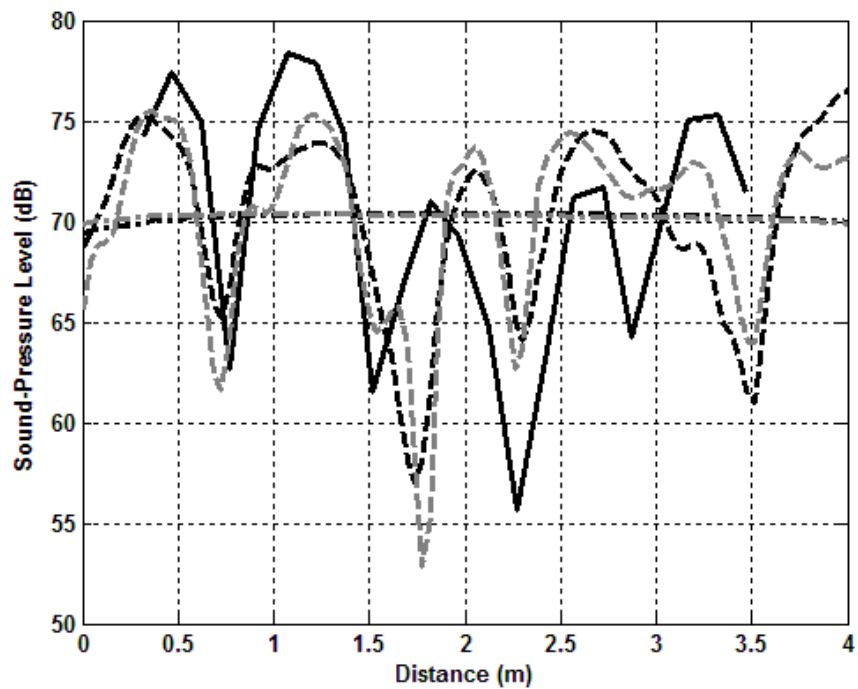


Figure 4.6. Comparison of pure-tone measured and predicted steady-state sound-pressure levels in a reverberant room at 430 Hz. Solid line: measurement; black dashed lines: wave-based prediction for R1; black dash-dot lines: energy-based prediction for R1; grey dashed lines: wave-based prediction for Z1; grey dash-dot lines: energy-based prediction for Z1.

locally-reacting boundary conditions. Predictions are specifically inaccurate in determining the locations and amplitudes of the peaks and troughs, but their modal pattern is somehow similar to that of the measurements. This might be due to inaccuracies in measuring the location of the source and receivers, and to phase changes on reflections. Energy-based predictions do not show any modal behaviour, as expected.

4.5 Diffraction

The diffraction model developed by Svensson *et al.* [122] is considered in this section for implementation in the new beam-tracing model; we refer to this model as Svensson's model. Coding of the theory is validated through comparison with results in the literature. Sound diffraction over a finite wedge is then predicted using Svensson's model and the uniform theory of diffraction (UTD) [69], and the results are compared. Predictions are then compared with measurements on a finite-length barrier over a flat surface in an anechoic chamber. Implementation of diffraction into the new beam-tracing model is then discussed.

4.5.1 Validation of the Code

To ensure that Svensson's model was programmed correctly, results obtained from the program were compared with results in the literature. For this purpose, the configuration used by Calamia [18], shown in Figure 4.7, was chosen. Calculations were performed for two receiver positions: R_1 in the shadow region and R_2 on the shadow boundary, using Eq. (3.44). The source is positioned at $(r_S, \theta_S, z_S) = (2 \text{ m}, 45^\circ, 0)$, receiver R_1 at $(r_R, \theta_R, z_R) = (5 \text{ m}, 270^\circ, 0)$ and receiver R_2 at $(r_R, \theta_R, z_R) = (5 \text{ m}, 224.999^\circ, 0)$. Four edge lengths (1, 2, 4 and 16 m) for R_1 and one edge length (1 m) for R_2 were used. The results obtained from the program are shown in Figure 4.8. Through visual comparison, they seem to be identical to the results reported by Calamia

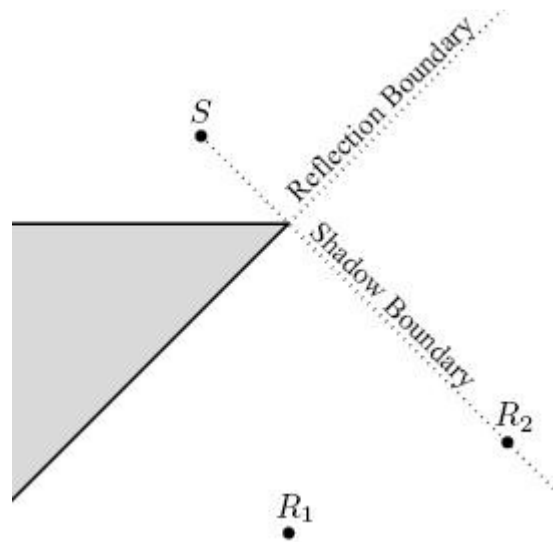


Figure 4.7. The configuration used for predicting the results in Figure 4.8 [18].

[18, pp. 36-37]; his Figure 3.7 is reproduced here as Figure 4.9.

4.5.2 Comparison with the Uniform Theory of Diffraction

It was stated in section 2.4 that the uniform theory of diffraction (UTD) describes a high-frequency approximation of the diffracted sound over an infinite wedge, while Svensson's model provides an exact formulation which applies to all frequencies and wedge lengths. Consequently, it is expected that the two models give the same result for long (compared to sound wavelength) wedges at high frequencies. To validate this, the diffracted sound at receiver R_1 was predicted using UTD (Eq. 3.54) and compared with results obtained using Svensson's model (Eq. 3.44) – see Figure 4.10.

It can be seen in Figure 4.10 that, as frequency increases, the difference between the diffraction coefficients predicted by the two models decreases. Moreover, as the length of the wedge is increased, diffraction coefficients predicted by UTD become closer to those predicted by Svensson's model; this is especially clear at lower frequencies. It should be noted, however,

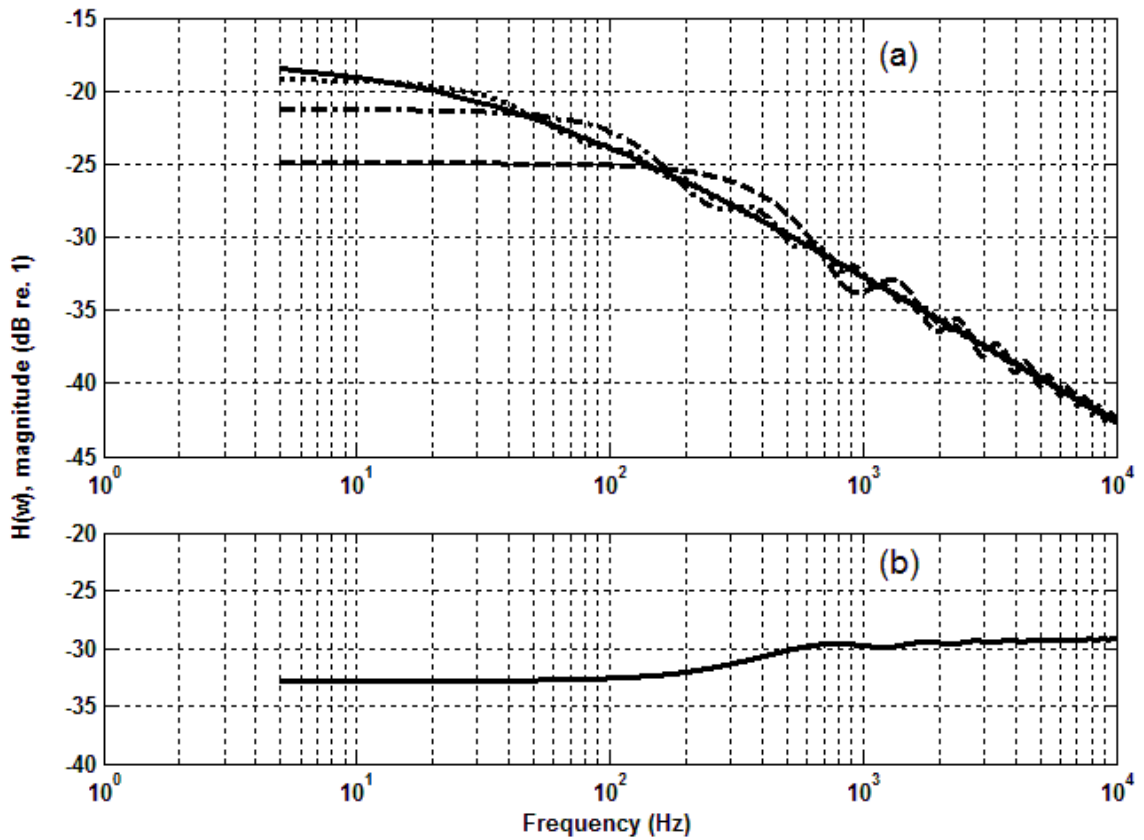


Figure 4.8. Magnitude of the diffraction coefficient calculated using Svensson's model for the configuration in Figure 4.7. (a) Receiver R_1 . Solid line: edge length = 16 m; dotted line: edge length = 4 m; dash-dot line: edge length = 2 m; dashed line: edge length = 1 m. (b) Receiver R_2 , edge length = 1 m. Note that the magnitude of diffraction coefficients is presented as $20\log(H_{diff}(\omega))$.

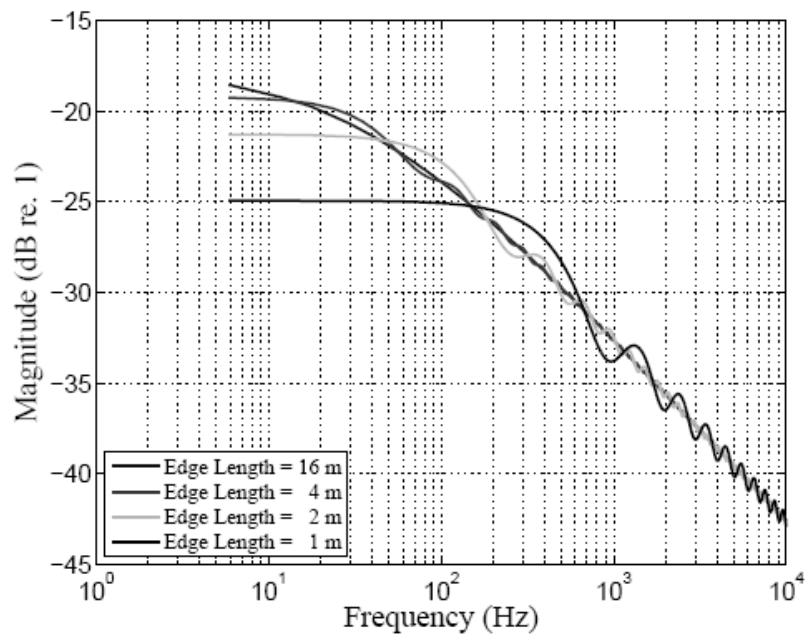


Figure 4.9. Reference solution for the configuration corresponding to Receiver R1 [18].

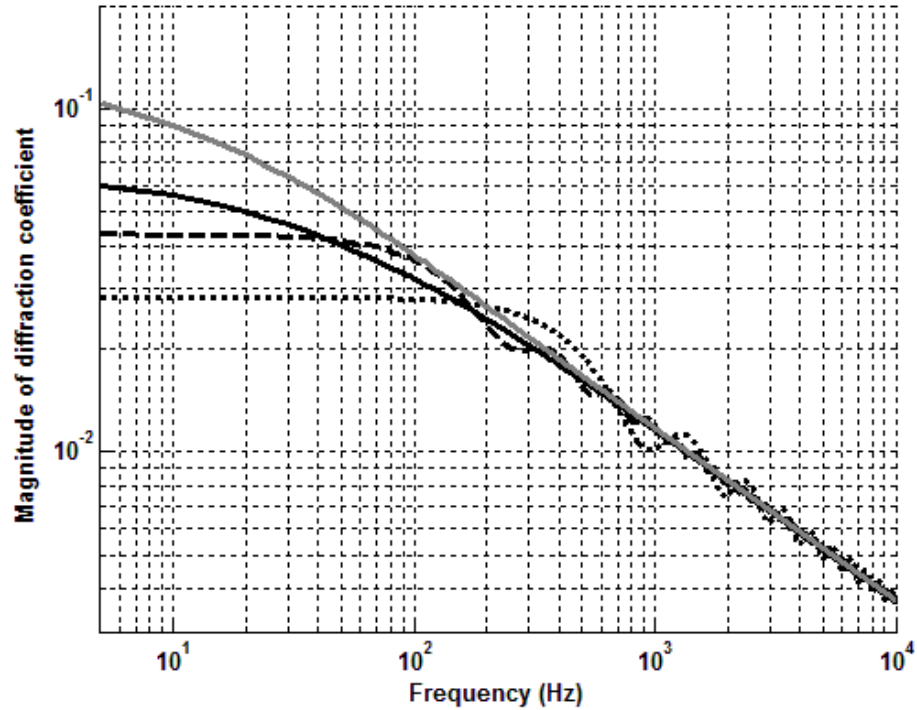


Figure 4.10. Magnitude of the predicted diffraction coefficients at receiver R_1 in Figure 4.8. Grey line: UTD; black lines: Svensson's model with different wedge lengths (solid line: 16 m, dashed line: 2 m, dotted line: 1 m).

that when the edge becomes shorter, diffraction from its sides becomes more important, and the difference between the two models is expected to increase. Another observation made from Figure 4.10 is that the magnitude of the diffraction coefficient is very small; less than 1% of the incident sound energy reaches receiver R_1 in the configuration considered here.

Insertion-loss measurements on a finite-length barrier (of double-drywall construction – length = 3.6 m, thickness = 15 cm) over a flat, hard surface (painted 19-mm plywood panels) in an anechoic chamber were performed by Daltrop [24]. Measurements were performed for two source positions and ten receiver positions, as shown in Figure 4.11. Predictions were made only for the lower source position, S1, and the first eight receiver positions, R1 to R8, with the flat surface assumed to be rigid. In the absence of the barrier, predictions were made using Eq. (4.1). The diffracted sound field was predicted using both Svensson's model and UTD. Only

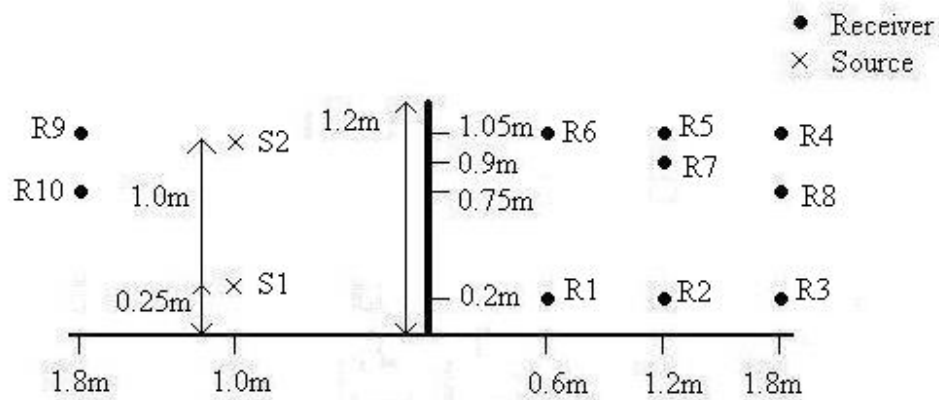


Figure 4.11. Source and receiver configuration for barrier insertion-loss measurements [24].

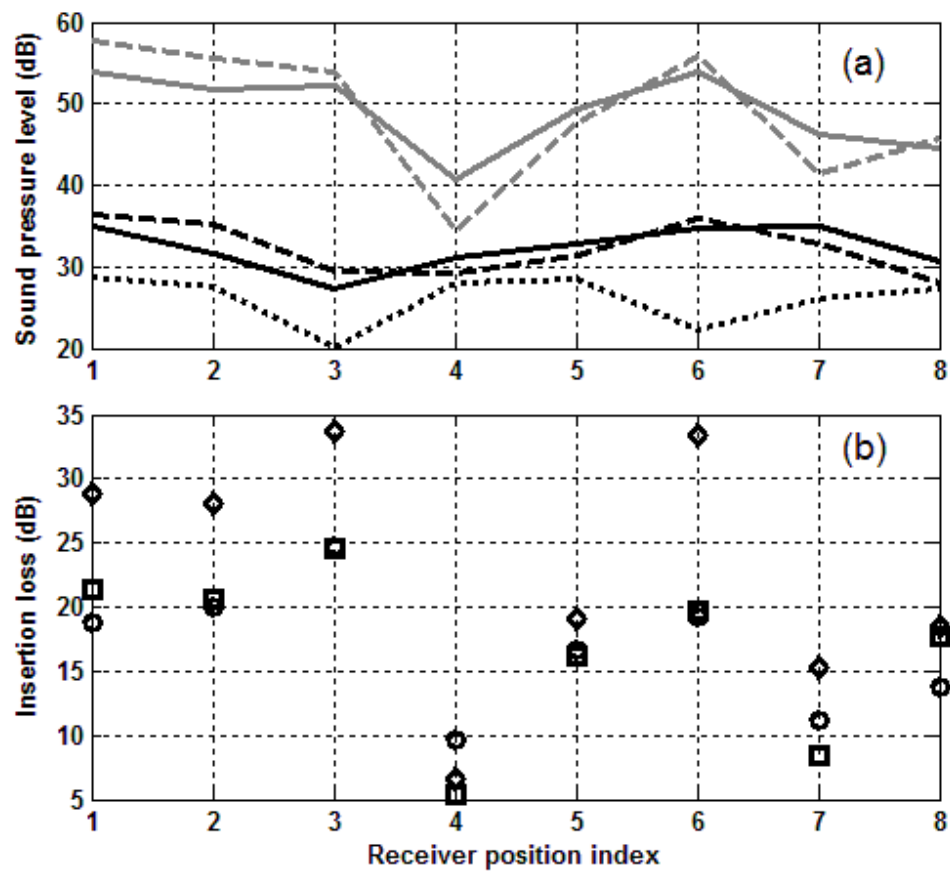


Figure 4.12. Third-octave-band measured and predicted sound-pressure levels and insertion losses of the barrier configuration at 1000 Hz. (a) Sound-pressure levels. Grey lines: without the barrier (solid line: measurement, dashed line: prediction); black lines: with the barrier (solid lines: measurement, dashed line: prediction using Svensson's model, dotted line: prediction using UTD). (b) Insertion loss. Circles: measurement; squares: Svensson's model; diamonds: UTD.

diffraction over the top edge of the barrier was included in the predictions; diffraction from the two sides of the barrier, as well as from the edges of the floor plate, was ignored.

Figure 4.12 shows the measured and predicted sound-pressure levels with and without the barrier, along with the associated insertion losses, for the 1000 Hz third-octave band. It can be seen that measurement and prediction show similar trends for the sound-pressure level when Svensson's model is used. In comparison, UTD underestimates the diffracted sound-pressure levels. The standard deviation between predictions using Svensson's model and the measured insertion losses is 3.4 dB. This discrepancy can be associated with a number of factors, such as second-order edge diffraction due to the finite width of the barrier, diffraction from the edges of the floor, and inconsistency in receiver positions in the two measurement configurations. Overall, the results shown in Figure 4.12 are indicative of the better accuracy of Svensson's model relative to UTD in predicting the insertion loss of a finite-length barrier.

4.5.3 Implementation in the Beam-Tracing Model

A preliminary diffraction algorithm was implemented in the new beam-tracing model. It accounts for sound diffraction over thin, vertical barriers which are located parallel to the xz coordinate plane of a room. The barrier is defined using two surfaces with their normal vectors defined in opposite directions. If all the vertices of a beam hit the same surface, the beam is not diffracted; it is reflected specularly from the surface. A beam's trajectory is diffracted if it overlaps the edge of the barrier. This happens if one, but not all, of the vertices of the beam hit the barrier surfaces; the case in which the beam hits the surfaces of the barrier and the floor is excluded by a subsequent check. A new beam is then emitted from the edge of the barrier in a random direction in the shadow zone of the real sound source. Either Svensson's model or UTD can be used to calculate diffraction coefficients.

The insertion loss of a barrier inside a reverberant room was predicted with the new beam-tracing model and compared with experimental results reported by Lau and Tang [78]. They measured the insertion loss of a thin barrier with hard surfaces in a reverberant room, shown in Figure 4.13. An omnidirectional source was positioned at $(x, y, z) = (1.500, 2.415, 0.150)$ in m. Beam-tracing predictions were compared with measurements along one row of receivers, positioned at $(x = 2.5, 3.0, 3.5, 4.0, 4.5, 5.0; y = 1.125, z = 0.45)$ in m. All surfaces were given a diffuse-field absorption coefficient of 0.092. Results are shown in Figure 4.14. Experimental results were extracted from Figure 2c in [78]. Beam-tracing predictions were averaged over five runs, each using 12500 beams and 100 reflections.

Due to the randomization used in diffracting the beams, poor accuracy is obtained with the beam-tracing model, and no trend can be observed in the results. A more meaningful direction for a diffracted beam could potentially be chosen as the direction in which the energy of the diffracted sound is greatest. For a given distance from the diffracting edge, this would be the direction in which the diffraction coefficient is smallest in magnitude. Further research is needed to find a deterministic way of implementing diffraction into beam-tracing.

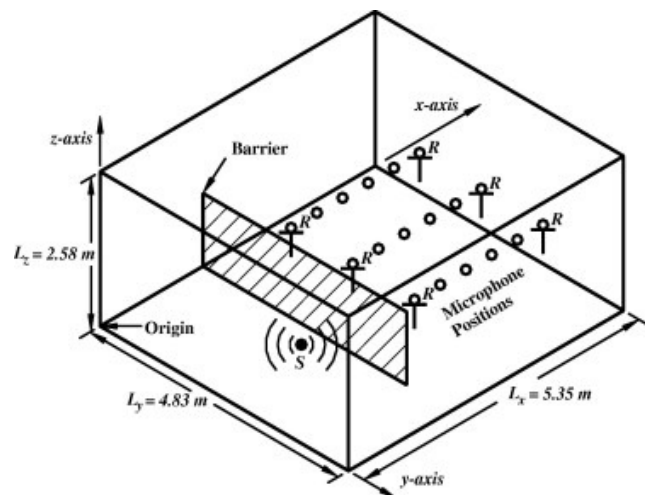


Figure 4.13. Layout of the configuration used by Lau and Tang [78] for insertion-loss measurements. Beam-tracing predictions were compared with the experimental results along the middle row of receivers.

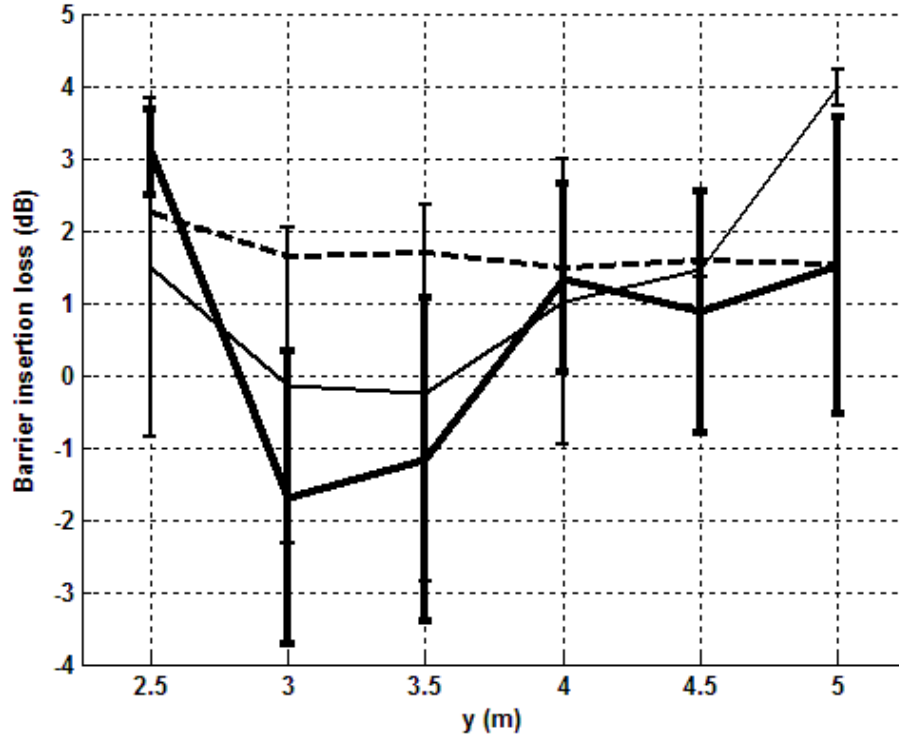


Figure 4.14. Insertion loss of the barrier in the configuration shown in Figure 4.14 in the 1000-Hz octave band. Dashed line: measurement; solid lines: beam-tracing predictions (thick line: using UTD; thin line: using Svensson's model).

Accounting for diffraction significantly decreased the computational efficiency of the model. This is due to the additional subroutines that were added to the program. For each beam trajectory, a decision must be made on whether the beam is to be diffracted; moreover, a visibility check is necessary to ensure that beams that are blocked by the barrier are not detected. For beams that are diffracted, a new source position and direction of propagation are calculated, as well as a diffraction coefficient. For a given number of beam trajectories, these introduce about a 50% increase in runtime.

4.6 Summary

In this chapter, modifications made to the existing beam-tracing model were validated. The computational efficiency of the model was improved; however, we saw later that accounting for diffraction significantly increased the runtimes due to additional calculations. The accuracies

of wave- and energy-based predictions were investigated for the case of sound propagation over a flat surface. While beam-tracing predictions matched very well with theory in the case of a specularly-reflecting surface, they did not converge in the case of a diffusely-reflecting surface. This was due to incompatibility of the diffuse-reflection model used here, which was imported from PRAY, with the beam-tracing model. As a result, all subsequent predictions were restricted to specular reflections only.

The beam-tracing model was also used to predict measurement results in a reverberant room. Although predicted reverberation times were close to measured values, predicted sound-pressure levels did not agree well with measurements, except in their general trends. This points out the importance of considering several parameters in validating a prediction model, as one parameter might be predicted accurately, while another is not.

The correct programming of Svensson's diffraction model was validated. The diffracted sound over the edge of a finite-length wedge was then predicted using both Svensson's model and the uniform theory of diffraction. It was shown that, as expected, as frequency and the length of the barrier increase, the difference between predictions by the two models decreases. The insertion loss of a finite barrier on a rigid surface was then predicted using the two models and compared with experimental results. The results suggest that Svensson's model predicts the diffracted sound with better accuracy than UTD. A preliminary diffraction model was then implemented into the beam-tracing model, tested and the results discussed.

In the following chapter, the beam-tracing model is used to investigate the effects of different surface-reaction models on the transient response and derived room-acoustical parameters in three different room configurations.

Chapter 5

Application of the New Model

The new beam-tracing model was next applied to three room configurations in order to compare the effects of different surface-reaction models on the transient response and derived room-acoustical parameters of the room. One or more of the room surfaces were assigned a multilayer structure, and were modeled as of extended and local reaction. The aim was to extend the work of Hodgson and Wareing [52], in which the predicted steady-state levels in rooms with extended- and local-reaction surfaces were compared. In addition to extending their comparisons from steady-state pressure levels to other room-acoustical parameters of the rooms, the effects of phase changes due to surface reflections have been considered by comparing real and complex reflection coefficients. Moreover, wave- and energy-based modeling have been compared in all cases.

This chapter begins with an introduction to the three test rooms and the boundary conditions (test surfaces) used in each room, followed by a brief review of the previous investigations by Hodgson and Wareing. We then consider the differences between the configurations, by studying the absorption coefficients of the test surfaces, focusing on differences between local- and extended-reaction modeling. Energy- and wave-based models are next compared, using energy impulse responses and sound-decay curves in the three room configurations. Prediction results are then presented for all twelve test configurations and discussed.

5.1 Test Configurations

Three room configurations representing a small, empty office (Room 1), a corridor (Room 2) and a small, empty industrial workshop (Room 3) were studied by Hodgson and Wareing [52]. They used various multilayer boundary conditions for the surfaces of these rooms, based on which twelve room configurations were considered. Details of the room geometries and multilayer boundary conditions are given in Table 5.1. The acoustical properties of the surfaces with multilayer structures were (pre)calculated using the transfer-matrix algorithm. All other surfaces of the rooms were assigned an average diffuse-field absorption coefficient of 0.1, invariant with the incident angle and frequency. Room surfaces were assumed to be specularly-reflecting.

The basic room configurations involved only the angularly-invariant, average diffuse-field absorption coefficient of 0.1 (configurations R1, R2 and R3). A large window was modeled on one wall in each of the rooms, with either a single glass panel (G1, G2, and G3) or a double glass panel with a 100-mm air cavity (DG1, DG2, and DG3). Carpet on a hard backing was used as the floor surface in Rooms 1 and 2 (C1 and C2). The four walls of Rooms 1 and 2 were

Table 5.1. Rooms, surface configurations and source and receiver positions involved in the predictions.

Room No.	Test Surface	Location of test surface (m)	Dimensions $L_x \times L_y \times L_z$ m ³	Source position (x_S, y_S, z_S) (m)	Receiver position (x_R, y_R, z_R) (m)
1	Single-glass panel	$y = 0$	3×3×3	(0.5, 1.5, 2.0)	(2.5, 1.5, 1.8)
	Double-glass panel	$y = 0$			
	Double-drywall panel	$x = 0, x = 3,$ $y = 0, y = 3$			
	Carpeted floor	$z = 0$			
	Suspended ceiling	$z = 3$			
2	Single-glass panel	$y = 0$	10×3×3	(0.5, 1.5, 2.0)	(9.5, 1.5, 1.8)
	Double-glass panel	$y = 0$			
	Double-drywall panel	$x = 0, x = 3,$ $y = 0, y = 3$			
	Carpeted floor	$z = 0$			
	Suspended ceiling	$z = 3$			
3	Single-glass panel	$y = 0$	10×10×3	(0.5, 5.0, 1.5)	(9.5, 5.0, 1.8)
	Double-glass panel	$y = 0$			
	Double-steel panel	$x = 0, x = 3,$ $y = 0, y = 3$			
	Double-steel panel	$z = 3$			
	Fibreglass on hard backing	$z = 3$			

modeled with double-drywall panels with a 100-mm air cavity (D1 and D2). A suspended acoustical ceiling was modeled with a 12-mm layer of fibreglass, 457-mm layer of air and a rigid

backing, and applied to the ceiling of Rooms 1 and 2 (SAC1 and SAC2). The ceiling in Room 3 was modeled in two ways: using a double-steel panel as used for the walls (SC3), and using a 100-mm fibreglass layer with a rigid backing (FG3). The four walls of Room 3 were modeled with double-steel panels with a 100-mm air cavity (SW3).

All configurations were the same as the ones used by Hodgson and Wareing, except that the R- and DG-configurations were added. The R-configurations were used to compare energy- and wave-based models. DG-configurations were introduced as complementary to G-configurations; however, as will be discussed in section 5.3, they were not considered in the final set of configurations. Consequently, studies of room-acoustical parameters were only performed for the original twelve configurations.

All predictions were performed using the same parameter values as Hodgson and Wareing: constant source-power level of 80 dB at all frequencies; source positioned at the center of the wall at $x = 0$, 0.5 m in front of it and at a constant height of 2 m; receiver positioned at the center of the wall at $x = L_x$, 0.5 m in front of it and at a constant height of 1.8 m. Predictions were made using 4500 beams, which were traced for 80 reflections. A frequency range of 0.5 to 5600 Hz was used to obtain results up to the octave band centered at 4000 Hz, using 0.5-Hz increments. Calculation times were typically 35 to 40 minutes on a PC with a 2.40 GHz CPU and 1.97 GB of RAM, for all configurations.

5.2 Review of Previous Investigations

Hodgson and Wareing [52] studied the difference in predicting steady-state sound-pressure levels in rooms with surfaces modeled as of local or extended reaction. They examined the differences between the local- and extended-reaction sound-pressure levels in octave bands from 63 to 2000 Hz for the twelve test configurations described in section 5.1. They explained their results by comparing the reflection coefficients of the test surfaces, and accounting for the

incident angles associated with first-order reflections; after the direct sound, the greatest contribution to the steady-state sound pressure at a receiver is expected to be from the first-order reflections. Following are their concluding remarks on the significance of modeling room surfaces as of extended or local reaction on the steady-state sound field in a room, quoted from [52]:

1. *The difference between modeling a room surface as of extended or local reaction is not significant when the surface is a single plate, or a single layer of material with a rigid backing. In the case of a porous layer on a rigid backing, the results likely depend on the flow resistivity of the porous layer;*
2. *The difference between modeling a room surface as extended or local reaction is significant when the surface consists of multi layers of solid or porous material, and includes a layer of air with a thickness that is large relative to the other layers. The local-reaction approximation can result in octave-band levels being either under- or over-estimated, by over 10 dB in some cases;*
3. *For surfaces for which the reflection coefficient is different when obtained using extended- and local-reaction surface impedances, the difference between the extended- and local-reaction levels may be significant, depending on the source and receiver positions. This becomes important when the positions are such that the first-reflection angle of incidence on the room surface is near grazing.*

The objective of this chapter is to revisit the configurations used by Wareing and Hodgson, and study them in terms of their transient response and room-acoustical parameters. We begin, in the next section, by taking a closer look at the boundary conditions in the room, in order to understand the differences between the configurations better.

5.3 General Properties of the Boundary Conditions

In this section, the general properties of the boundary conditions used in the test configurations are studied. The aim is to gain a general understanding of the differences between the test configurations, specifically of the differences between the local- and extended-reaction assumptions. The analysis is limited to considering the absorption coefficients of the surfaces. More detailed analysis of the boundary conditions will be performed when absorption coefficients do not provide sufficient information in analyzing the results.

In addition to an average diffuse-field absorption coefficient of 0.1 used in every test configuration, seven other boundary conditions were used. For ease of reference, the seven test surfaces are abbreviated as follows: SGP for single-glass panel, used in configurations G1, G2 and G3; DGP for double-glass panel, used in DG1, DG2, and DG3; DDW for double-drywall panel, used in D1 and D2; DSP for double-steel panel, used in SW3 and SC3; CAF for carpeted floor, used in C1 and C2; FR for fibreglass on a rigid backing, used in FG3; FA for fibreglass on an air cavity, used in SAC1 and SAC2.

We begin by considering the average diffuse-field absorption coefficients of the seven test surfaces in octave bands. These are shown in Table 5.2. As expected, it can be seen that surfaces that have a porous layer have different absorption characteristics than the other ones. When there is no porous layer in the structure of the surface (SGP, DGP, DDW, DSP), the absorption coefficients are very low, and generally decrease with frequency. Surfaces containing a porous layer (CAF, FR, FA), on the other hand, have high absorption, and become more absorptive as frequency increases.

For a single-glass panel (SGP), the extended-reaction absorption is slightly higher than the local-reaction absorption, especially at the lowest frequencies. In the 2-kHz band, the

increase in the extended-reaction absorption corresponds to the coincidence phenomenon⁴, which is only predictable with the extended reaction model. When a second layer of glass is added (DGP), the absorption coefficients decrease slightly, except at the lowest frequencies. The increase in low-frequency absorption coefficients corresponds to the mass-air-mass resonance of the wall. Because mass-air-mass resonance occurs for both normal and oblique incidences [32, p.316], the local-reaction model predicts it as well, but with different characteristics than the extended-reaction model – see Figure 5.1. The same differences between the local- and extended-reaction absorption coefficients are observed in the other double-partition walls, DDW and DSP. The diffuse-field absorption characteristics of DGP and DDW are very similar. DSP, on the other hand, is generally more absorptive and its coincidence and mass-air-mass resonance frequencies are higher than those of DDW. This can be seen in Figure 5.1, where the diffuse-

Table 5.2. Octave-band diffuse-field absorption coefficients of the test surfaces.

Boundary condition	Surface-reaction model	Frequency (Hz)							Average
		63	125	250	500	1000	2000	4000	
SGP	Extended	0.17	0.09	0.05	0.02	0.01	0.02	0.01	0.05
	Local	0.12	0.06	0.03	0.02	0.01	0.00	0.00	0.04
DGP	Extended	0.20	0.11	0.03	0.01	0.00	0.01	0.00	0.05
	Local	0.27	0.02	0.00	0.00	0.00	0.00	0.00	0.04
DDW	Extended	0.20	0.12	0.03	0.01	0.00	0.01	0.00	0.05
	Local	0.28	0.02	0.00	0.00	0.00	0.00	0.00	0.04
DSP	Extended	0.32	0.33	0.18	0.05	0.01	0.01	0.02	0.13
	Local	0.30	0.39	0.03	0.00	0.00	0.00	0.00	0.10
CAF	Extended	0.05	0.10	0.18	0.26	0.35	0.44	0.52	0.27
	Local	0.04	0.08	0.13	0.18	0.23	0.27	0.33	0.18
FR	Extended	0.42	0.57	0.65	0.72	0.79	0.85	0.89	0.70
	Local	0.41	0.57	0.65	0.71	0.77	0.84	0.86	0.69
FA	Extended	0.41	0.69	0.76	0.63	0.68	0.74	0.79	0.67
	Local	0.65	0.85	0.69	0.70	0.71	0.73	0.76	0.73

⁴ The coincidence phenomenon happens when the incident acoustical wave coincides with the flexural waves in the wall [32], resulting in a local maximum in the sound-transmission characteristics of the wall.

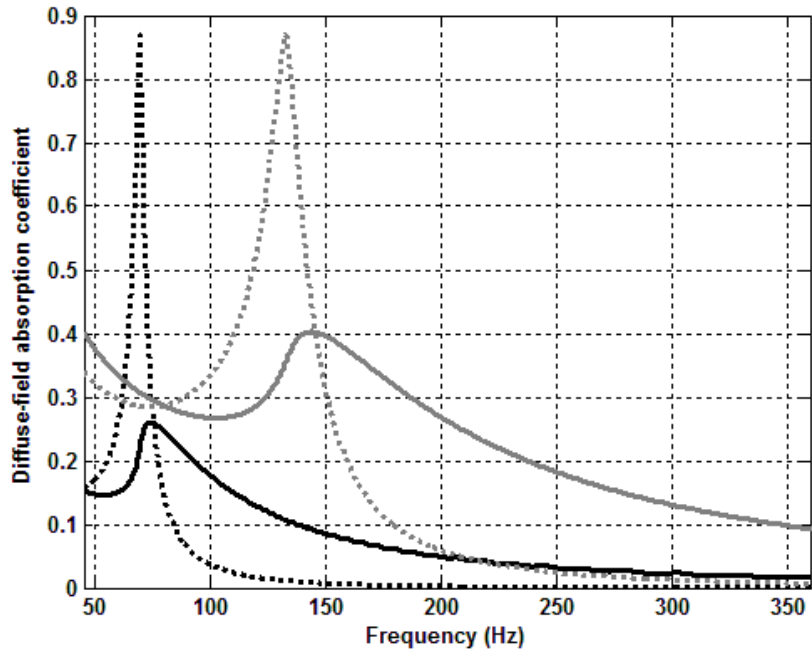


Figure 5.1. Diffuse-field absorption coefficient of the double-drywall panel (black curves) and the double-steel panel (grey curves). Solid lines: assuming extended reaction; dotted lines: assuming local reaction.

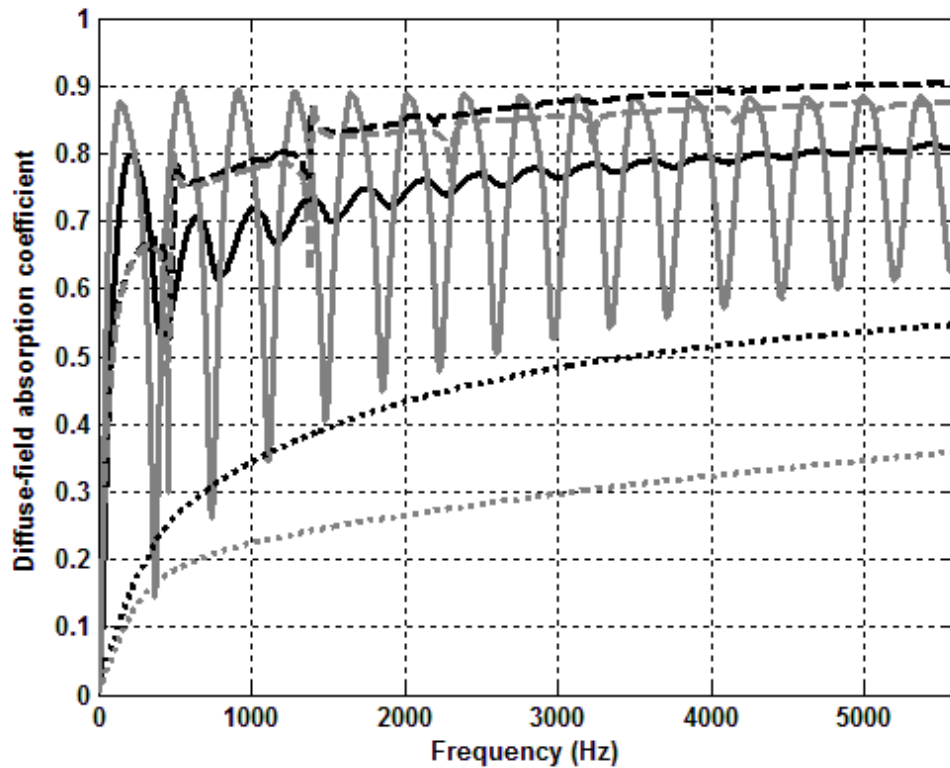


Figure 5.2. Diffuse-field absorption coefficient of the test surfaces with porous layers, assuming extended reaction (black curves) and local reaction (grey curves). Solid lines: FA; dashed lines: FR; dotted lines: CAF.

field absorption coefficients of DGP and DSP are shown for both the local- and extended-reaction models.

The diffuse-field absorption coefficients of the test surfaces with porous layers are shown in Figure 5.2. In the case of the carpeted floor (CAF), and fibreglass on a rigid backing (FR), the local-reaction model predicts lower absorption coefficients than the extended-reaction model. The absorption coefficients increase smoothly with frequency, and so does the difference between local- and extended-reaction modeling. While this difference is significant in the case of CAF, it is very small for FR.

The most significant difference between the local- and extended-reaction modeling of the test surfaces occurs in the case of fibreglass on an air-cavity. In the case of local reaction, the diffuse-field absorption coefficient shows somewhat periodic variations with frequency. Its values fluctuate between a relatively constant maximum and an increasing minimum. In the case of extended reaction, these fluctuations are much smaller, and the absorption coefficient generally increases with frequency. When averaged in octave bands, however, the difference between the two absorption coefficients becomes less significant (Table 5.2).

Figure 5.3 shows the octave-band diffuse-field absorption coefficients at 125 Hz as a function of the angle of incidence for the four test configurations that do not have porous layers; similar trends are observed at other frequencies. It can be seen that the diffuse-field absorption coefficients predicted by the extended- and local-reaction models have different behaviours with respect to angle of incidence. In the case of extended reaction, the absorption coefficients generally increase with angle of incidence, and experience a high peak very close to grazing incidence, followed by a very steep decrease to zero at grazing incidence. Local-reaction absorption coefficients increase slowly and monotonically with angle of incidence until close to

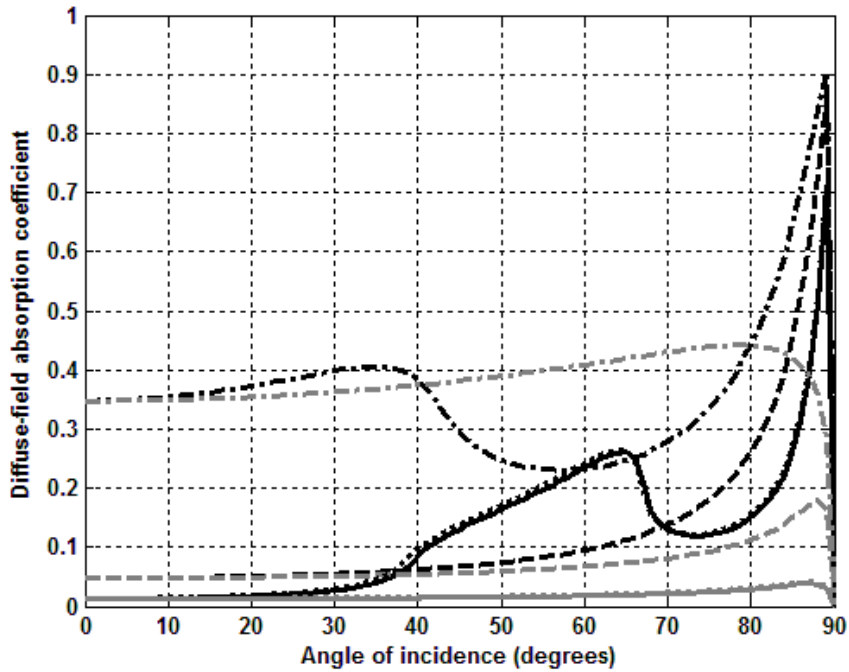


Figure 5.3. Octave-band absorption coefficients of test surfaces at 125 Hz. Black curves: extended reaction; grey curves: local reaction. Solid lines: DGP; dotted line: DDW; dashed lines: SGP; dash-dot line: DSP.

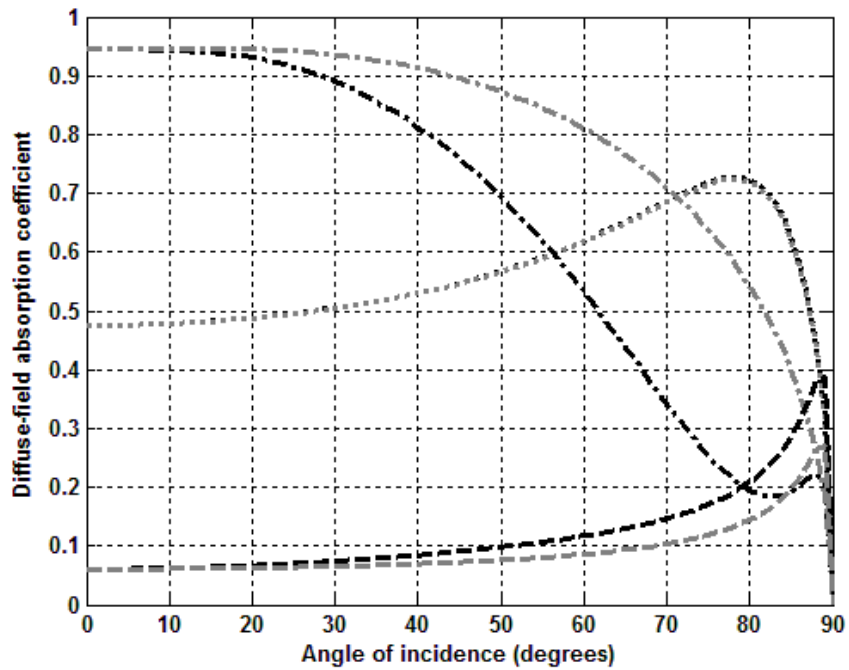


Figure 5.4. Octave-band absorption coefficients of test surfaces at 125 Hz. Black curves: extended reaction; grey curves: local reaction. Dotted line: FR; dashed lines: CAF; dash-dot line: FA.

grazing, where they rapidly decrease to zero. In both cases, the absorption coefficients start from the same value at normal incidence, and reach zero at grazing incidence. It can be seen that DGP and DDW have almost identical behaviours. Locally-reacting DGP does not vary significantly with angle of incidence, and has a smaller absorption coefficient than SGP. The extended-reaction absorption coefficient of DGP, however, increases with angle of incidence and has a similar behaviour to SGP.

The DGP boundary conditions, and therefore the DG-configurations, are omitted from the analysis in this chapter, based on the fact that their absorption characteristics are almost the same as for the DDW surfaces. The only difference between the DG- and DDW-configurations is in the positioning of the test surface, which is already considered in configurations SC3 and SW3.

The 125-Hz octave-band absorption coefficients of the test configurations containing a porous layer are shown in Figure 5.4; similar trends are observed at other frequencies. In the cases of fibreglass on a rigid backing (FR), and the carpeted floor (CAF), similar trends are observed: the diffuse-field absorption coefficients increase monotonically with angle of incidence until they reach a maximum value near grazing incidence, after which they decrease to zero. The predicted absorption coefficients of FR are almost identical for both the local- and extended-reaction models. The difference between local- and extended-reaction modeling of surfaces is most significant in the case of fibreglass on an air cavity (FA). Unlike other test surfaces, the absorption coefficients of FA decrease with angle of incidence. The extended-reaction absorption coefficient decreases more rapidly and has a local maximum close to grazing incidence.

Based on the absorption characteristics of the surfaces, predictions can be made of the results expected to be obtained from the beam-tracing model:

- The most significant difference between local- and extended-reaction modeling of room surfaces is expected to occur for configurations SAC1 and SAC2, which include FA as a room surface. This is based on the fact that, of all of the test surfaces, FA shows the most significant difference between its local- and extended-reaction absorption characteristics;
- Changing between local- and extended-reaction modeling is expected to be significant in configurations C1 and C2, where CAF is used as a test surface, especially as frequency increases;
- No significant change in any of the parameters is expected to be observed in configuration FG3, which has FR as its test surface; the absorption characteristics of FR were almost unchanged when changing between local- and extended-reaction modeling;
- In the case of configurations with test surfaces that do not have porous layers, changes are expected to occur at low frequencies. This is based on the significant difference between local- and extended-reaction models in predicting the diffuse-field absorption coefficients of these surfaces near the mass-air-mass frequency. Moreover, the absorption coefficients of these surfaces have different angular dependencies when modeled as of local and extended reaction; this might cause additional significant differences between the results obtained for the two surface-reaction models.

5.4 Energy Impulse Responses and Decay Curves

The energy impulse response of a room is its most important characteristic when studying the acoustical parameters of the room. The reason for this is that all of the room-acoustical parameters are derived – directly in most cases – from its energy impulse response. Moreover, both energy- and wave-based models are capable of predicting the energy impulse response of a room. Consequently, knowledge of the characteristics of the energy impulse responses of rooms is helpful for studying the room-acoustical parameters.

The calculation of energy impulse responses was described in Chapter 3. In this section, energy impulse responses in the three basic room configurations (R1, R2 and R3) are examined. Decay curves are then compared for these room configurations, and the differences between energy- and wave-based modeling are explained in this context. Unless otherwise specified, energy impulse responses are simply referred to as impulse responses in this section.

The energy- and wave-based impulse responses of the three rooms are shown in Figures 5.5 to 5.7. Note that since all boundary conditions are frequency-invariant, no frequency-dependent phenomena are detected by the energy-based model, and the resulting impulse response is the same at all frequencies. In the case of wave-based impulse responses, as the octave-band frequency increases, the resolution in time increases as well; as a result, higher-frequency impulse responses have finer structures.

Sound-decay curves for the three rooms are shown in Figures 5.8 to 5.10. It can be seen that, while energy-based decay curves are nearly linear, wave-based decay curves are generally nonlinear, especially at lower frequencies. The nonlinearities in the wave-based decay curves correspond to individual peaks in their corresponding impulse responses.

5.5 Prediction Results

The results of the beam-tracing predictions of the twelve test configurations are presented in this section. In each case, test surfaces were modeled as of extended and of local reaction, and the results are compared. Moreover, energy-based and wave-based models are compared, and the effects of phase changes on reflection considered. Three types of predictions were made for each configuration: wave-based with complex reflection coefficients (WBC); wave-based with real reflection coefficients (WBR); energy-based with (inevitably) real reflection coefficients (EBR).

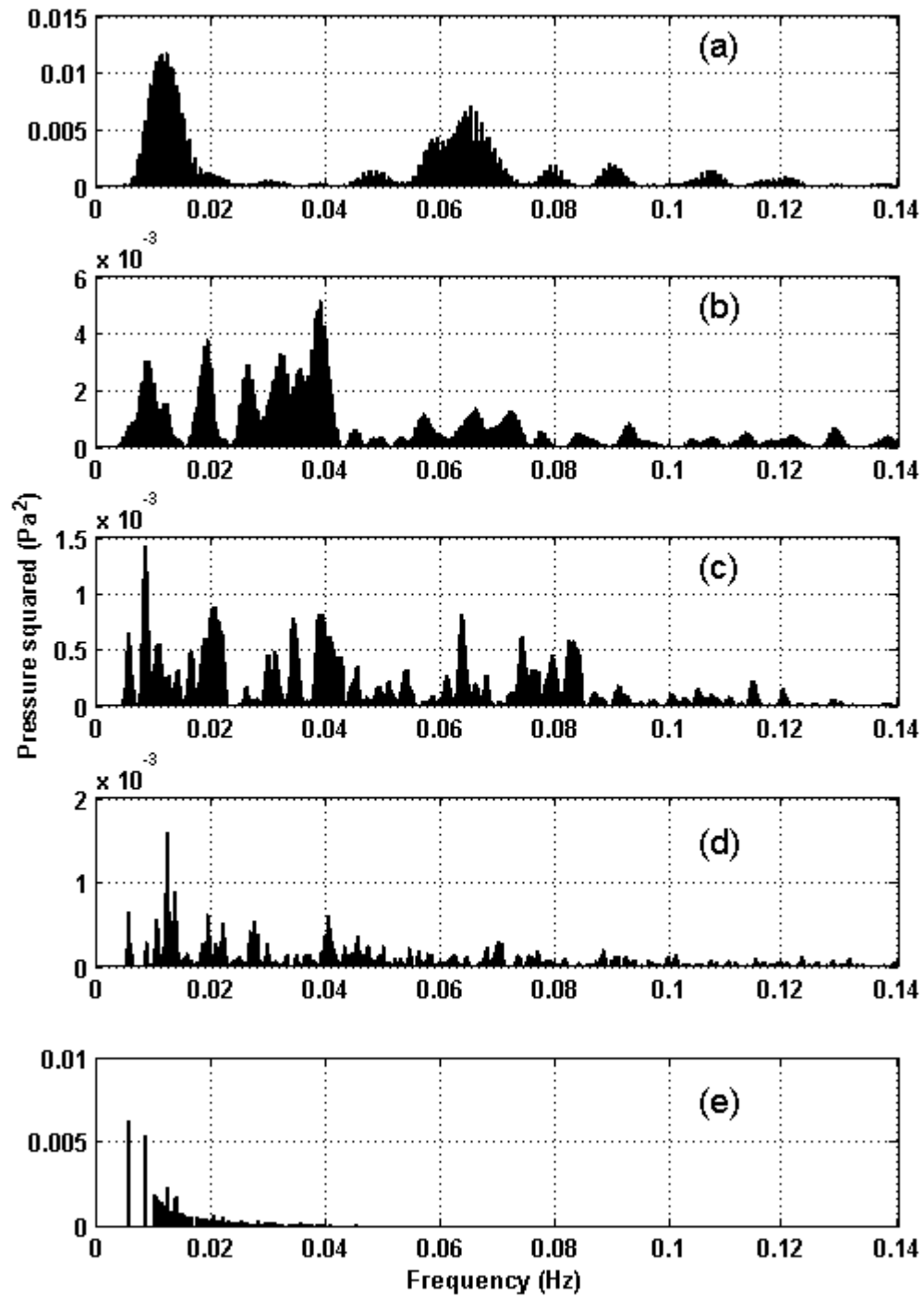


Figure 5.5. Octave-band predicted energy impulse response of the R1 configuration: a) wave-based, 500 Hz; b) wave-based 1000 Hz; c) wave-based, 2000 Hz; d) wave-based, 4000 Hz; e) energy-based.

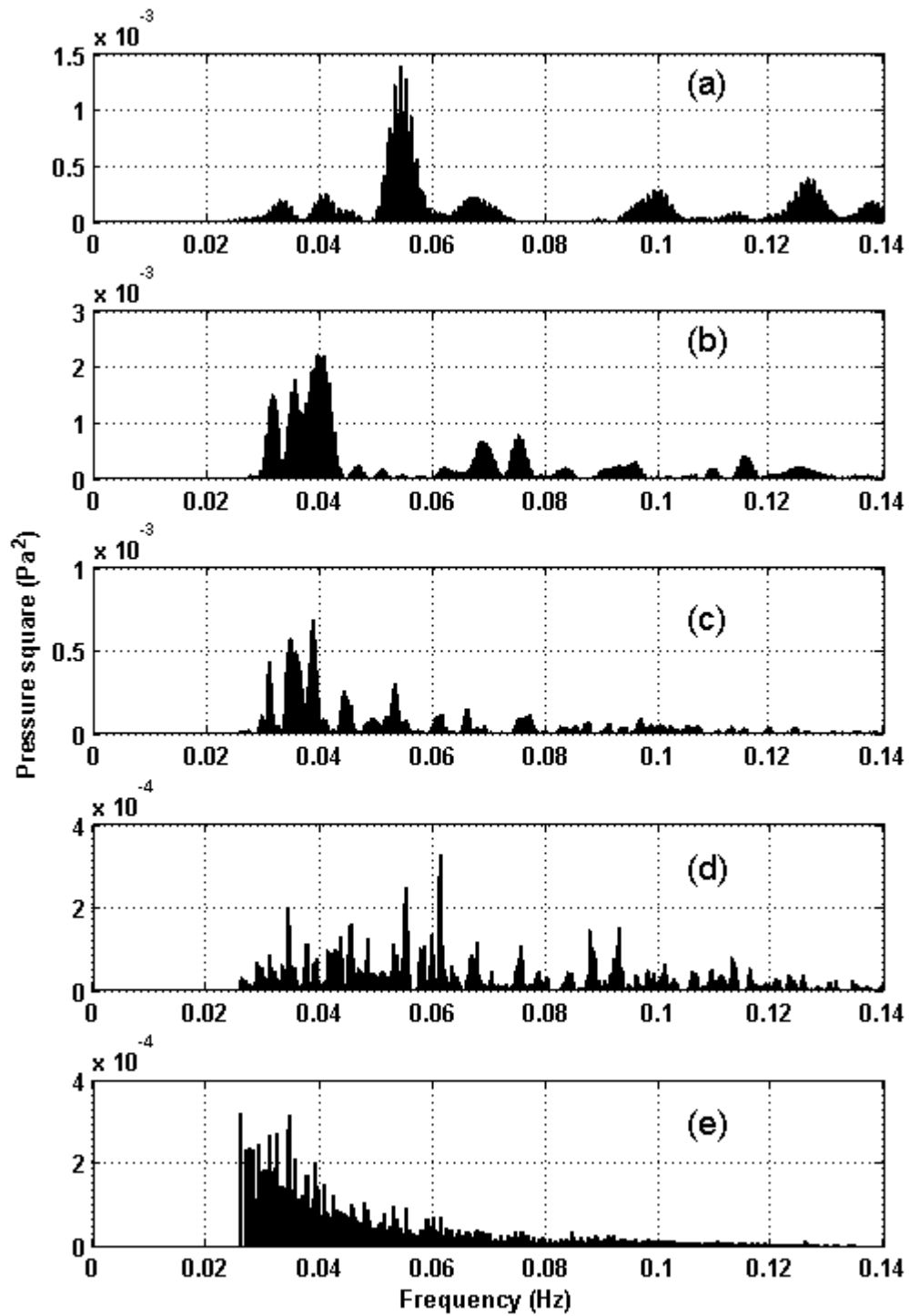


Figure 5.6. Octave-band predicted energy impulse response of the R2 configuration: a) wave-based, 500 Hz; b) wave-based 1000 Hz; c) wave-based, 2000 Hz; d) wave-based, 4000 Hz; e) energy-based.

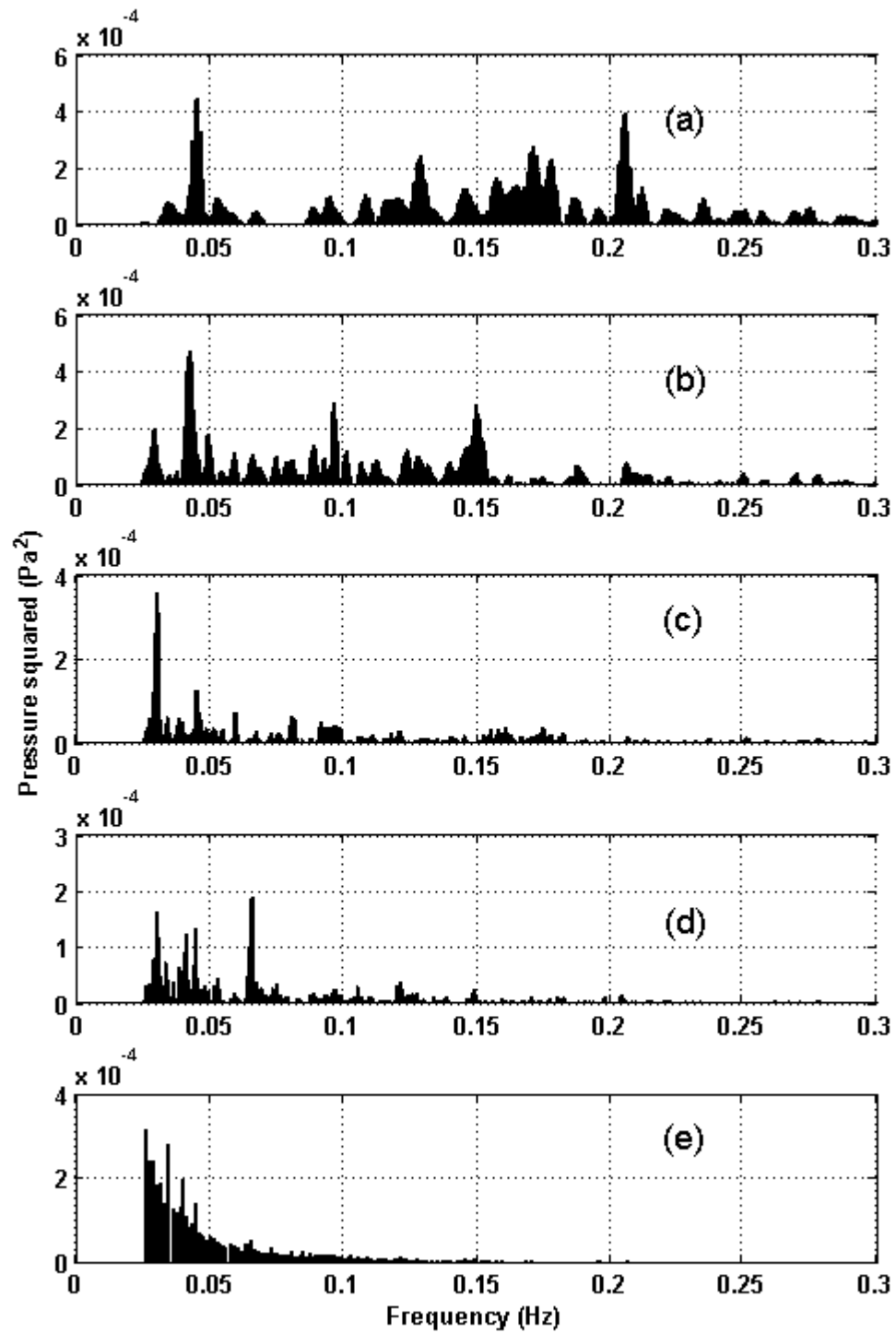


Figure 5.7. Octave-band predicted energy impulse response of the R3 configuration: a) wave-based, 500 Hz; b) wave-based 1000 Hz; c) wave-based, 2000 Hz; d) wave-based, 4000 Hz; e) energy-based.

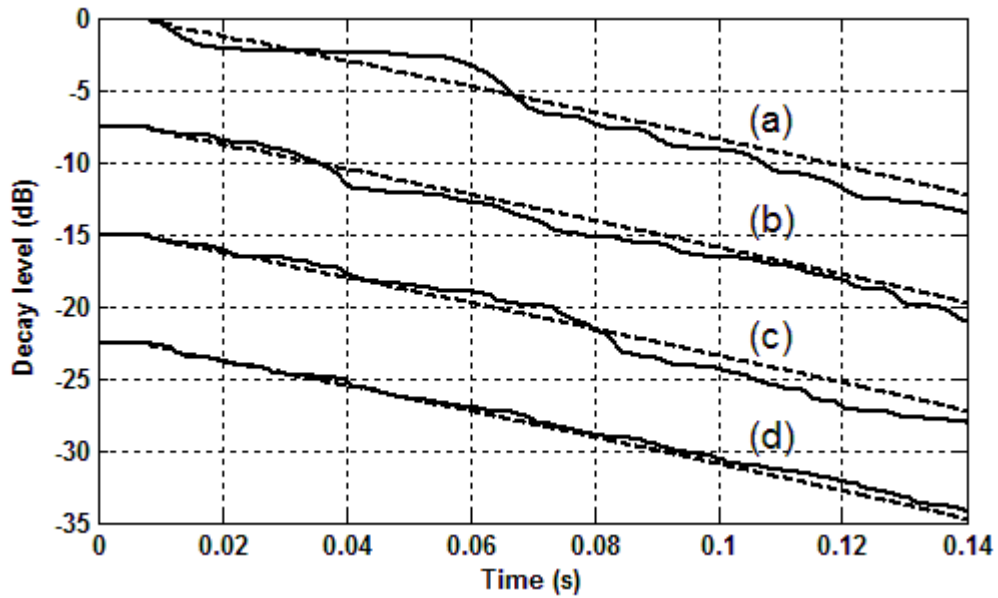


Figure 5.8. Octave-band sound-decay curves for configuration R1: a) 500 Hz, b) 1000 Hz, c) 2000 Hz, d) 4000 Hz. Solid lines: wave-based; dashed lines: energy-based. Curves for (b), (c) and (d) were moved -7.5, -15 and -22.5 dB, respectively, so that details can be seen.

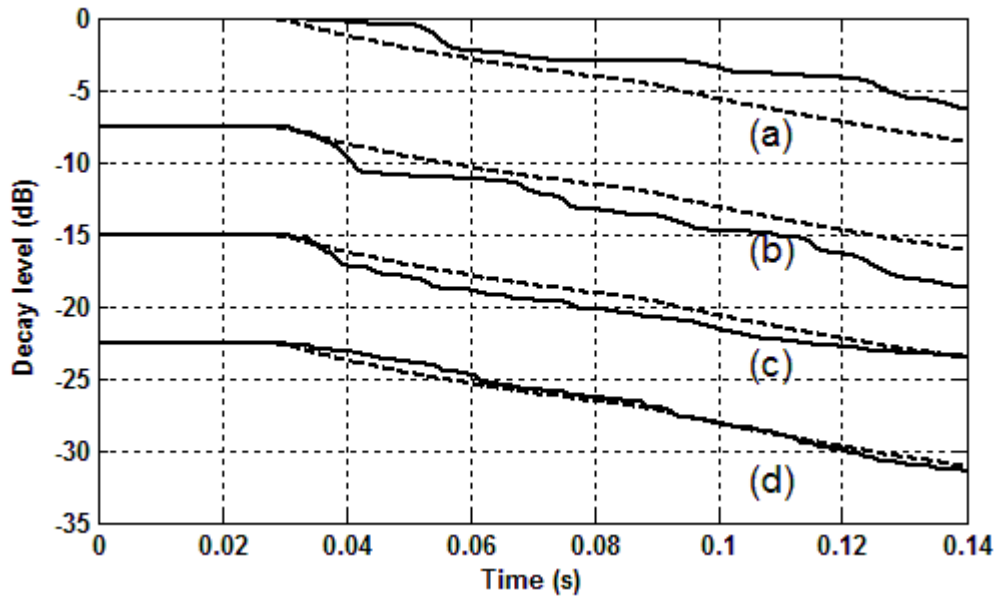


Figure 5.9. Octave-band sound-decay curves for configuration R2: a) 500 Hz, b) 1000 Hz, c) 2000 Hz, d) 4000 Hz. Solid lines: wave-based; dashed lines: energy-based. Curves for (b), (c) and (d) were moved -7.5, -15 and -22.5 dB, respectively, so that details can be seen.

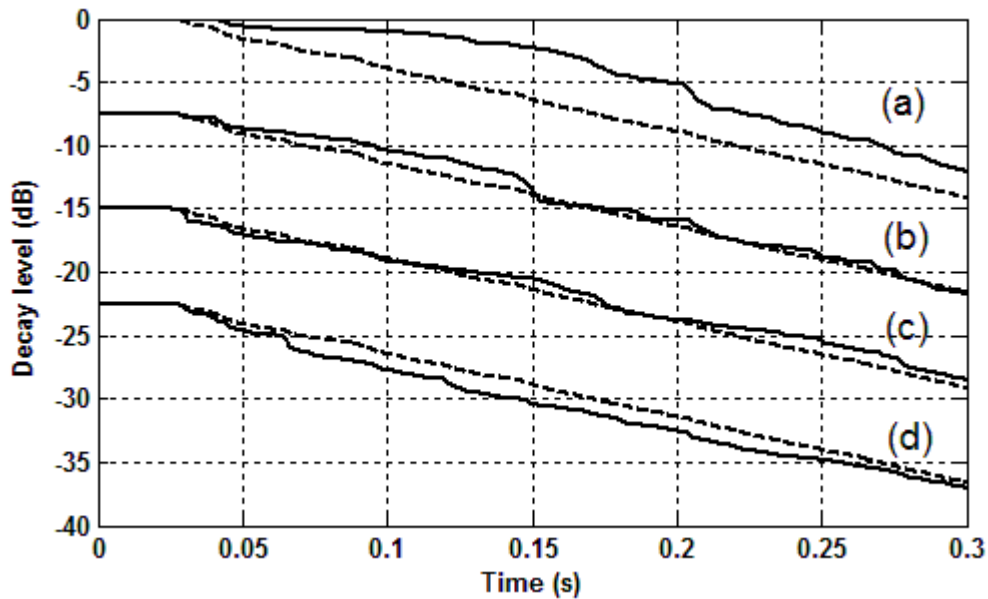


Figure 5.10. Octave-band sound-decay curves for configuration R3: a) 500 Hz, b) 1000 Hz, c) 2000 Hz, d) 4000 Hz. Solid lines: wave-based; dashed lines: energy-based. Curves for (b), (c) and (d) were moved -7.5, -15 and -22.5 dB, respectively, so that details can be seen.

There was no point in studying all of the room-acoustical parameters defined in section 3.7, because many of them are highly correlated [74]. For example, if an impulse response gives a short center time, it will result in a high value of ‘definition’ as well – see Eqs. (2.27) and (2.29). In the extreme case of a diffuse sound field, all of the parameters can be expressed in terms of the reverberation time; they therefore provide no further information about the sound field.

Only three of the room-acoustical parameters introduced in section 3.7 were studied in this chapter: a measure of the steady-state characteristics of the sound field (sound strength), a measure of the temporal variations of the sound field (reverberation time), and a measure of how well the sound field transmits speech (RASTI). Variations in these parameters due to changes in configuration and prediction type are discussed in detail; these variations will be considered significant if they are audible; *i.e.* greater than the just-noticeable differences mentioned in section 3.7.

For ease of reference, extended-reaction modeling of test surfaces is referred to with the suffix ‘ext’; likewise, the suffix ‘loc’ indicates local-reaction modeling of test surfaces. This abbreviation is mainly used in the figures. For example, WBR-loc refers to values which were obtained using the wave-based model with real-valued reflection coefficients, assuming local reaction of the test surface. Moreover, the difference between the parameters predicted with the test surfaces modeled as of local and extension reaction is referred to as the “L-E difference”; likewise, the difference between predictions made using real and complex reflection coefficients is referred to as the “R-C difference”. In both cases, only the magnitude of the difference is considered.

5.5.1 Sound Strength

Sound strength is a measure of the perceived loudness of the sound. It is the steady-state sound-pressure level normalized to the sound-pressure level of the same source measured in a free field at a distance of 10 m. Since the output power of the sound source used in this study has a constant level (L_w) of 80 dB at all frequencies, sound strength can be simply calculated as follows [140]:

$$G = L_p - L_w + 31 = L_p - 49 \quad (5.1)$$

where L_p is the steady-state sound-pressure level at the receiver position. As a result, the study of sound strength in this section is in part the same as Wareing’s study of steady-state sound-pressure levels; thus, comparing the new results with Wareing’s results validates the new model. In addition to considering the effects of surface-reaction models on the steady-state response of the test configurations, the current work studies the effects of phase change on reflection, as well as neglecting all phase effects (energy-based modeling).

Wareing calculated the transfer function of the room from 50 to 4000 Hz with a frequency resolution of 10 Hz. To calculate the octave-band sound-pressure levels, he added the

squared pressures at all frequencies in the corresponding band. This is equivalent to using a rectangular filter, except that the sum of the squared pressures was not divided by the bandwidth of the filter. In the present research, a frequency resolution of 0.5 Hz was used, 20 times finer than that of Wareing. As a result, when calculating steady-state sound-pressure levels, more values were added and higher sound-pressure levels were predicted, as shown in Figure 5.11. In order to make current predictions comparable to Wareing’s results, the average squared pressure of each octave band was used instead. Sound-pressure levels predicted in this way are directly comparable for both Wareing’s and the current predictions – see Figure 5.11. Predicted sound-strength values for the twelve test configurations are shown in Figures 5.12 and 5.13.

The L-E difference is inaudible (*i.e.* below 1 dB) for all predictions in configurations G1, G2 and G3. Moreover, it can be seen that phase change on reflection has no audible effect on the sound strength. Energy-based predictions are very different from wave-based prediction, and

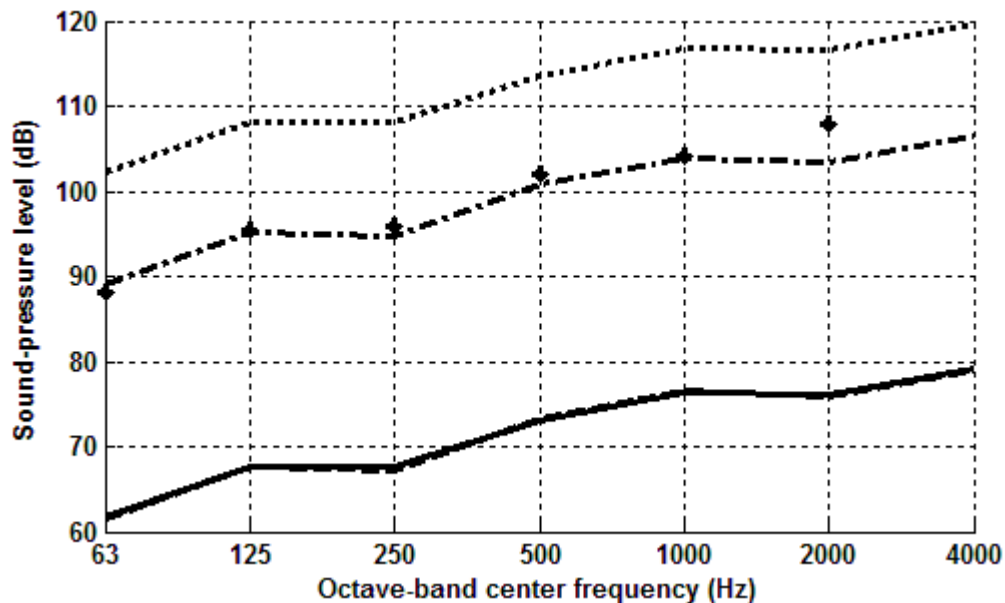


Figure 5.11. Octave-band steady-state sound-pressure levels for configuration G1-ext, using 3920 beams and 50 reflections. Diamonds: Wareing’s original results; dash-dot line: total levels, 10-Hz resolution; dotted line: total levels, 0.5-Hz resolution; dashed line: average levels, 10-Hz resolution, solid line: average levels, 0.5-Hz resolution.

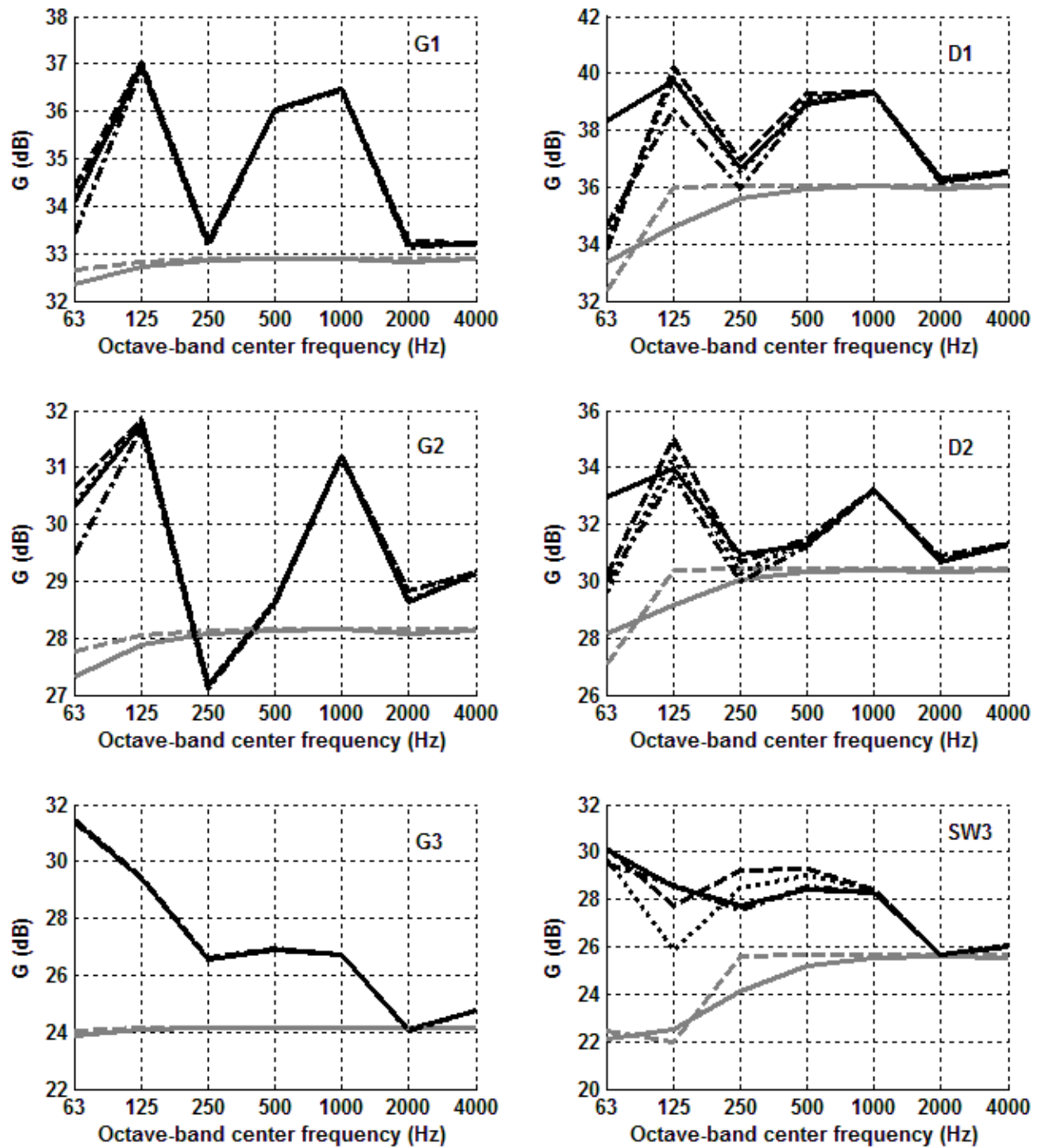


Figure 5.12. Octave-band sound strength G for six configurations: G1, D1, G2, D2, G3 and SW3. Grey lines: energy-based predictions; solid line: EBR-ext, dashed line: EBR-loc. Black lines: wave-based predictions; solid line: WBC-ext, dashed line: WBC-loc, dash-dot line: WBR-ext, dotted line: WBR-loc.

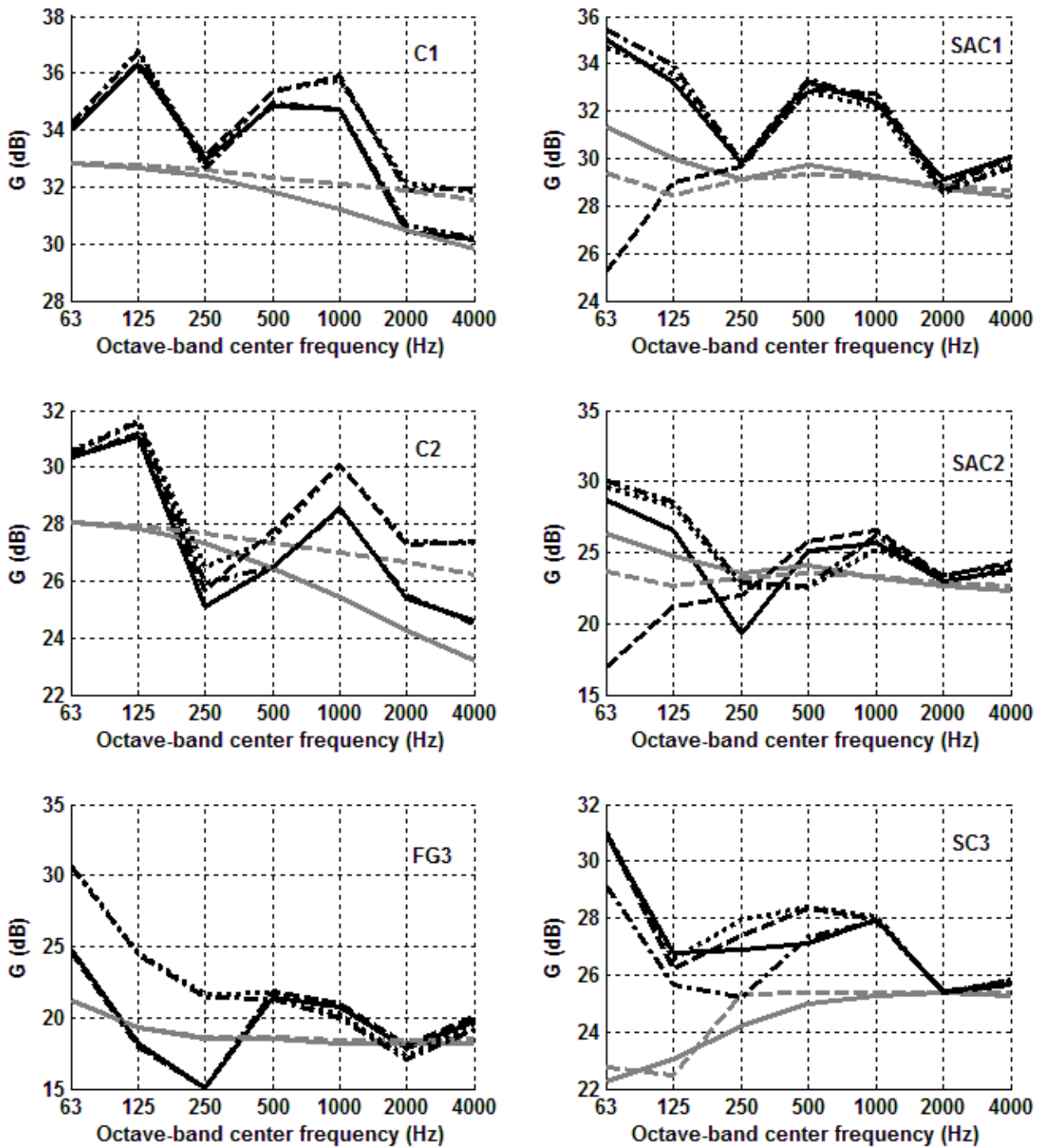


Figure 5.13. Octave-band sound strength G for six configurations: C1, SAC2, C2, SAC2, FG3 and SC3. Grey lines: energy-based predictions; solid line: EBR-ext, dashed line: EBR-loc. Black lines: wave-based predictions; solid line: WBC-ext, dashed line: WBC-loc, dash-dot line: WBR-ext, dotted line: WBR-loc.

do not result in audible changes over the considered frequency range. These results are consistent with those reported by Wareing.

The only audible L-E differences in configurations D1 and D2 occur in the 63 and 125 octave bands. In general, higher sound strengths are predicted in the local-reaction case. At 63 Hz, the WBC-ext model predicts sound strengths to be 3 to 4 dB higher than all other models. This is because of the mass-air-mass resonance, as already explained in Figure 5.1.

In configuration SW3, the workshop with double-steel panels as its walls, audible L-E differences occurred at 125 and 250 Hz only. The local-reaction models predicted lower sound strengths than the extended-reaction models at 125 Hz, but higher sound strengths at 250 Hz. This can be explained by considering the absorption characteristics of the DSP test surfaces, as shown in Figure 5.1; the local-reaction model predicts higher absorption coefficients than the extended-reaction model at 125 Hz, but lower values at 250 Hz. When DSP is used as the ceiling of the workshop in SC3, L-E differences become audible at 63 and 500 Hz as well. This suggests that the positioning of the test surfaces influences the sound strength. At 250 Hz, the results are still mainly influenced by the mass-air-mass resonance. At 500 Hz, the absorption coefficient of the local-reaction model is lower, and the corresponding sound strengths are accordingly predicted to be higher. The WBC-ext model predicts higher sound strengths than does the WBR-ext model, which shows the importance of modeling phase; this is most significant near the resonance frequency.

As expected, no audible L-E differences occurred in configuration FG3. However, phase changes due to reflection have the most significant influence on sound strength in this configuration; of course, this is only detectable using the wave-based models. In octave bands from 63 to 250 Hz, the WCR models predict 5 to 7 dB higher sound strengths. Following Wareing, this difference is explained by studying the characteristics of the reflection coefficient

of the test surface, which correspond to the angle of incidence of the first-order reflection path. As presented in Table 5.3, Wareing calculated the incident angles of the first-order reflection paths for the three rooms. Figure 5.14 shows the reflection coefficient of the FR test surface at 76 degrees. The R-C difference can be explained based on the opposite signs of the real and imaginary parts of the reflection coefficient at frequencies below 230 Hz. As the real part of the reflection coefficient goes to zero from 0 to 230 Hz, the imaginary part of the reflection coefficient becomes more significant and the R-C difference increases. Above 230 Hz, however, this difference decreases, as the real and imaginary parts of the reflection coefficient have the same sign. The difference also decreases with frequency as the imaginary part of the reflection coefficient decreases.

In configurations C1 and C2, no audible difference in the sound strength is caused by phase changes due to reflection. As the frequency increases, on the other hand, the L-E difference increases. As was shown in Figure 5.2, the local-reaction model predicts lower absorption coefficients for the CAF test surface than the extended-reaction model, with the difference between the two models increasing with frequency. As a result, the local-reaction models predict higher sound strengths than the extended-reaction models, with the L-E difference increasing with frequency.

Table 5.3. Incident angles corresponding to first-order reflection paths for the three rooms [133].

Room	θ_{ceiling} (deg)	θ_{floor} (deg)	θ_{wall} (deg)
1 (office)	42.3	27.8	33.7
2 (corridor)	76.3	67.1	71.6
3 (workshop)	76.3	67.1	42.0

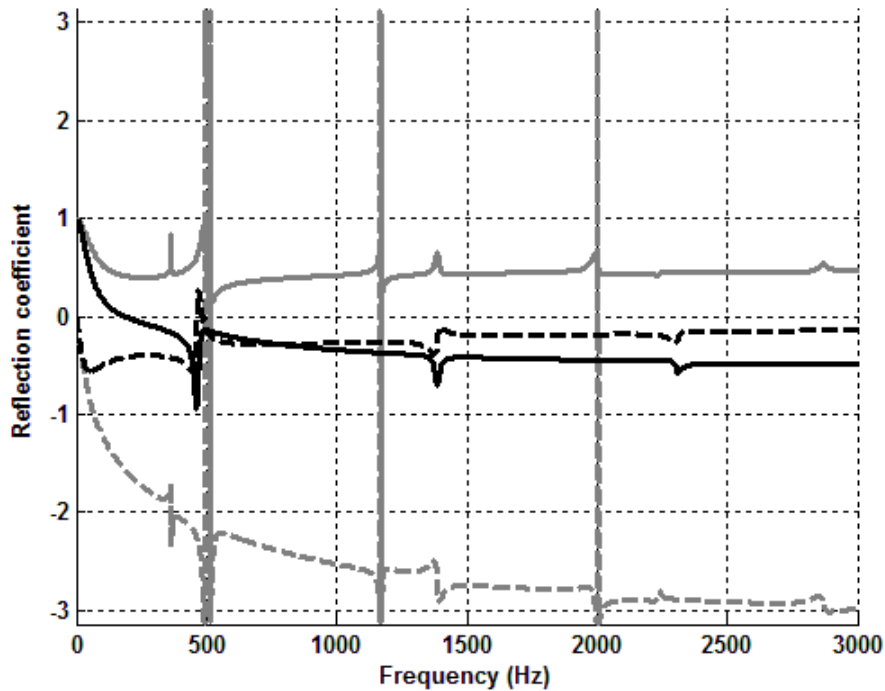


Figure 5.14. Predicted reflection coefficient of the FR test surface, fibreglass on rigid backing, at the 76° angle of incidence. Black solid line: magnitude; black dashed line: phase (radians); grey solid line: real part; grey dashed line: imaginary part.

The most significant L-E difference is observed in configurations SAC1 and SAC2, at the lowest frequencies. In the 63 and 125 Hz octave-bands, the WBC-loc model predicts sound strengths which are, respectively, more than 10 and 5 dB lower than the other wave-based models. As frequency increases, however, the difference between the models becomes smaller. The L-E differences at lower frequencies are explained by considering the angular variations of the real part and absolute value of the reflection coefficients of the FA test surfaces at 45, 90, 125 and 180 Hz, as shown in Figure 5.15. 45 and 90 Hz are the lower and upper limits of the octave band centered at 63 Hz, and 180 Hz is the upper frequency of the 125-Hz octave band. At 45 Hz, the real part of the local-reaction reflection coefficient is greater than the extended-reaction reflection coefficient at all angles of incidence, with their difference increasing with angle of incidence. Most importantly, the real parts of the two reflection coefficients have opposite signs for incident angles greater than 40°. As frequency increases to the upper frequency

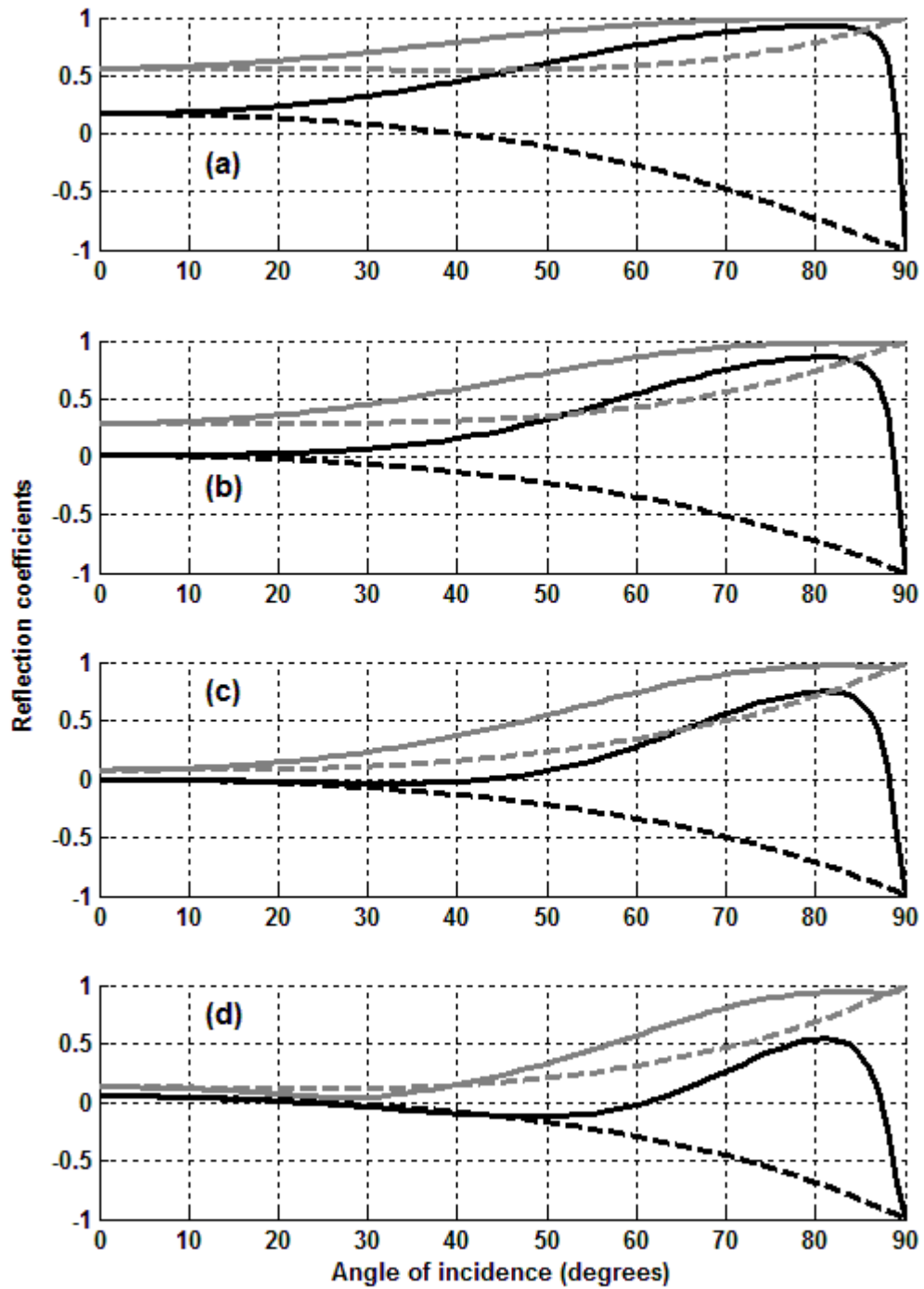


Figure 5.15. Predicted real part and absolute value of the reflection coefficient of the FA test surface, as a function of incident angle at: a) 45 Hz, b) 90 Hz, c) 125 Hz and d) 180 Hz. Black curves: real parts; grey curves: absolute values. Solid lines: extended-reaction; dashed lines: local-reaction.

limit, 90 Hz, this transition of the sign of the real part of the reflection coefficient happens at a lower incident angle. Consequently, for the majority of the local-reaction reflection coefficients in the 63-Hz octave band, their real part has a different sign than the extended-reaction reflection coefficients. This is particularly important when we consider that, according to Table 5.3, the first-order reflections in the SAC1 and SAC2 configurations occur at 42.3° and 76.3°, respectively. As frequency increases, the real part of the extended-reaction reflection coefficient gradually becomes negative as well; the real parts of the reflection coefficients have different signs only for incident angles greater than 44° at 125 Hz and 61° at 180 Hz. This is consistent with the fact that sound strengths predicted by the WBC-loc model are significantly different from those predicted by the other methods at 63 and 125 Hz.

In the case of the energy-based model, the local-reaction sound strengths are lower than those with extended-reaction at the lowest frequencies, with the difference decreasing with frequency. This general trend can be explained by considering the absorption coefficient of the FA test surface, shown in Figure 5.2: as frequency increases, the difference between the local- and extended-reaction absorption coefficients decreases. The same explanation applies to the WBR model.

5.5.2 Reverberation Time

The predicted reverberation times, T_{20} , of the test configurations are shown in Figures 5.16 and 5.17, and will be studied in this section.

In configurations G1, G2 and G3, the different surface-reaction models do not affect the reverberation times significantly, except at low frequencies. When surfaces are modeled as of local reaction, the predicted reverberation times are slightly higher than when they are modeled as of extended reaction; especially at the lowest frequencies, the L-E differences become

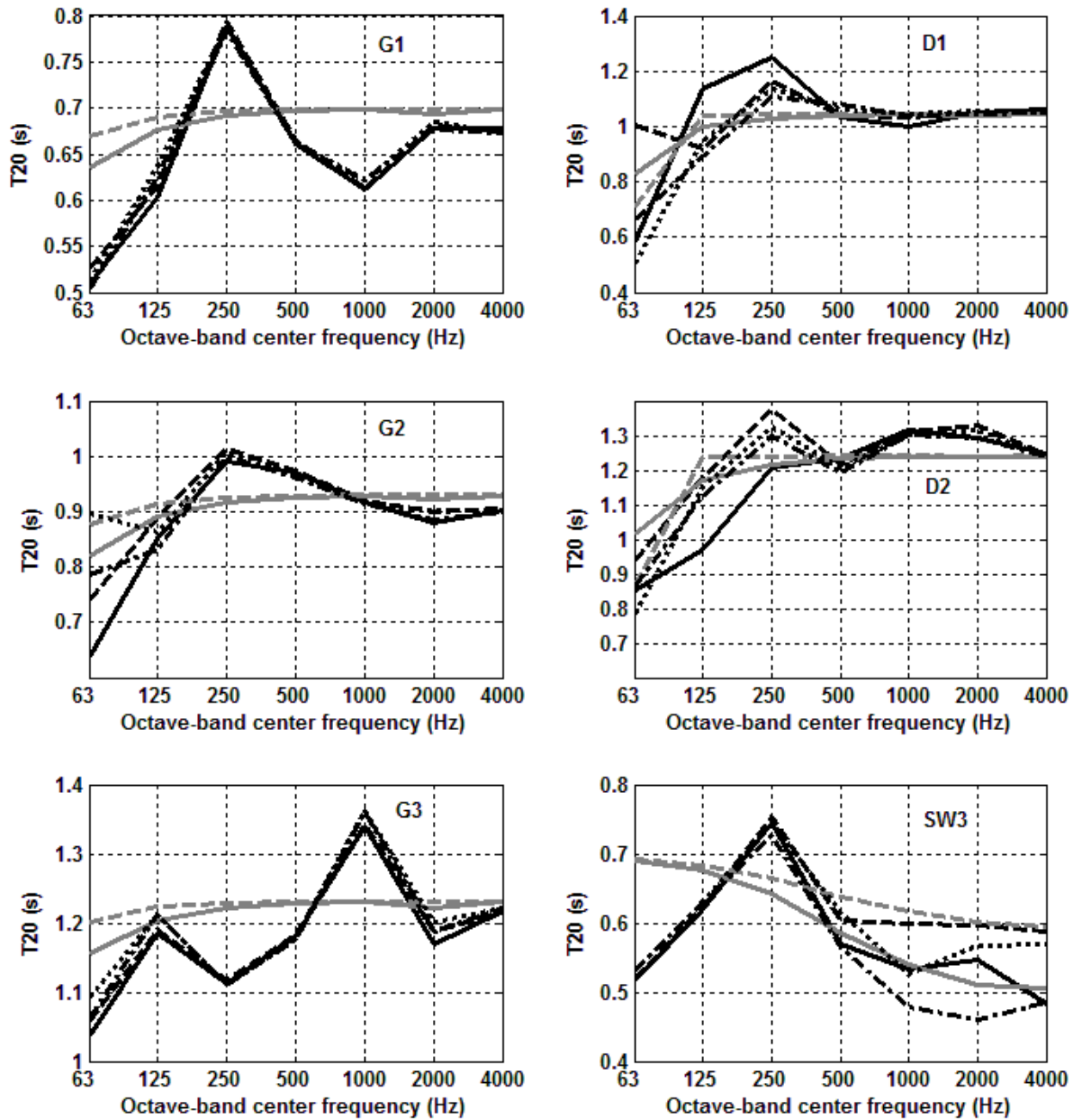


Figure 5.16. Predicted octave-band reverberation times T_{20} for six configurations: G1, D1, G2, D2, G3 and SW3. Grey lines: energy-based predictions; solid line: EBR-ext, dashed line: EBR-loc. Black lines: wave-based predictions; solid line: WBC-ext, dashed line: WBC-loc, dash-dot line: WBR-ext, dotted line: WBR-loc.

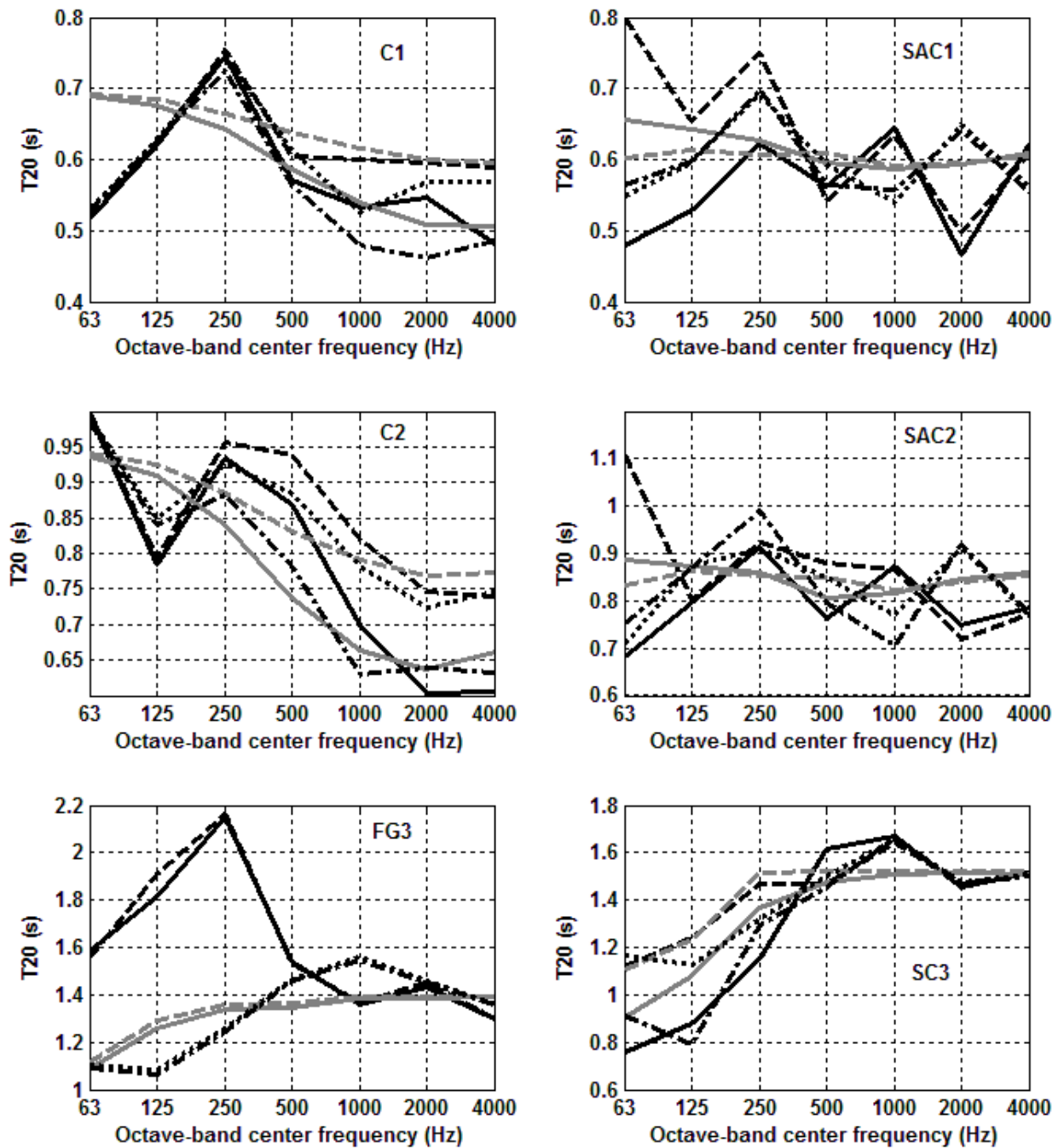


Figure 5.17. Predicted octave-band reverberation times T_{20} for six configurations: C1, SAC2, C2, SAC2, FG3 and SC3. Grey lines: energy-based predictions; solid line: EBR-ext, dashed line: EBR-loc. Black lines: wave-based predictions; solid line: WBC-ext, dashed line: WBC-loc, dash-dot line: WBR-ext, dotted line: WBR-loc.

significant. This can be explained by considering the diffuse-field absorption coefficients in Table 5.2; higher reverberation times correspond to lower absorption coefficients. In addition, L-E differences are observed at 1000 Hz in the wave-based models in Rooms 1 and 3. Since the energy-based model predicts zero L-E difference at 1000 Hz, the differences predicted by the wave-based models must be due to interference effects. The only significant R-C difference occurs at 63 Hz in G2.

In configurations D1 and D2, significant changes occur only at frequencies below 500 Hz. The predicted L-E differences are caused by the mass-air-mass resonance frequency, and are consistent with the absorption characteristics of the DDW test surface, as shown in Figure 5.1. Similar trends are observed in configuration SC3. Except at resonant frequencies, the imaginary parts of the reflection coefficients of test surfaces DDW and DSP are negligible; as a result, the R-C differences are not significant except near the mass-air-mass resonance frequency.

L-E differences in configurations C1 and C2 increase with frequency, which correlates with the difference between the local- and extended-reaction absorption coefficients in Figure 5.2. Moreover, R-C differences are significant in the 250-Hz and higher octave bands.

In configuration FG3, the same explanations which were used to describe R-C differences in sound strength apply to reverberation times as well – see Figure 5.14. The local-reaction model predicts slightly higher reverberation times than the extended-reaction model.

Significant L-E differences, as well as R-C differences, are observed in configurations SAC1 and SAC2. L-E differences in reverberation times are most significant at lower frequencies; the same argument that was used in explaining the L-E differences in the case of sound strength can be used for reverberation times as well – *i.e.* different signs of the real parts of the local- and extended-reaction reflection coefficients. L-E differences become less significant as frequency increases, which is consistent with the decreasing difference between

local- and extended-reaction diffuse-field absorption coefficients of the FA surface shown in Figure 5.2.

5.5.3 Speech Intelligibility

RASTI (Rapid Speech Transmission Index) was used in this research to study the intelligibility of speech in the test configurations. The perceived quality of speech is typically related to different ranges of STI values [85], as shown in Table 5.4. It is assumed here that the same interpretation applies to RASTI as well.

Predicted RASTI values are presented in Figure 5.18 for all room configurations. The most significant observation is that the energy-based model consistently predicts much higher RASTI values than the wave-based models, values corresponding to ‘excellent’ speech intelligibility. With the exception of configuration FG3, the energy-based model predicts the lowest RASTI values in Room 3 and the highest RASTI values in Room 1. Given that higher reverberation times are correlated with lower STI values [14], this is consistent with the fact that the reverberation times are generally highest in Room 3 and lowest in Room 1. The same trend is observed in predictions using the wave-based models.

L-E differences in RASTI predicted by the energy-based model are inaudible (less than 0.03 [15]) for all configurations. In the case of wave-based models, L-E differences are audible only in three configurations C1, C2 and SAC1. Since the calculation of RASTI is based on the two octave bands at 500 and 2000 Hz, L-E differences in RASTI can partly be explained by

Table 5.4. Relation between STI values and speech-intelligibility ratings [85].

STI range	0 – 0.3	0.3 – 0.45	0.46 – 0.60	0.60 – 0.75	0.75 – 1
Speech-intelligibility rating	unintelligible	poor	fair	good	excellent

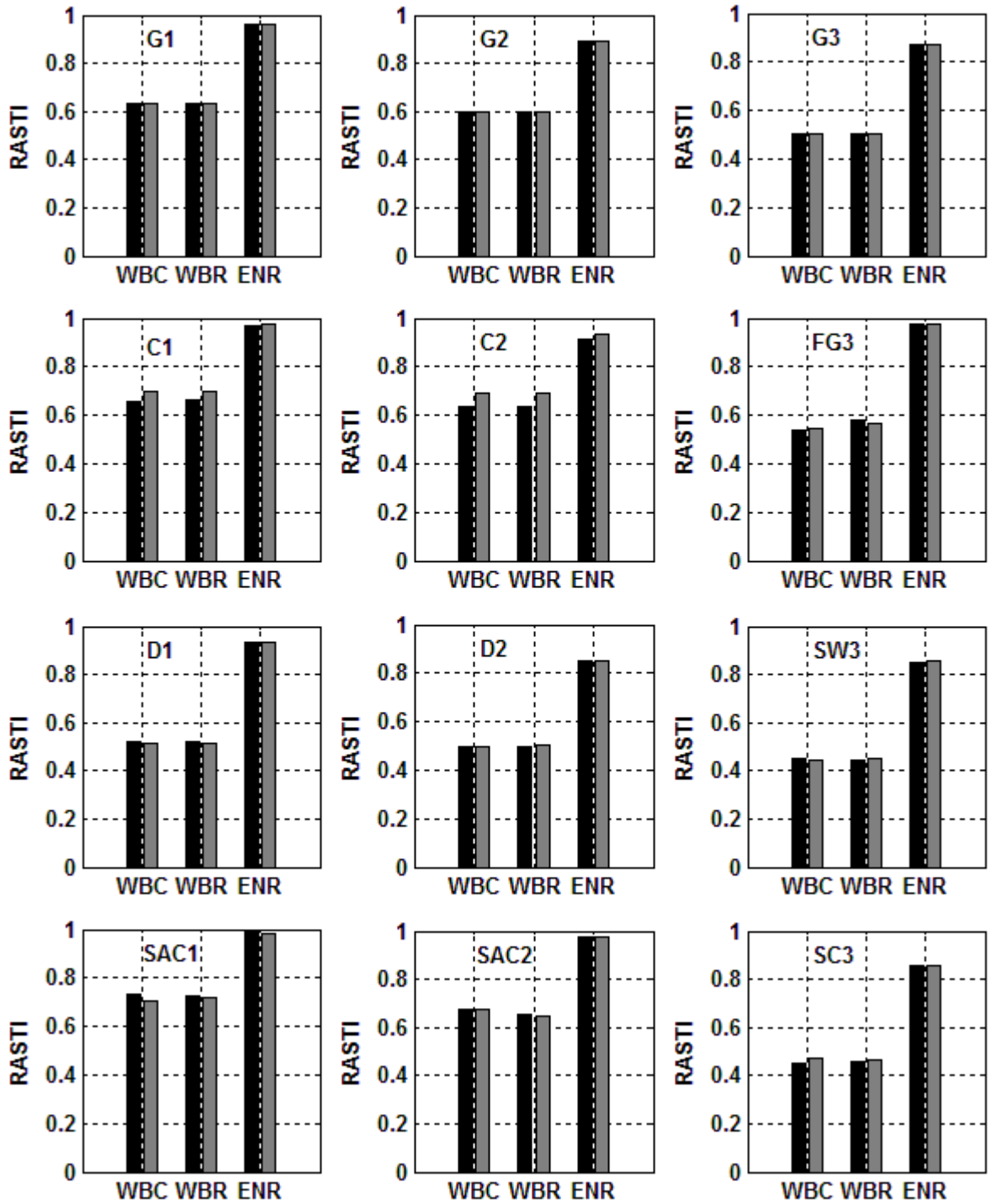


Figure 5.18. Predicted RASTI values for all test configurations. Black bars: extended-reaction; Grey bars: local-reaction. WBC: wave-based prediction with complex reflection coefficients; WBR: wave-based prediction with real reflection coefficients; ENR: energy-based prediction with real reflection coefficients.

considering the L-E differences in T_{20} in these two octave bands. Therefore, significant L-E differences in RASTI values would be expected in configurations C1 and C2. Less significant L-E differences would be expected in configurations SW3 and SAC2, because they show significant L-E differences in only one of the two relevant octave bands. Consistent with this reasoning, L-E differences in RASTI can be explained in configurations C1, C2, SW3, and SAC2; the L-E differences are audible in the first two configurations and inaudible in the last two. Nevertheless, the L-E difference in configuration SAC1 remains unexplained. R-C differences in RASTI are less significant than L-E differences, and are only audible in configuration FG3 with the test surface modeled as of extended reaction.

In general, configurations that have a test surface with very low absorption (G1, G2, G3, D1, D2, SW3 and SC3) have ‘fair’ speech intelligibility, while configurations that have absorptive surfaces (C1, C2, SAC1, SAC2 and FG3) have ‘good’ speech intelligibility; exceptions are configurations G1 and FG3, which have ‘good’ and ‘fair’ speech intelligibility, respectively. It is expected that more significant changes in speech intelligibility would occur if STI was used instead of RASTI, because STI is evaluated based on seven octave bands, while RASTI is based on only two.

5.6 Summary

Beam-tracing predictions of sound strength, reverberation time and RASTI in twelve room configurations were presented and discussed. The following is a summary of these results obtained in this chapter:

- Wave-based predictions showed significant variations in sound strength and reverberation time with frequency. Energy-based predictions, on the contrary, showed much smoother and smaller variations with frequency for both parameters.

- For configurations with a single solid panel, different surface-reaction models caused no audible changes to any of the three parameters, except for the reverberation time of the corridor at the lowest frequency, which is most likely due to interference effects.
- In the case of configurations that included solid double-panel partitions with an air gap, the only audible effects of changing the surface-reaction model occurred around the mass-air-mass resonance frequency. This is because local- and extended-reaction models predict significantly different reflection characteristics at the resonance frequency, both in magnitude and phase. These differences influenced sound strength and reverberation time, but not RASTI values.
- When a single layer of porous material on a rigid backing was used as a test surface, significant changes occurred only at lower frequencies and due to phase change on reflection. Modeling the surface as of local or of extended reaction, however, had no audible effects on any of the three parameters.
- When a second layer of porous material was added to the test surface, significant changes in all three parameters occurred. Local- or extended-reaction modeling of the test surfaces made significant differences in sound strength and reverberation time at frequencies above 500 Hz. Phase change on reflection, on the other hand, made significant changes to reverberation time in the 125-Hz and higher octave bands, but did not make audible changes in sound strength. The most significant changes in energy-based predictions occurred for this configuration, for all parameters.
- The most significant changes between local- and extended-reaction modeling of test surfaces was in the case of a porous layer with an air gap. This was explained by the fact that the local-reaction assumption is not valid for a layer of air. As a result, significant changes in both reverberation time and sound strength were observed at low frequencies.

At higher frequencies, phase change on reflection made significant changes in predicted reverberation time, but not sound strength.

- The energy-based model consistently predicted much higher RASTI values than the wave-based models. Based on predicted values of RASTI, rooms having very low absorption have 'fair' speech intelligibility, whereas rooms that have absorptive surfaces have 'good' speech intelligibility. Moreover, RASTI values are generally predicted to have a negative correlation with the size of the room. In both cases (higher absorption and smaller rooms), lower speech intelligibility is most likely due to high reverberation times.

Chapter 6

Conclusions

6.1 Accomplishments

The objective of this work was to develop a beam-tracing model for the prediction of sound fields in rooms – in particular, the transient response and derived acoustical parameters. The model was based on an existing wave-based triangular-beam-tracing model developed for predicting steady-state sound fields in empty rooms with specularly-reflecting, extended-reaction surfaces. Room surfaces were modeled as multiple layers of solid, fluid or poroelastic materials, and their acoustical properties were calculated using a transfer-matrix approach. The model was used to study the effects of modeling room surfaces as of local or of extended reaction on steady-state sound-pressure levels in different room configurations.

In the present work, the existing model was upgraded to calculate the pressure impulse responses of rooms. This enables calculation of room-acoustical parameters that correlate with different aspects of the subjective perception of sound. Moreover, energy-based modeling was implemented in the new model, so that energy-based impulse responses and room-acoustical parameters could be compared with those obtained using wave-based modeling.

The transfer-matrix algorithm which is used for calculating the acoustical properties of the multilayer surfaces had not been implemented in the existing model in the most computationally-efficient way, resulting in very long runtimes. Therefore, the computational efficiency of the model was improved and the transfer-matrix algorithm was implemented in a more efficient way. As a result, impulse responses can be predicted with the new beam-tracing model for rooms containing multilayer surfaces, within reasonable runtimes.

A wave-based ray-tracing model was previously developed at UBC Acoustics and Noise Research Group; it could account for diffuse surface reflections according to Lambert's law, and sound diffraction based on the uniform theory of diffraction. The possibility of exporting these features to the new beam-tracing model was investigated in this research. Specifically, a literature review was done on modeling sound diffraction, and an exact formulation was chosen to replace the uniform theory of diffraction, which is a high-frequency approximation for infinitely-long wedges. It was shown that, for high frequencies and long wedges, the two models give similar results.

Within the ray-tracing model, the direction of both the diffracted rays and diffuse reflections were determined through a random process. This is compatible with the statistical nature of the ray-tracing model. Beam-tracing models, on the contrary, are deterministic and use many fewer beams than rays. Consequently, beam-tracing predictions did not converge within

reasonable runtimes with the diffuse-reflection and diffraction algorithms imported from the ray-tracing program.

6.2 Summary of Results

Beam-tracing predictions of the sound-fields in twelve room configurations were presented and discussed in Chapter 5. Wave-based and energy-based predictions were made in each configuration, and the results compared. In the case of the wave-based model, the importance of modeling phase changes on reflection was studied by using both complex- and real-valued reflection coefficients; the real-valued reflection coefficient was chosen as the magnitude of the complex-valued reflection coefficient. Three room-acoustical parameters were studied for each configuration: a measure of the steady-state characteristics of the sound field (sound strength), a measure of the temporal variations of the sound field (reverberation time), and a measure of how well the sound field transmits speech (RASTI). Variations of these parameters due to changes in configuration and prediction mode were discussed, and explained by considering the absorption and reflection characteristics of the test surfaces used in each configuration. The following remarks summarize the findings on the significance of predicting the acoustical parameters using different models:

- *Energy-based and wave-based modeling:* Very significant changes occurred in all three parameters when interference effects were ignored, whether partly (ignoring phase change on reflection) or entirely (tracing sound energy instead of sound pressure). Further, accounting for phase changes due to distance traveled was found to be far more significant than phase change on reflection. With the wave-based model, predicted reverberation time and sound strength changed significantly with frequency; in the case of energy-based prediction, these variations were less significant. When predictions were energy-based, the room-acoustical parameters were less significantly influenced by

change of the surface-reaction model. The energy-based model consistently predicted higher RASTI values than the wave-based models.

- *Local and extended reaction of surfaces:* Modeling surfaces as of local or of extended reaction is significant for surfaces that consist of multiple layers, specifically when one of the layers is air. This affects the corresponding reverberation time and sound strength significantly; changes in RASTI, however, are mostly inaudible. For multilayers of solid materials with an air cavity in-between, significant changes occurred around their mass-air-mass resonance frequency, and therefore at lower frequencies. For single-layer surfaces, whether made of porous or solid materials, local- or extended-reaction modeling of the surface is generally insignificant. These results are consistent with Wareing's findings [133].
- *Phase change on reflection:* Modeling phase change on reflection was found to be significant in the case of surfaces for which the real part of their reflection coefficients changes its sign. At frequencies at which the sign of the real and imaginary parts of the reflection coefficient are different, significant changes were observed due to modeling phase change on reflection. For the configurations studied in this research, modeling phase change on reflection had no audible influence on RASTI values.

6.3 Future Work and Improvements

Suggestions are made for future improvements of the model. These are as follows:

- *Diffraction:* There are two aspects of the current diffraction algorithm that need to be improved. Most importantly, a deterministic direction must be chosen for diffracted beams. One possibility is to choose, for a given distance from the diffracting edge, the direction in which the energy of the diffracted sound is greater. This would be the direction in which the diffraction coefficient is the smallest in magnitude, and

corresponds to the most significant contribution of the diffracted beam. To retain computational efficiency, this information could be pre-calculated for the wedge configurations used in the room, and recalled during execution of the tracing algorithm. Moreover, the diffraction algorithm needs to be improved to account for sound diffraction over all free edges. Arbitrary positioning of the hanging walls inside the rooms should also be allowed.

- *Diffuse reflections:* Accounting for diffuse surface reflections is important for realistic prediction of sound fields. A deterministic (as opposed to statistical) algorithm is needed for modeling diffuse reflections within the beam-tracing model. One promising option is to incorporate acoustical radiosity into the beam-tracing model, as proposed by Lewers [82].
- *Adaptive tracing:* Currently, beams are traced by their center rays only. As a result, overlaps and missing reflections occur as the beam-fronts eventually become larger as they propagate in the room. In adaptive beam-tracing, the shape of the reflected beam is redefined by the shape of the reflecting surface, such that individual beams only encounter one surface. Adaptive tracing improves the accuracy of the model by finding more realistic reflection paths, and requires fewer beams than a non-adaptive beam-tracing model to obtain the same accuracy.
- *Modeling the effects of finite surface dimensions:* Once the diffraction algorithm is improved to account for sound diffraction from all free edges, it can be used to investigate the effects of diffraction from the edges of the room. These can be modeled as wedges with an angle of 270 degrees.

References

1. J.B. Allen and D.A. Berkeley, "Image Method for Efficiently Simulating Small-Room Acoustics", *J. Acoust. Soc. Am.*, **65** (4), 943-950 (1979).
2. J. Amanatides, "Ray Tracing with Cones", *Computer Graphics*, **18** (3), 129-135 (1984).
3. L.L. Beranek, *Music, Acoustics and Architecture* (John Wiley & Sons, U.S.A., 1962).
4. L.L. Beranek, *Concert and Opera Halls, How They Sound* (Acoustical Society of America, U.S.A., 1996).
5. L.L. Beranek, "Subjective Rank-Orderings and Acoustical Measurement for Fifty-Eight Concert Halls", *Acta Acustica united with Acustica*, **89**, 494-508 (2003).
6. L.L. Beranek, "Basic Acoustical Quantities: Levels and Decibels", *Noise and Vibration Control Engineering: Principles and Applications* (John Wiley & Sons, U.S.A., 2006).
7. C. Bibby, "Characterizing and Improving the Acoustical Performance of Profiled Architectural Surfaces", Internal Report, Acoustics and Noise Research Group, University of British Columbia (2009).
8. A. Billon, C. Foy, J. Picaut, V. Valeau and A. Sakout, "Modeling the Sound Transmission between Rooms Coupled through Partition Walls by Using a Diffusion Model", *J. Acoust. Soc. Am.*, **123** (6), 4261-4271 (2008).
9. S.R. Bistafa and J.W. Morrissey, "Numerical Solutions of the Acoustic Eigenvalue Equation in the Rectangular Room with Arbitrary (Uniform) Wall Impedance", *J. Sound & Vib.*, **263**, 205-218 (2003).
10. M.A. Bolt and I. Tolstoy, "Formulation of the Wave Propagation in Infinite Media by Normal Coordinates with an Application to Diffraction", *J. Acoust. Soc. Am.*, **29** (3), 381-391 (1957).
11. J. Borish, "Extension of the Image Model to Arbitrary Polyhedra", *J. Acoust. Soc. Am.*, **75** (6), 1827-1836 (1984).
12. D. Botteldooren, "Finite-Difference Time-Domain Simulation of Low-Frequency Room Acoustics Problems", *J. Acoust. Soc. Am.*, **98** (6), 3302-3308 (1995).
13. R.N. Bracewell, *The Fourier Transform and Its Applications* (McGraw-Hill, U.S.A., 1978).

14. J.S. Bradley, "Auditorium Acoustics Measurements from Pistol Shots", *J. Acoust. Soc. Am.*, **80** (1), 199-205 (1986).
15. J.S. Bradley, R. Reich and S.G. Norcross, "A Just Noticeable Difference in C_{50} for Speech", *Appl. Acoust.*, **58**, 99-108 (1999).
16. J.S. Bradley, G.A. Soulodre and S. Norcross, "Factors Influencing the Perception of Bass", *J. Acoust. Soc. Am.*, **101** (5), 3135 (1997).
17. B. Brouard, D. Lafarge and J.-F. Allard, "A General Method of Modeling Sound Propagation in Layered Media", *J. Sound & Vib.*, **183** (1), 129-142 (1995).
18. P.T. Calamia, "Advances in Edge-Diffraction Modeling for Virtual Acoustic Simulations", PhD Dissertation, Princeton University, 2009.
19. G. Chan, "Prediction of Low-Frequency Sound-Pressure Fields in Fitted Rooms for Active Noise Control", M.A.Sc. Thesis, University of British Columbia, 2007.
20. O. Cousins, "Prediction of Sound Pressure and Intensity Fields in Rooms and Near Surfaces by Ray Tracing", M.A.Sc. Thesis, University of British Columbia, 2008.
21. T.J. Cox, B.-I.L. Dalenback, P. D'Antonio, J.J. Embrechts, J.Y. Jeon, E. Mommertz and M. Vorländer, "A Tutorial on Scattering and Diffusion Coefficients for Room Acoustic Surfaces", *Acta Acustica united with Acustica*, **92**, 1-15 (2006).
22. T.J. Cox and P. D'Antonio, *Acoustic Absorbers and Diffusers* (Taylor and Francis, U.K., 2009).
23. B.-I. Dalenbäck, M. Kleiner and P. Svensson, "A Macroscopic View of Diffuse Reflection", *J. Audio Eng. Soc.*, **42** (10), 793-806 (1994).
24. S. Daltrop, M. Hodgson and C. Wakefield, "Experimental Investigation of the Effects of Absorptive Surfaces on the Acoustical Performance of a Barrier in an Anechoic Chamber", *Can. Acoust.*, **38** (3), 182-183 (2010).
25. E. De Geest and R. Garcea, "Simulation of Room Transmission Functions using a Triangular Beam Tracing Computer Model", *IEEE ASSP Workshop on Applications of Signal Processing to Audio and Acoustics*, 253-256 (1995).
26. E. De Geest and H. Patzold, "Comparison between Room Transmission Functions Calculated with a Boundary Element Method and a Ray Tracing Method Including Phase", *Proceeding of internoise 96*, **6**, 3177-3180 (1996).

27. P.E. Doak and P.G. Vaidya, "Attenuation of Plane Wave and Higher Order Mode Sound Propagation in Lined Ducts", *J. Sound & Vib.*, **12** (2), 201-224 (1970).
28. I.A. Drumm and Y.W. Lam, "The Adaptive Beam-Tracing Algorithm", *J. Acoust. Soc. Am.*, **107** (3), 1405-1412 (2000).
29. V. Easwaran and A. Craggs, "On Further Validation and Use of the Finite Element Method to Room Acoustics", *Appl. Acoust.*, **187** (2), 195-212 (1995).
30. J.J. Embrechts, "Broad Spectrum Diffusion Model for Room Acoustics Ray-Tracing Algorithms", *J. Acoust. Soc. Am.*, **107** (4), 2068-2081 (2000).
31. F. Fahy, *Foundations of Engineering Acoustics* (Academic Press, U.K., 2001).
32. F. Fahy and P. Gordonio, *Sound and Structural Vibration – Radiation, Transmission and Response* (Academic Press, The Netherlands, 2007).
33. A. Farina, "RAMSETE – A New Pyramid Tracer for Medium and Large Scale Acoustic Problems", *Proceeding of EURONOISE 95*, 55-60 (1995).
34. C. Foy, V. Valeau, A. Billon, J. Picaut and A. Sakout, "An Empirical Diffusion Model for Acoustic Prediction in Rooms with Mixed Diffuse and Specular Reflections", *Acta Acustica united with Acustica*, **95** (1), 97-105 (2009).
35. T. Funkhouser, N. Tsingos, I. Carlbom, G. Eko, M. Songhi, J.E. West, G. Pingali, P. Min and A. Ngan, "A Beam Tracing Method for Interactive Architectural Acoustics", *J. Acoust. Soc. Am.*, **115** (2), 739-756 (2004).
36. A.C. Gade, "Acoustics in Halls for Speech and Music", *Springer Handbook of Acoustics* (Springer Science + Business Media, U.S.A., 2007).
37. D. Ghazanfarpour and J.-M. Hasenfratz, "A Beam Tracing Method with Precise Antialiasing for Polyhedral Scenes", *Computer and Graphics*, **22** (1), 103-115 (1998).
38. A.S. Glassner (Ed.), *An Introduction to Ray tracing* (Academic Press, U.K., 1991).
39. J. Guo and M. Hodgson, "Investigation of Active Noise Control in Non-Diffuse Sound Fields", *Proceedings of ACTIVE 99*, 621-632 (1999).
40. W.J. Hadden and A.D. Pierce, "Sound Diffraction around Screens and Wedges for Arbitrary Point Source Locations", *J. Acoust. Soc. Am.*, **69** (5), 1266-1276 (1981).
41. J.K. Hammond, "Fundamentals of Signal Processing", *Fundamentals of Noise and Vibration* (E & FN Spon, U.S.A., 1998).

42. I. Harari and T.J.R. Hughes, "A Cost Comparison of Boundary and Finite Element Methods for Problems of Time-Harmonic Acoustics", *Computer Methods in Applied Mathematics and Engineering*, **97** (1), 77-102 (1992).
43. H.S. Heaps, "Reflection of a Plane Acoustic Wave from a Surface of Nonuniform Impedance", *J. Acoust. Soc. Am.*, **28** (4), 666-671 (1956).
44. P.S. Heckbert and P. Hanrahan, "Beam Tracing Polygon Objects", *Computer Graphics*, **18** (3), 119-127 (1984).
45. M. Hodgson, *(D,E)RAYCUB's User's Manual*, University of British Columbia.
46. M. Hodgson, "On the Accuracy of Models for Predicting Sound Propagation in Fitted Rooms", *J. Acoust. Soc. Am.*, **88** (2), 871-878 (1990).
47. M. Hodgson, "Evidence of Diffuse Surface Reflections in Rooms", *J. Acoust. Soc. Am.*, **89** (2), 765-771 (1991).
48. M. Hodgson, "When is the Diffuse-Field Theory Applicable?", *Appl. Acoust.*, **49** (3), 197-207 (1996).
49. M. Hodgson and J. Bradley, "Sound in Rooms", *Noise and Vibration Control Engineering: Principles and Applications* (John Wiley & Sons, U.S.A., 2006).
50. M. Hodgson, O. Cousins, G. Chan and V. Valeau, "Ray-tracing prediction of sound-pressure and sound-intensity fields in empty and fitted rooms", *J. Acoust. Soc. Am.*, **123** (5), 3760 (2008).
51. M. Hodgson and E.-M. Nosal, "Experimental Evaluation of Radiosity for Room Sound-Field Prediction", *J. Acoust. Soc. Am.*, **120** (2), 808-819 (2006).
52. M. Hodgson and A. Wareing, "Comparisons of Predicted Steady-State Levels in Rooms with Extended- and Local-Reaction Bounding Surfaces", *J. Sound & Vib.*, **309**, 167-177 (2008).
53. M. Hodgson and G. Wong, "Ray-Tracing Prediction of Optimal Conditions for Speech in Realistic Classrooms", *Appl. Acoust.*, **70** (7), 915-920 (2009).
54. T. Houtgast and H.J.M. Steeneken, "The Modulation Transfer Function in Room Acoustics as a Predictor of Speech Intelligibility", *Acustica*, **28** (1), 66-73 (1973).
55. T. Houtgast and H.J.M. Steeneken, "A Multi-Language Evaluation of the RASTI-Method for Estimating Speech Intelligibility in Auditoria", *Acustica*, **54**, 185-199 (1984).

56. T. Houtgast and H.J.M. Steeneken, "A Review of the MTF Concept in Room Acoustics and Its Use for Estimating Speech Intelligibility in Auditoria", *J. Acoust. Soc. Am.*, **77** (3), 1069-1077 (1985).
57. T. Houtgast, H.J.M. Steeneken and R. Plomp, "Predicting Speech Intelligibility in Rooms from the Modulation Transfer Function. I. General Room Acoustics", *Acustica*, **46**, 60-72 (1980).
58. C.-H. Jeong, "A Correction of Random Incidence Absorption Coefficients for the Angular Distribution of Acoustic Energy under Measurement Conditions", *J. Acoust. Soc. Am.*, **125** (4), 2064-2071 (2009).
59. C.-H. Jeong, "Non-Uniform Sound Intensity Distributions when Measuring Absorption Coefficients in Reverberation Chambers Using a Phased Beam Tracing", *J. Acoust. Soc. Am.*, **127** (6), 3560-3568 (2010).
60. C.-H. Jeong and J.-G. Ih, "A Note on Proper Frequency Resolution for the Room Transfer Function in the Phased Beam Tracing Method", *Appl. Acoust.*, **70** (1), 120-128 (2009).
61. C.-H. Jeong, J.-G. Ih and J.H. Rindel, "An Approximate Treatment of Reflection Coefficient in the Phased Beam Tracing Method for the Simulation of Enclosed Sound Fields at Medium Frequencies", *Appl. Acoust.*, **69** (7), 601-613 (2008).
62. Z. Jiang and X. Qiu, "Receiving Radius Determination in Ray-Tracing Sound Prediction of Rectangular Enclosure", *J. Sound & Vib.*, **301**, 391-399 (2007).
63. Y. Jing and N. Xiang, "A Modified Diffusion Equation for Room-Acoustic Prediction", *J. Acoust. Soc. Am.*, **121** (6), 3284-3287 (2007).
64. Y. Jing and N. Xiang, "One-dimensional Transport Equation Models for Sound Energy Propagation in Long Spaces: Simulations and Experiments", *J. Acoust. Soc. Am.*, **127** (4), 2323-2331 (2010).
65. J. Kang, "Acoustics of Long Underground Spaces", *Tunnelling and Underground Space Technology*, **12** (1), 15-21 (1997).
66. J.B. Keller, "Geometrical Theory of Diffraction", *J. Opt. Soc. Am.*, **52** (2), 116-130 (1962).
67. L.E. Kinsler, A.R. Frey, A.B. Coppens and J.V. Sanders, *Fundamentals of Acoustics* (John Wiley and Sons, U.S.A., 1982)
68. M. Kleiner, B.-I. Dalenbäck and P. Svensson, "Auralization – An Overview", *J. Audio Eng. Soc.*, **41** (11), 861-875 (1993).

69. R.G. Kouyoumijian and P.H. Pathak, "A Uniform Geometrical Theory of Diffraction from an Edge in a Perfectly Conducting Surface", *Proceedings of the IEEE*, **62** (11), 1448-1461 (1974).
70. A. Krokstad, S. Strom and S. Sorsdal, "Calculating the Acoustical Room Response by the Use of a Ray Tracing Technique", *J. Sound & Vib.*, **8** (1), 118-125 (1968).
71. H. Kuttruff, "Simulierte Nachhallkurven in Rechteckräumen mit diffusem Schallfeld" [Simulated Reverberation Curves in Rectangular Rooms with Diffuse Sound Fields], *Acustica*, **25** (6), 333-342 (1971).
72. H. Kuttruff, "On the Audibility of Phase Distortions in Rooms and its Significance for Sound Reproduction and Digital Simulation in Room Acoustics", *Acustica*, **74**, 3-7 (1991).
73. H. Kuttruff, "Auralization of Impulse Responses Modeled on the Basis of Ray-Tracing Results", *J. Audio Eng. Soc.*, **41** (11), 876-880 (1993).
74. H. Kuttruff, *Room Acoustics* (Spon Press, U.K., 2009).
75. S. Laine, S. Siltanen, T. Lokki and L. Savioja, "Accelerated Beam Tracing Algorithm", *Appl. Acoust.*, **70** (1), 172-181 (2009).
76. Y.W. Lam, "A Comparison of Three Diffuse Reflection Modeling Methods Used in Rooms Acoustics Computer Models", *J. Acoust. Soc. Am.*, **100** (4), 2181-2192 (1996).
77. Y.W. Lam, "Issues for Computer Modelling of Room Acoustics in Non-Concert Hall Settings", *Acoust. Sci. & Tech.*, **26** (2), 145-155 (2005).
78. S.K. Lau and S.K. Tang, "Performance of a Noise Barrier within an Enclosed Space", *Appl. Acoust.*, **70** (1), 50-57 (2009).
79. H. Lee and B.-H. Lee, "An Efficient Algorithm for the Image Model Technique", *Appl. Acoust.*, **24** (2), 87-115 (1988).
80. H. Lehnert, "Systematic Errors of the Ray-Tracing Algorithm", *Appl. Acoust.*, **38**, 207-221 (1993).
81. S. Lesoinne and J.-J. Embrechts, "Size-Adaptive Spherical Receptor Acceleration Method for Acoustical Ray Tracing", *J. Acoust. Soc. Am.*, **123** (5), 3769 (2008).
82. T. Lewers, "A Combined Beam Tracing and Radiant Exchange Computer Model of Room Acoustics", *Appl. Acoust.*, **38**, 161-178 (1993).

83. K.M. Li and H.Y. Young, "A Review of Commonly Used Analytical and Empirical Formulae for Predicting Sound Diffracted by a Thin Screen", *Appl. Acoust.*, **66** (1), 45-76 (2005).
84. T. Lokki, V. Pulkki and P.T. Calamia, "Measurement and Modeling of Diffraction from an Edge of a Thin Panel", *Appl. Acoust.*, **69**, 824-832 (2008).
85. M. Long, *Architectural Acoustics* (Elsevier Academic Press, U.S.A., 2006)
86. D.V. Maercke and J. Martin, "The Prediction of Echogram and Impulse Responses within the Epidaure Software", *Appl. Acoust.*, **38**, 93-114 (1993).
87. Y. Makita and T. Hidaka, "Revision of the Cos-Theta-Law of Oblique Incidence Sound Energy and Modification of the Fundamental Formulations in Geometrical Acoustics in Accordance with the Revised Law", *Acustica*, **63** (3), 163-173 (1987).
88. B.J. McCartin, "On the Eigenstructure of a Sturm-Liouville Problem with an Impedance Boundary Condition", *Global Journal of Pure and Applied Mathematics*, **3** (1), 63-82 (2007).
89. H.M. McDonald, "A Class of Diffraction Problems", *Proc. Lond. Math. Soc.*, **14**, 410-427 (1915).
90. J.G. McDaniel and C.L. Clarke, "Interpretations and Identifications of Minimum Phase Reflection Coefficients", *J. Acoust. Soc. Am.*, **110** (6), 3003-3010 (2001).
91. S.G. McGovern, "Fast Image Method for Impulse Response Calculations of Box-Shaped Rooms", *Appl. Acoust.*, **70** (1), 182-189 (2009).
92. H. Medwin, "Shadowing by Finite Noise Barriers", *J. Acoust. Soc. Am.*, **69**, 1060-1064 (1981).
93. F.P. Mechel, "Modal Solutions in Rectangular Ducts Lined with Locally Reacting Absorbers", *Acustica*, **73**, 223-239 (1991).
94. P.M. Morse, "Some Aspects of the Theory of Room Acoustics", *J. Acoust. Soc. Am.*, **11** (1), 56-66 (1939).
95. P.M. Morse, "The Transmission of Sound inside Pipes", *J. Acoust. Soc. Am.*, **11** (2), 205-210 (1939).
96. P.M. Morse and R.H. Bolt, "Sound Waves in Rooms", *Reviews of Modern Physics*, **16** (2), 69-150 (1944).

97. P.M. Morse and K.U. Ingard, *Theoretical Acoustics* (Princeton University Press, U.S.A., 1986).
98. S.J.S. Morris, "Sound Speed without Entropy", *Am. J. Phys.*, **70** (5), 495-497 (2002).
99. Y. Naka, "Numerical Methods for Solving the Wave Equation in Large Enclosures with Application to Room Acoustics", PhD Dissertation, Boston University, 2007.
100. P.A. Nelson and S.J. Elliot, *Active Control of Sound* (Academic Press, U.S.A., 1999).
101. E.-M. Nosal, M. Hodgson and I. Ashdown, "Improved Algorithms and Methods for Room Sound-Field Prediction by Acoustical Radiosity in Arbitrary Polyhedral Rooms", *J. Acoust. Soc. Am.*, **116** (2), 970-980 (2004).
102. E. Ollendorf, "Statistische Raumakustik als Diffusionproblem" [Statistical Room Acoustics as a Diffusion Problem], *Acustica*, **21**, 236-245 (1969).
103. A.M. Ondet and J.L. Barbry, "Modeling of Sound Propagation in Fitted Workshop Using Ray Tracing", *J. Acoust. Soc. Am.*, **85** (2), 787-796 (1988).
104. M. Petyt and C.J.C. Jones, "Numerical Methods in Acoustics", *Advanced Applications in Acoustics, Noise and Vibration* (Spon Press, U.K., 2005).
105. J. Picaut, L. Simon and J.-D. Polack, "A Mathematical Model of Diffuse Sound Field Based on a Diffusion Equation", *Acta Acustica united with Acustica*, **83** (4), 614-621 (1997).
106. J. Picaut, L. Simon and J.-D. Polack, "Sound Field in Long Rooms with Diffusely Reflecting Boundaries", *Appl. Acoust.*, **56**, 217-240 (1999).
107. A.D. Pierce, "Diffraction of Sound around Corners and over Wide Barriers", *J. Acoust. Soc. Am.*, **55** (5), 941-955 (1974).
108. A.D. Pierce, *Acoustics – An Introduction to Its Physical Principles and Applications* (Acoustical Society of America, U.S.A., 1989).
109. J.-D. Polack, "Playing Billiards in the Concert Hall: The Mathematical Foundations of Geometrical Room Acoustics", *Appl. Acoust.*, **38**, 235-244 (1993).
110. J.H. Rindel, "Modelling the Angle-Dependent Pressure Reflection Factor", *Appl. Acoust.*, **38**, 223-234 (1993).
111. M.R. Schroeder, "New Method of Measuring Reverberation Time", *J. Acoust. Soc. Am.*, **37** (3), 409-412 (1965).

112. M.R. Schroeder, “Modulation Transfer Functions: Definition and Measurement”, *Acustica*, **49** (3), 179-182 (1981).
113. A. Singh, T. De Rybel and J.R. Marti, “FFT Tutor: A MatLab-Based Instruction Tool for FFT Parameter Exploration”, *Can. Acoust.*, (2008).
114. G.-B. Stan, J.-J. Embrechts and D. Archambeau, “Comparison of Different Impulse Response Measurement Techniques”, *J. Audio Eng. Soc.*, **50** (4), 249-262 (2002).
115. H.J.M. Steeneken and T. Houtgast, “A Physical Method for Measuring Speech-Transmission Quality”, *J. Acoust. Soc. Am.*, **67** (1), 318-326 (1980).
116. U.M. Stephenson, “An Energetic Approach for the Simulation of Diffraction within Ray Tracing Based on the Uncertainty Principle”, *Acta Acustica united with Acustica*, **96**, 516-535 (2010).
117. U.M. Stephenson and U.P. Svensson, “An Improved Energetic Approach to Diffraction Based on the Uncertainty Principle”, *Proc. 19th Intl. Congress on Acoustic*, Madrid (2007).
118. J. Stewart, *Calculus: Early Transcendental* (Brooks/Cole Publishing Company, U.S.A., 1999).
119. J.S. Suh and P.A. Nelson, “Measurement of Transient Response of Rooms and Comparison with Geometrical Acoustic Models”, *J. Acoust. Soc. Am.*, **105** (4), 2304-2317 (1999).
120. U.P. Svensson and P.T. Calamia, “Edge-Diffraction Impulse Responses Near Specular-Zone and Shadow-Zone Boundaries”, *Acta Acustica united with Acustica*, **92**, 501-512 (2006).
121. U.P. Svensson, P.T. Calamia and S. Nakanishi, “Frequency-Domain Edge Diffraction for Finite and Infinite Edges”, *Acta Acustica united with Acustica*, **95**, 568-572 (2009).
122. U.P. Svensson, R.I. Fred and J. Vanderkooy, “An Analytic Secondary Source Model of Edge Diffraction Impulse Responses”, *J. Acoust. Soc. Am.*, **106** (5), 2331-2344 (1999).
123. T. Terai and Y. Kawai, “BEM Applications in Architectural Acoustics”, *Boundary Element Methods in Acoustics* (Computational Mechanics Publications, U.K., 1991).
124. R.R. Torres, M. Kleiner and B.-I. Dalenbäck, “Audibility of ‘Diffusion’ in Room Acoustics Auralization: An Initial Investigation”, *Acta Acustica united with Acustica*, **86** (6), 919-927 (2000).

125. R.R. Torres, U.P. Svensson and M. Kleiner, "Computation of Edge Diffraction for more Accurate Room Acoustics Auralization", *J. Acoust. Soc. Am.*, **109** (2), 600-610 (2001).
126. N. Tsingos, T. Funkhouser, A. Ngan and I. Carlbom, "Modeling Acoustics in Virtual Environments Using the Uniform Theory of Diffraction", *Proceedings of the 28th Annual Conference on Computer Graphics and Interactive Techniques*, 545-552 (2001).
127. V. Valeau, J. Picaut and M. Hodgson, "On the Use of a Diffusion Equation for Room-Acoustic Prediction", *J. Acoust. Soc. Am.*, **119** (3), 1504-1513 (2006).
128. V. Valeau, M. Hodgson and J. Picaut, "A Diffusion-Based Analogy for the Prediction of Sound Fields in Fitted Rooms", *Acta Acustica united with Acustica*, **93**, 94-105 (2007).
129. M. Vorländer, "International Round Robin on Room Acoustical Computer Simulations", *Proceedings of the 15th International Congress on Acoustics*, 689-692 (1995).
130. M. Vorländer, "Simulation of the Transient and Steady-State Sound Propagation in Rooms Using a new Combined Ray-Tracing/Image-Source Algorithm", *J. Acoust. Soc. Am.*, **86**, 172-178 (1989).
131. M. Vorländer, *Auralization – Fundamentals of Acoustics, Modelling, Simulation, Algorithms and Acoustic Virtual Reality* (Springer-Verlag, Germany, 2008).
132. M. Vorländer and F.P. Mechel, "Room Acoustics", *Formulas of Acoustics* (Springer-Verlag, Germany, 2008).
133. A. Wareing, "Acoustic Modeling of Rooms with Extended-Reaction Surfaces", M.A.Sc. Thesis, University of British Columbia, 2000.
134. A. Wareing and M. Hodgson, "Beam-Tracing Model for Predicting Sound Fields in Rooms with Multilayer Bounding Surfaces", *J. Acoust. Soc. Am.*, **118** (4), 2321-2331 (2005).
135. J.S. Wright, "Fundamentals of Diffraction", *J. Audio Eng. Soc.*, **45** (5), 347-356 (1997).
136. N. Xiang, Y. Jing and A.C. Bockman, "Investigation of Acoustically Coupled Enclosures Using a Diffusion-Equation Model", *J. Acoust. Soc. Am.*, **126** (3), 1187-1198 (2009).
137. Z. Xiangyang, C. Ke'an and S. Jincai, "Modeling the Sound Fields in Rooms with Multiple Sources Using a Hybrid Image Method Including Phase", *Acta Acustica united with Acustica*, **88**, 88-92 (2002).
138. Z. Xiangyang, C. Ke'an and S. Jincai, "On the Accuracy of the Ray-Tracing Algorithms Based on Various Sound Receiver Models", *Appl. Acoust.*, **64**, 433-441 (2003).

139. B. Yousefzadeh and M. Hodgson, “Prediction of Sound Propagation in Rectangular Ducts by a Ray-Tracing Model with Phase”, *J. Acoust. Soc. Am.*, **125** (4), 2494 (2009).
140. ISO/FDIS 3882-1, “Acoustics – Measurement of Room Acoustic Parameters – Part 1: Performance Spaces” (2009).
141. [<http://www.mathworks.com/access/helpdesk/help/techdoc/ref/quadgk.html>]:
MATLAB’s help documentation on *quadgk*.